Supporting information

for

'Connecting the dots': knitting C-phenylresorcin[4]arenes with aromatic linkers for task-specific porous organic polymers

Arkaprabha Giri, MD. Waseem Hussain, Bahadur Sk, and Abhijit Patra*

Department of Chemistry, Indian Institute of Science Education and Research Bhopal (IISERB), Bhopal-462066, Fax: +91 (0)755 409 2392; Tel: +91 (0)755 669 1337

E-mail: abhijit@iiserb.ac.in

Contents

		Page No.
1.	Instrumentation and chemicals	S-3
2.	*C*-phenylresorcin[4]arene: A unique macrocyclic building block	S-5
	2.1. Design strategy	S-6
	2.2. Synthesis and characterization of macrocyclic cavitands	S-8
3.	Fabrication and characterization of porous organic polymers (POPs)	S-9
	3.1. Fabrication of POPs	S-9
	3.2. Thermogravimetric analysis (TGA)	S-10
	3.3. Solid-state ^{13}C (CP/MAS) NMR analysis	S-10
	3.4. XPS analysis	S-12
	3.5. PXRD analysis	S-13
	3.6. Microscopic analysis (FESEM, TEM)	S-13
	3.7. EDS analysis	S-14
	3.8. BET specific surface area analysis	S-15
	3.9. Cavity of resorcin[4]arene and pore size distribution of POPs	S-17
4.	CO_2 and H_2 uptake	S-18
	4.1. Isosteric heat of adsorption	S-18
	4.2. Selectivity of CO_2 uptake	S-19
5.	Residual palladium in RN4-OH	S-20
	5.1. Estimation of residual palladium	S-20
	5.2. Reduction of *p*-nitrophenol	S-21
6.	Dispersity of POPs in common organic solvents and reaction mixture	S-22

6.1. Dispersity of RN4-Az-OH in common organic solvents and water S-22
6.2. Zeta potential values of POPs in water S-22
6.3. Interaction of tetra-n-butylammonium bromide with RN4-Az-OH S-23
7. Synthesis and characterization of RN4-Az-OR and Zn/RN4-Az-OH S-24
8. CO_2 conversion S-27
8.1. CO_2 fixation to cyclic carbonates S-27
8.2. Recyclability of Zn/RN4-Az-OH S-28
8.3. Stability of the RN4-Az-OH and Zn/RN4-Az-OH after recycling S-28
9. Removal of organic micropollutants from water S-29
9.1. Interaction of methylene blue with RN4-F S-30
9.2. Percentage removal efficiency of RN4-F S-30
9.3. Calculation of dimensions of model micropollutants and linkers S-32
9.4. Kinetic analysis of micropollutant uptake S-33
9.5. Thermodynamic analysis of micropollutant uptake S-36
9.6. Recyclability of RN4-F S-37
11. Comparative tables S-38
11.1 Comparative accounts of properties and applications of RN4-based POPs with various cavitand-based porous organic materials S-38
11.2 Comparative accounts of RN4-based POPs with other notable porous materials for gas uptake S-39
11.3 Comparative accounts of RN4-based POPs with other porous materials for CO_2 conversion S-40
11.4 Comparative accounts of RN4-based POPs with other porous organic materials for selective separation of organic micropollutants S-42
10. MALDI-TOF, ^{1}H and ^{13}C NMR analysis of compounds S-43
12. References S-59

1. Instrumentation and Chemicals

Nuclear magnetic resonance (NMR) Spectroscopy: ^{1}H NMR and ^{13}C NMR spectra were recorded on Bruker Avance III 500 and 400 MHz NMR spectrometers. The residual solvent signal was used as an internal standard, and chemical shifts (δ) were reported in parts per million (ppm). The NMR measurements were carried out in $CDCl_3$ and dimethyl sulfoxide (DMSO-d_6) at room temperature. The solid-state ^{13}C cross-polarization magic angle spinning (CP/MAS) NMR experiments were carried out on JEOL ECX2 400 MHz (field 9.4 T) standard bore spectrometer equipped with 4 mm solid-state MAS probe. The samples were packed into a 4 mm Zirconia rotor and spun at 8 kHz at the magic angle.

Fourier transform infrared spectroscopy (FTIR): FTIR measurements were done on Perkin-Elmer Model 2000 FTIR spectrometer using KBr pellet. Twenty scans were signal-averaged, with a resolution of 4 cm^{-1} at ambient temperature.

Matrix-assisted laser desorption ionization (MALDI): Matrix-assisted laser desorption ionization time of flight (MALDI-TOF) mass spectrometry was performed with Bruker Daltonics UltrafleXtreme, using software flexControl version 3.4.

Thermogravimetric analysis (TGA): TGA analysis was carried out using a Perkin Elmer TGA-6000 instrument. The sample was heated at a rate of 10 °C min^{-1} under a nitrogen atmosphere to a maximum of 800 °C.

Powder X-ray diffraction (PXRD): PXRD experiment was done on a PANalytical Empyrean XRD instrument. Data was collected for 2θ values ranging from 5° to 80°.

Field emission scanning electron microscopy (FESEM): The morphology of polymer was examined using Carl Zeiss (Ultraplus) field emission scanning electron microscope. The accelerating voltage of 5 kV and 20 kV were used.

Energy dispersive X-ray spectroscopy (EDS): EDS was examined using a spectrometer (Oxford Instruments X-MaxN) attached to FESEM. Measurements were done at a working voltage of 20 kV, and elemental Co was used as a reference.

High-resolution transmission electron microscopy (HRTEM): The porous nature of POPs was observed through HRTEM using FEI TALOS 200S instrument at a working voltage of 200 kV.

X-ray photoelectron spectroscopy (XPS): The XPS experiment was performed on a sample holder with the vacuum dried powder sample drop of the size of 1.5 mm radius using PHI 5000 Versa Prob II, FIE Inc. The scan time was set for 1 h per element for core level scan (energy band: 20 eV) with a pass setting of 23.5 eV, 0.025 eV step and 100 ms time per step for 5 cycles.

Brunauer–Emmett–Teller (BET) specific surface area analysis: All the gas adsorption measurements were performed on Quantachrome Autosorb, QUA211011 equipment. The sample was degassed at 80-100 ℃ for 12 h under vacuum before analysis. Isotherms were analyzed using ASiQwin software.

Steady-state absorption spectroscopy: UV-Visible absorption spectra were recorded on a Cary 100 spectrophotometer.

Zeta potential measurements: The zeta potential values of all the samples were measured in water using Beckman Coulter (Delsa Nano C) particle analyzer.

Chemicals: All chemicals were used as received unless stated otherwise. *p*-Hydroxybenzaldehyde, *p*-bromobenzaldehyde, benzidine, 1,4-diethynyl benzene, tetrafluoroterephthalonitrile, tetrabutylammonium bromide (98%), potassium carbonate, copper(I) iodide, bis(triphenylphosphine)palladium(II) chloride, *N*, *N*-dimethylformamide (DMF, 99%), dimethyl sulfoxide (DMSO, 99%), diisopropylamine (99%), zinc acetate dihydrate, sodium borohydride were received from Sigma-Aldrich. All the chemicals used as the substrate scope in CO_2 conversion and as model micropollutants, e.g., propylene oxide, epichlorohydrin, styrene oxide, 1,2-epoxy-3-phenoxypropane, 1,2-epoxyhexane, methylene blue, cresyl violet, rhodamine B, rhodamine 101 inner salt, methyl orange, methyl blue, Congo red, rose bengal, *p*-nitrophenol, 2-naphthol were received from Sigma-Aldrich. Sodium nitrite (99%), chloroform, diethyl ether, dichloromethane, and hexane were received from Merck. Tetrahydrofuran (THF, 99%), ethanol (99.8%), extra pure concentrated HCl were received from Spectrochem.

2. *C*-phenylresorcin[4]arene: A unique macrocyclic building block

Macrocyclic host molecules having well-defined cavities, versatile functionality, and excellent guest recognition properties trigger intense research in the field of supramolecular chemistry. Resorcin[4]arenes are a unique class of macrocycles and are first characterized by Niederl and Vogel in the year of 1940.[1] D. J. Gutsche and Böhmer classified them as calixarenes by calling them calix[4]resorcinarenes.[2] The characteristics features of resorcin[4]arenes are the following. (i) *Shape*: Resorcin[4]arenes have a bowl-shaped geometry (Figure S1). *C*-phenylresorcin[4]arene can be synthesized by lower rim functionalization of resorcin[4]arene, which has a deeper cavity than that of the pristine cavitand. (ii) *Synthesis*: They can be prepared easily from inexpensive starting materials such as resorcinol and corresponding aromatic/aliphatic aldehyde through various pathways, e.g., Brønsted or Lewis acid-catalyzed condensation, microwave irradiation or solvent-free green synthesis.[3] (iii) *Solubility*: *C*-phenylresorcin[4]arene derivatives are soluble in organic solvents like acetonitrile, DMF, and DMSO. (iv) *Versatile functionality*: The presence of 8 phenolic -OH groups at the upper rim, easily modulable functional groups at the lower rim with π-electron-rich hydrophobic core make the *C*-phenylresorcin[4]arene an interesting macrocyclic building block. We can control the cavity size through the tuning the lower rim, as well. (v) *Host-guest complexation ability*: In acid saturated chloroform, six resorcin[4]arene molecules are hydrogen bonded and form hexameric capsule. The capsule is well explored in host-guest complexation as well as in organocatalysis.[4]

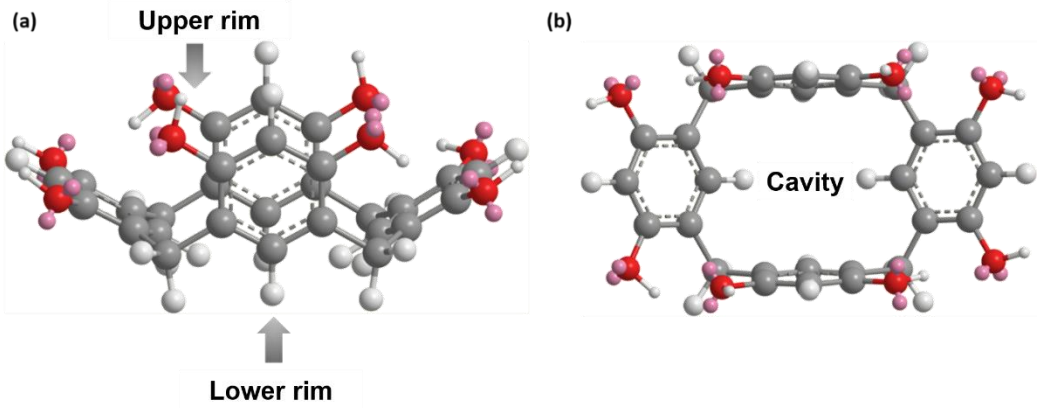

Figure S1. (a) Side and (b) top view of pristine resorcin[4]arene.

2.1. Design strategy

Macrocyclic host molecules have been widely explored as a versatile platform over the last few decades for the molecular separation, catalysis, sensing, etc. However, these applications are mostly limited in the solution phase, and the rich host-guest chemistry of the cavitands was hardly demonstrated in the solid state. Hence, a judicious design strategy for the development of a macrocycle-based host matrix for the above-mentioned applications in the solid phase is a worthy problem to address. In this regard, various strategies have been demonstrated to utilize the intrinsic porosity of molecular containers in the solid state, e.g., (i) integrating the cavitands through the host-guest interactions in the supramolecular polymers,[5] (ii) supramolecular polymers of macrocycles through crystallization,[6] (iii) using the cavitands as the pendant groups of linear polymers and (iv) crosslinking the macrocyclic cavitands through flexible alkyl linkers.[7] But all these strategies suffer from various aspects like occupied cavities of the macrocycles due to the host-guest complexation during the supramolecular polymerization. The noncovalent interactions in the supramolecular assembly of the macrocyclic host in the solid state lead to the instability of the materials after guest removal. On the other hand, the use of flexible alkyl linkers suffers from the pore blocking issue due to the interchain entanglement.

Considering the facts, we employed the rigid aromatic linkers to create shape-persistent pores with hydrothermally robust polymers. In this context, we tuned the length and functionalities of aromatic linkers to develop task-specific porous organic polymers (POPs). The linker length and functionality should affect the physicochemical characteristics of the external pores (Figure S2a). Whereas, the internal pores of the cavitands are likely to remain unaltered. To demonstrate the aforementioned idea, we have chosen three distinct types of linkers, such as (a) diazo, (b) alkyne, and (c) fluorine-rich linker (Figure S2).

(a) *Diazo linker*: Incorporation of diazo-linkage (-N=N-) between two monomeric building units facilitates selective CO_2 capture over N_2 due to the 'N-phobic' and 'CO_2-philic' nature of basic -N=N- linkage.[8] Additionally, the *cis-trans* isomerization due to the diazo linkage leads to the flexibility in the polymer. The flexibility of the polymer allows better dispersibility in the reaction medium. Keeping these advantages in mind, we have designed the azo-linked POP, RN4-Az-OH by connecting the polyphenolic (-OH) and catalytically active macrocyclic cavitand, *C*-phenylresorcin[4]arene core through long diazo linker for the CO_2 conversion. The long linker

leads to mesoporous polymers aiding to easy mass transfer and hence, is contributing to efficient catalysis.

(b) *Alkyne linker*: Rigid alkyne linkers are known for the development of materials with a high surface area.[9] Additionally, a smaller alkyne-based linker leads to the highly microporous network. The high surface area and microporosity lead to effective interactions with small gas molecules. We assumed that connecting the macrocyclic host with such smaller alkyne linkers might lead to the POP (RN4-OH) having high gas uptake ability.

(c) *Fluorine rich linker*: Fluorine-rich porous materials are known for their hydrophobic nature.[10] On the other hand, the fluorine being the strongest electronegative atom have strong H-bonding ability. Again, resorcin[4]arenes are well-known for selective guest encapsulation. Hence, connecting *C*-phenylresorcin[4]arene with fluorine-rich linkers will provide a highly porous platform (RN4-F) for the efficient removal of the organic contaminants from water.

The design strategy, as discussed above, demonstrates the advantages of incorporating *C*-phenylresorcin[4]arene building units in POPs, leading to three distinct and environmentally benign applications in the solid state. We believe that such a design strategy will further open up new avenues for the development of cavitand-based multifunctional porous polymers.

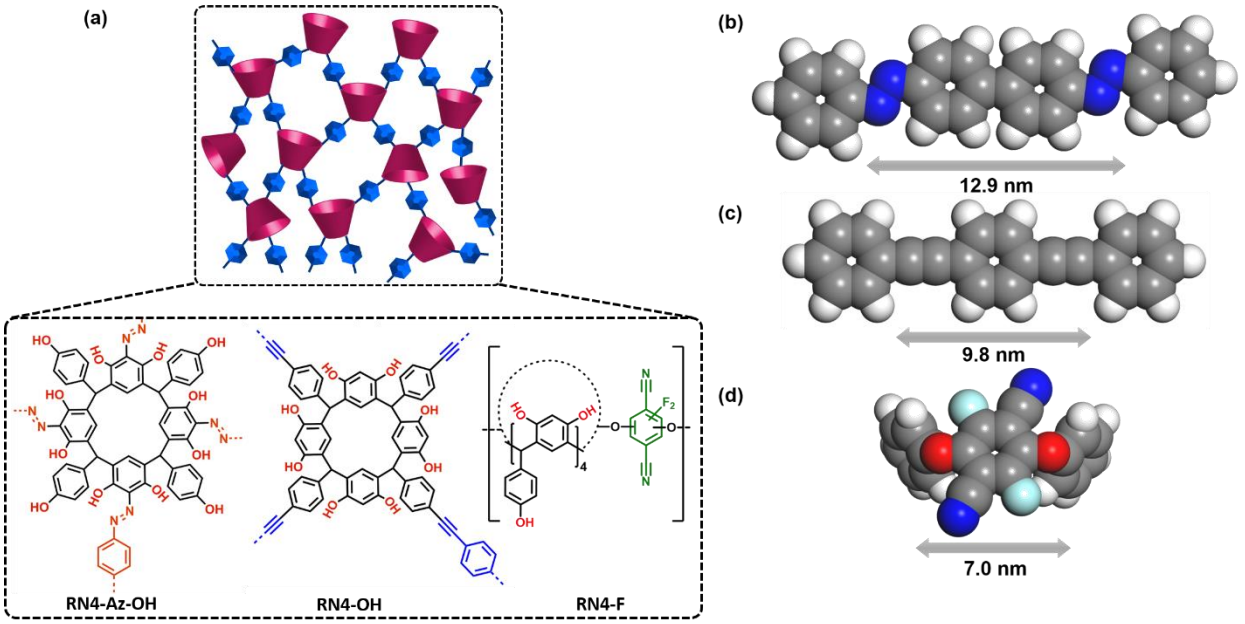

Figure S2. (a) Porous organic polymers (POPs) by connecting the cavitands through aromatic linkers. The length of the DFT optimized structure of (b) diazo linker, (c) dialkyne linker and (d) fluorinated linker, used for connecting the *C*-phenylresorcin[4]arene based 0D macrocyclic core.

2.2. Synthesis and characterization of macrocyclic cavitands

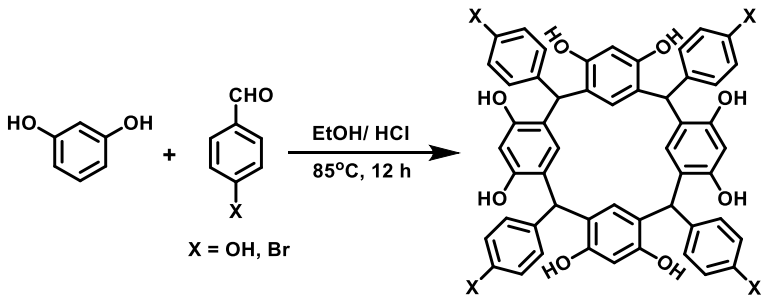

Scheme S1. The synthetic protocol of *C*-phenylresorcin[4]arene derivatives.

(i) Synthesis of p-hydroxyphenylresorcin[4]arene (HRN4)

p-Hydroxyphenylresorcin[4]arene was synthesized following a reported procedure with minor modification.[11] Resorcinol (4.1 mmol) and concentrated HCl (3.5 mL) were dissolved in anhydrous ethanol (25 mL) and stirred at 0°C. Ethanolic solution of *p*-hydroxybenzaldehyde (4.1 mmol) was added dropwise to the cold solution and refluxed for 12 h. After cooling down to room temperature, the pink color precipitate was filtered out and purified via reprecipitation in water. The reprecipitated solid was washed with methanol, acetone, diethyl ether and dried under vacuo for 24 h at 50°C (Scheme S1). Yield: 45%.

^{1}H NMR (500 MHz, DMSO-d_6): δ 8.81 (s, 4H), 8.41 (s, 8H), 6.63 (d, J = 8.5 Hz, 8H), 6.50 (s, 4H), 6.47 (d, J = 8.5 Hz, 8H), 6.08 (s, 4H), 5.52 (s, 4H) ppm.
^{13}C NMR (126 MHz, DMSO-d_6): δ 154.45, 152.27, 135.98, 129.56, 120.91, 114.03, 102.07, 40.57 ppm.
MALDI-TOF: Calculated for $C_{52}H_{40}O_{12}$, 856.88, found (m/z): 855.39 (M^+) and 878.38 ($M+Na^+$).
FT-IR (KBr): 3350 cm^{-1} (O-H stretching), 3026 cm^{-1} (alkyl C-H stretching), 1246 cm^{-1} (C-O stretching), 1614 cm^{-1} (C=C stretching).

(ii) Synthesis of p-bromophenylresorcin[4]arene

Following the above-mentioned protocol, *p*-bromophenylresorcin[4]arene was synthesized using resorcinol and *p*-bromobenzaldehyde (Scheme S1). Yield: 42 %.

^{1}H NMR (400 MHz, DMSO-d_6): δ 8.70 (s, 8H), 7.18 (d, J = 8.1 Hz, 8H), 6.56 (d, J = 8.1 Hz, 8H), 6.37 (s, 2H), 6.17 (s, 4H), 5.69 (s, 2H), 5.60 (s, 4H) ppm.
^{13}C NMR (126 MHz, DMSO-d_6): δ 145.4, 130.4, 130.0, 119.7, 117.9, 102.1, 40.9 ppm.
MALDI-TOF: Calculated for $C_{52}H_{36}Br_4O_8$, 1108.47, found (m/z): 1102.919, 1104.93, 1106.90, 1108.96, 1110.86 (Br_4 isotope pattern 1:4:6:4:1); ($M+Na^+$) (m/z): 1128.87, 1130.62.
FT-IR (KBr): 3460 cm^{-1} (O-H stretching), 2964 cm^{-1} (alkyl C-H stretching), 1618 cm^{-1} (C=C stretching).

3. Fabrication and characterization of porous organic polymers

3.1. Fabrication of POPs

(i) Fabrication of RN4-Az-OH

Benzidine (0.7 mmol, 2 equiv.) was taken in 100 mL round bottom flask and was charged with 30 mL of deionized water, and 2 mL concentrated HCl. The solution was stirred for 30 min in an ice bath. Then 20 mL of aqueous sodium nitrite (1.4 mmol, 4 equiv.) was added dropwise and stirred for 30 min. The color of the solution turned yellowish due to the formation of a diazonium salt. The solution was neutralized with dilute sodium carbonate solution (checked by pH paper). Then it was added slowly to the 30 mL aqueous solution of *p*-hydroxyphenylresorcin[4]arene (0.35 mmol, 1 equiv.) and sodium carbonate (4.2 mmol, 12 equiv.) and stirred for 12 h at 2-3 °C. The precipitate was separated from the reaction mixture by filtration and then washed with dilute aq. HCl. The dark brown colored solid was thoroughly washed with multiple Soxhlet extractions with methanol, THF, and ethanol respectively followed by freeze-drying (Yield: 90-95%).

(ii) Fabrication of RN4-OH

The synthesis of RN4-OH was carried out using Pd-catalyzed Sonogashira cross-coupling polycondensation reaction of *p*-bromophenylresorcin[4]arene and diethynyl benzene. In a typical procedure, *p*-bromophenylresorcin[4]arene (0.18 mmol, 1 equiv.), copper(I) iodide (0.09 mmol, 0.5 equiv.), bis(triphenylphosphine)palladium(II) chloride (0.07 mmol, 0.4 equiv.) were dissolved in 5 mL of dry, degassed 1:1 (v/v) DMF : THF. Diisopropylamine (0.72 mmol, 4 equiv.) and 1,4-diethynylbenzene (0.36 mmol, 2 equiv.) were dissolved in a 5 mL dry, degassed THF and kept in a separate Schlenk tube. The solution containing the diethynyl linker was added dropwise to the solution containing the macrocycle with stirring to afford a dark gray reaction mixture. The mixture was heated at 65 °C under nitrogen for 48 h. After cooling to room temperature, the reaction mixture was quenched with cold acidified methanol. The precipitate was collected through gravimetric filtration. Then it was washed with THF, methanol, and followed by thorough washing by Soxhlet extraction for 24 h each in methanol, THF, chloroform, and ethanol, respectively. The resulting yellowish-brown solid was dried under vacuo at 80 °C for 24 h (Yield: ~50%).

(iii) Fabrication of RN4-F

In a typical procedure, two Schlenk tubes were taken, one containing *p*-hydroxyphenylresorcin[4]arene (HRN4, 0.35 mmol, 1 equiv.) and potassium carbonate (2.8 mmol, 8 equiv.) in dry, degassed DMF (1.5 mL) solvent, and the second tube containing tetrafluoroterephthalonitrile (TFTN, 1 mmol, 3 equiv.) in anhydrous THF (13 mL) solvent. Both the tubes were flushed with N_2 gas for 5 min. The TFTN solution was added drop-wise over 10 min to the Schlenk tube containing *p*-hydroxyphenylresorcin[4]arene using a syringe while stirring at room temperature. After complete addition, the reaction mixture was heated up to 85 °C, and stirring was continued for 48 h. Then, the light brown suspension was cooled. The residual K_2CO_3 was neutralized by washing with 1N HCl until the CO_2 effervescence stopped. The solid was filtered followed by soaking for 15 min each in H_2O, THF, and DCM, respectively. Then the POP was dried through freeze-drying (Yield: 60-70%).

The 12 phenolic OH groups (8 from the upper rim and 4 from the lower rim) in HRN4 are likely to be equally reactive. There is no selective phenolic OH group functionalization during hypercrosslinking (S_NAr), and it is hard to depict the exact propagating sites (Figure S2a). The porous nature of RN4-F depends on the injection rate of the comonomer, temperature, and post-synthetic drying techniques (freeze-drying/ thermal drying).[10]

3.2. Thermogravimetric analysis (TGA)

Thermogravimetric analysis showed that RN4-Az-OH is stable up to 250 °C while RN4-OH and RN4-F are stable up to 350 °C. 2-3% weight loss near 100 °C was observed for all the POPs due to the removal of trapped solvents (e.g., ethanol, water) which were strongly H-bonded with the phenolic-OH groups of *C*-phenylresorcin[4]arene core (Figure 2d).

3.3. Solid-state ^{13}C (CP/MAS) NMR analysis

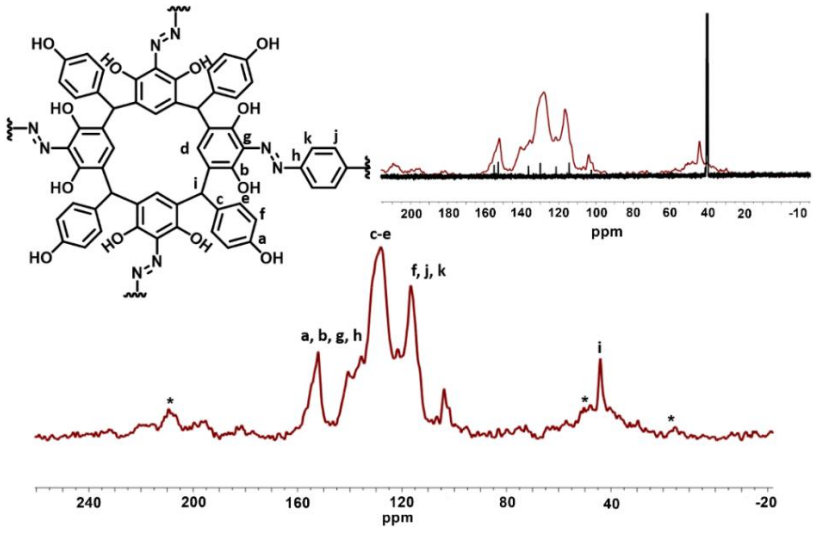

Figure S3. Solid-state ^{13}C (CP/MAS) NMR spectrum of RN4-Az-OH; (*) denotes unassigned peaks (inset: overlay of the solution-state ^{13}C NMR spectrum of HRN4 and the solid-state ^{13}C NMR spectrum of RN4-Az-OH).

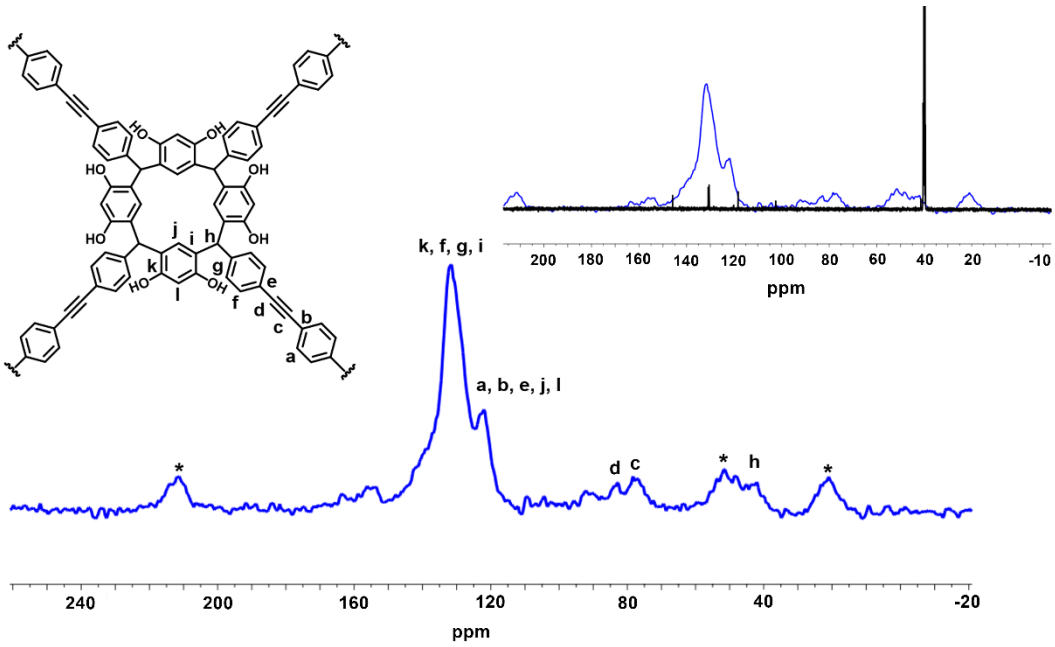

Figure S4. Solid-state ^{13}C (CP/MAS) NMR spectrum of RN4-OH; (*) denotes unassigned peaks (inset: overlay of the solution-state ^{13}C NMR spectrum of *p*-bromophenylresorcin[4]arene and the solid-state ^{13}C NMR spectrum of RN4- OH).

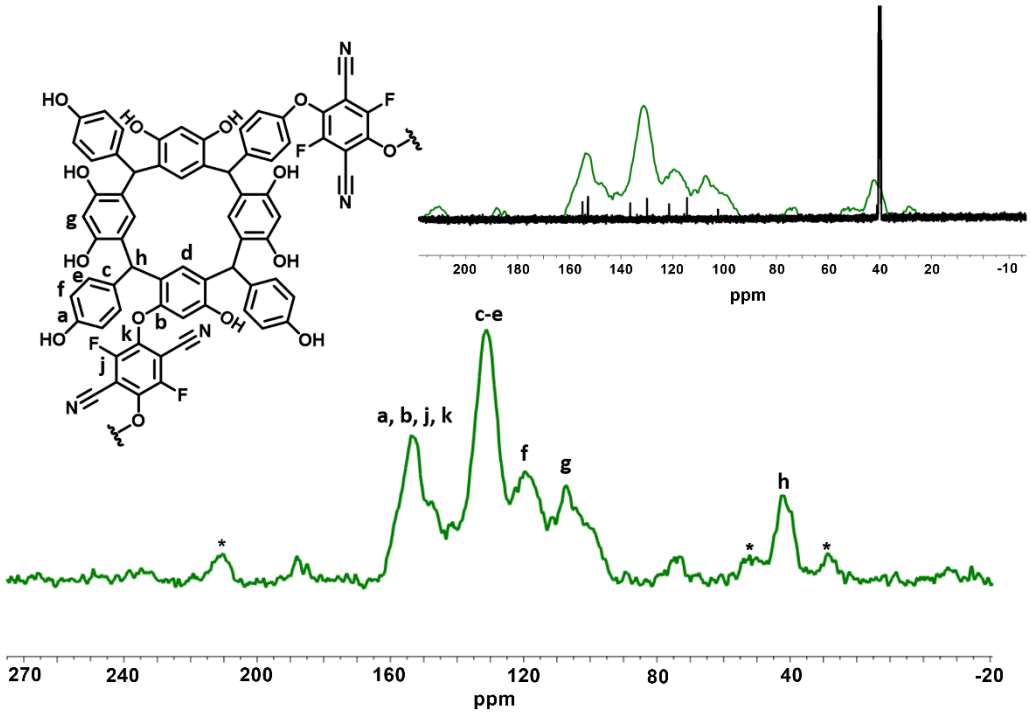

Figure S5. Solid-state ^{13}C (CP/MAS) NMR spectrum of RN4-F; (*) denotes unassigned peaks (inset: overlay of the solution-state ^{13}C NMR spectrum of HRN4 and the solid-state ^{13}C NMR spectrum of RN4-F).

3.4. XPS analysis

The XPS analysis of POPs is shown in Figure S6. The fitting parameter (χ^2) values in all cases are close to 1. The C1s spectra of the cavitand-based POPs, as revealed by the X-ray photoelectron spectroscopy (XPS), showed the presence of the sp^3-C (methine carbon) at 287.6 eV. The peak at 284.3 eV in RN4-OH indicates the presence of sp-C (alkyne) corroborating the cross-coupling (Figure S6). The N1s XPS spectrum of RN4-Az-OH has a peak at 398.6 eV substantiating the presence of the azo-N. The F1s XPS analysis of RN4-F indicated the presence of two different fluorine atoms due to the positional couplings (para: 687 eV and meta: 685 eV) of tetrafluoroterephthalonitrile.

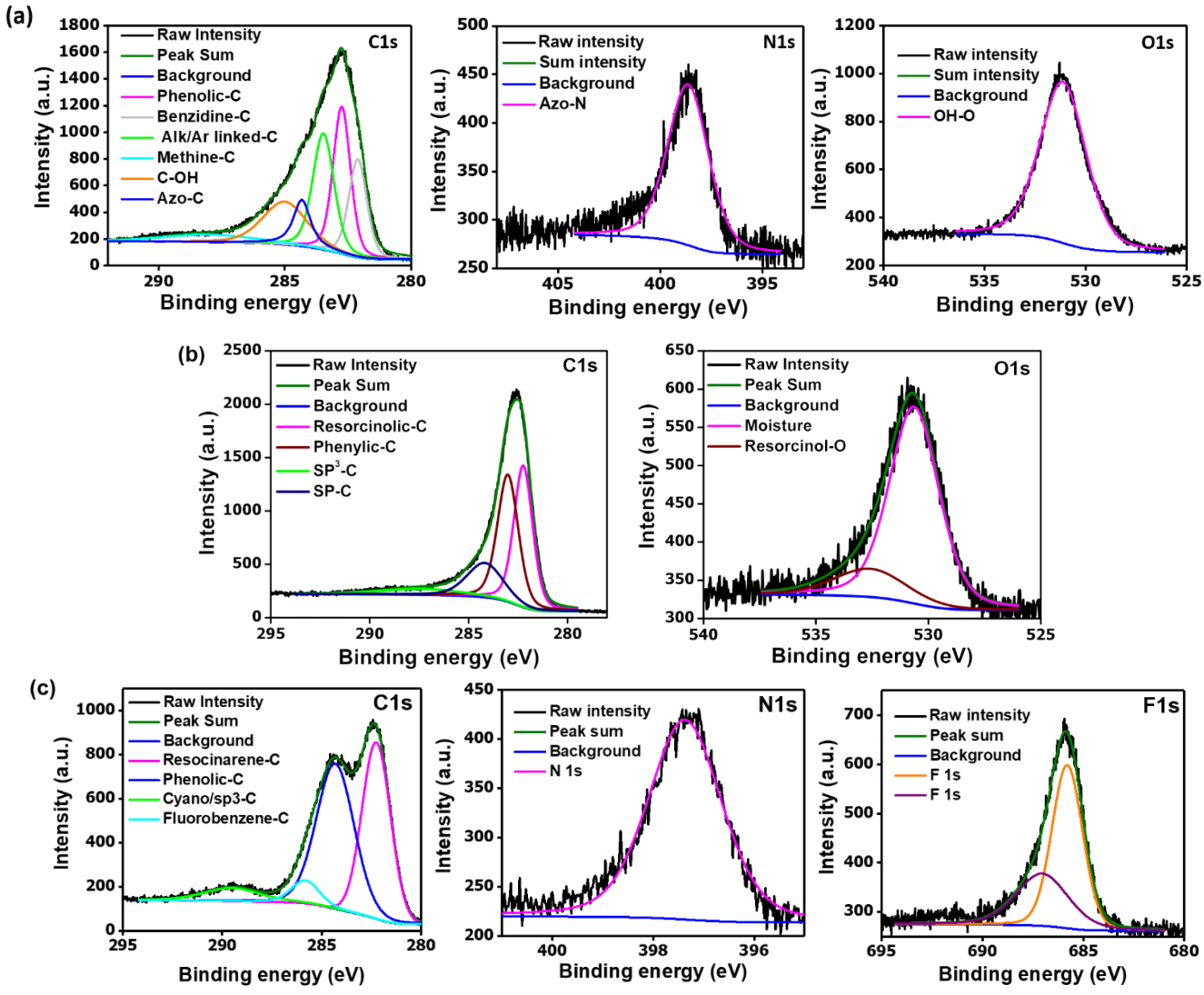

Figure S6. XPS spectra of (a) RN4-Az-OH, (b) RN4-OH, and (c) RN4-F.

3.5. PXRD pattern

The broad PXRD profiles signify the amorphous nature of the POPs. In the case of RN4-OH, a small peak at 2θ = 40° was attributed to the presence of residual palladium [(111) Miller plane] in the porous polymer (Figure S7b).

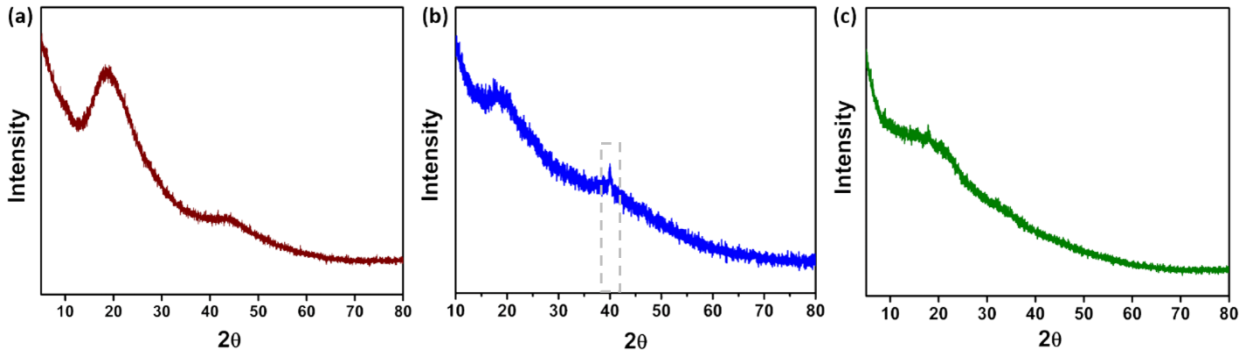

Figure S7. The PXRD patterns of (a) RN4-Az-OH, (b) RN4-OH, and (c) RN4-F.

3.6. Microscopy analysis of POPs

Samples for FESEM were prepared by sprinkling (~ 2 mg) powder POP samples on the aluminium stub using the adhesive carbon tape. All samples were coated with a thin layer of sputtered gold before imaging (Figure S8). The FESEM image of freeze-dried RN4-Az-OH revealed the homogeneous distribution of fused sphere like submicron-sized particles (Figure 3a, S8). This can be attributed to the less dense packing of the polymers leading to the mesoporosity. Amorphous fused sphere-like particles was observed in the case of RN4-OH which generally found in alkyne-linked POPs (Figure 3b, S8).[9] Smaller linkers provide efficient packing in RN4-F and fluoride groups endow the mechanical stiffness to the porous polymer leading to the dense, rigid, large aggregated particles (Figure 3c).[10] HRTEM samples were prepared by drop casting a homogeneous dilute dispersion of POPs (in ethanol) over a carbon-coated 400 mesh Cu grid (Figure S9).

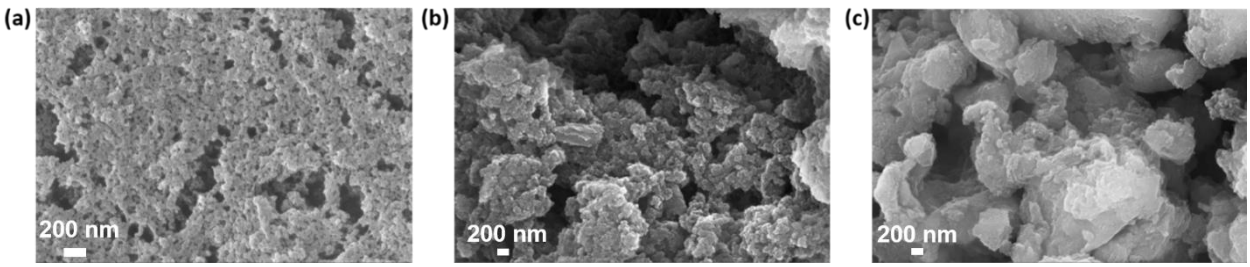

Figure S8. FESEM images of (a) RN4-Az-OH, (b) RN4-OH, and (c) RN4-F (scale bar = 200 nm).

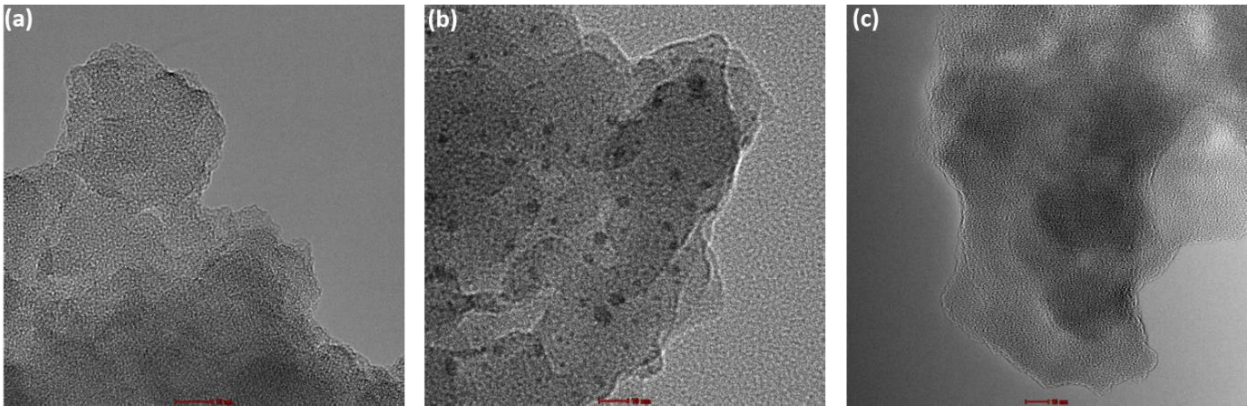

Figure S9. HRTEM images of (a) RN4-Az-OH, (b) RN4-OH, and (c) RN4-F (scale bar = 10 nm).

3.7. Energy dispersive X-ray spectroscopic (EDS) analysis

The EDS analysis was carried out at a working voltage of 20 kV using Co as reference (Figure S10). Atomic and weight percentage of various elements obtained from the EDS analysis is listed in Table S1.

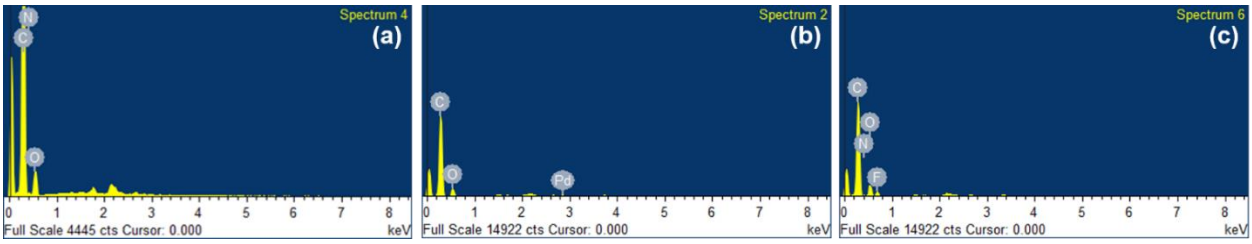

Figure S10. EDS profile of (a) RN4-Az-OH, (b) RN4-OH, and (c) RN4-F.

Table S1 Atomic (at) and weight (wt) percentage of carbon, nitrogen, oxygen, and fluorine acquired from EDS analysis of RN4-Az-OH, RN4-OH, and RN4-F.

POPs	C		O		N		F		Pd	
	at%	wt%	at%	wt%	at%	wt%	at%	wt%	at%	wt%
RN4-Az-OH	77.8	73.2	15.3	19.1	6.9	7.7	-	-	-	-
RN4-OH	89.4	73.0	10.6	13.6	-	-	-	-	0.2	1.4
RN4-F	71.9	65.4	17.9	21.7	4.3	4.5	5.8	8.4	-	-

3.8. BET surface area analysis

All the samples were degassed for 12 h at 60-100 °C under vacuum before analysis. Nitrogen adsorption-desorption isotherms were measured at 77 K. The surface area and pore size distributions were estimated by nitrogen adsorption-desorption isotherms (Figure S11). The pore size distribution was obtained through non-local density functional theory (NLDFT, carbon, slit pore, equilibrium model) analysis.[12] The specific surface area of POPs was obtained by fitting the adsorption isotherm with Brunauer–Emmett–Teller (BET) equation as given below.

$$\frac{P/P_0}{n\,(1-\frac{P}{P_0})} = \frac{1}{n_m C} + \frac{C-1}{n_m C}\,(P/P_0) \qquad (1)$$

where P/P_0 is the relative pressure, n is the specific amount adsorbed at P/P_0, n_m is the specific monolayer capacity, and C is the BET constant. The relative pressure (P/P_0) range used for determination of specific surface areas of all the POPs and HRN4 is $0.05 < P/P_0 < 0.25$.

The surface areas were estimated for three times for the POPs obtained from different batches of synthesis. The standard deviation of BET specific surface areas of HRN4, RN4-Az-OH, and RN4-OH obtained through independent measurements are within ±5, ± 20 and, ± 40 $m^2\ g^{-1}$, respectively. RN4-F is a hypercrosslinked polymer, obtained through aromatic nucleophilic substitution reaction. We noted that depending on the post-synthetic drying (freeze-drying or drying through heating under high vacuum prior to pretreatment for BET surface area measurement) and injection time of the comonomer, the surface area of RN4-F could vary (925-1250 $m^2\ g^{-1}$). However, CO_2 conversion and dye adsorption by RN4-F obtained from different batches fall within the error levels, and the general trend in properties observed for RN4-based POPs is maintained. The similar effect of post-synthetic treatment on surface areas of porous polymers was demonstrated earlier.[10,13]

The H3 type hysteresis loop in the isotherms of RN4-Az-OH suggests the presence of open mesopores, whereas H2(b) type of loop in the isotherms of RN4-OH indicates restricted mesopores (Figure 3e). On the other hand, almost parallel nature of the adsorption and desorption suggests that the narrow slit-like pores are exclusively present in RN4-F (Figure 3e).[12]

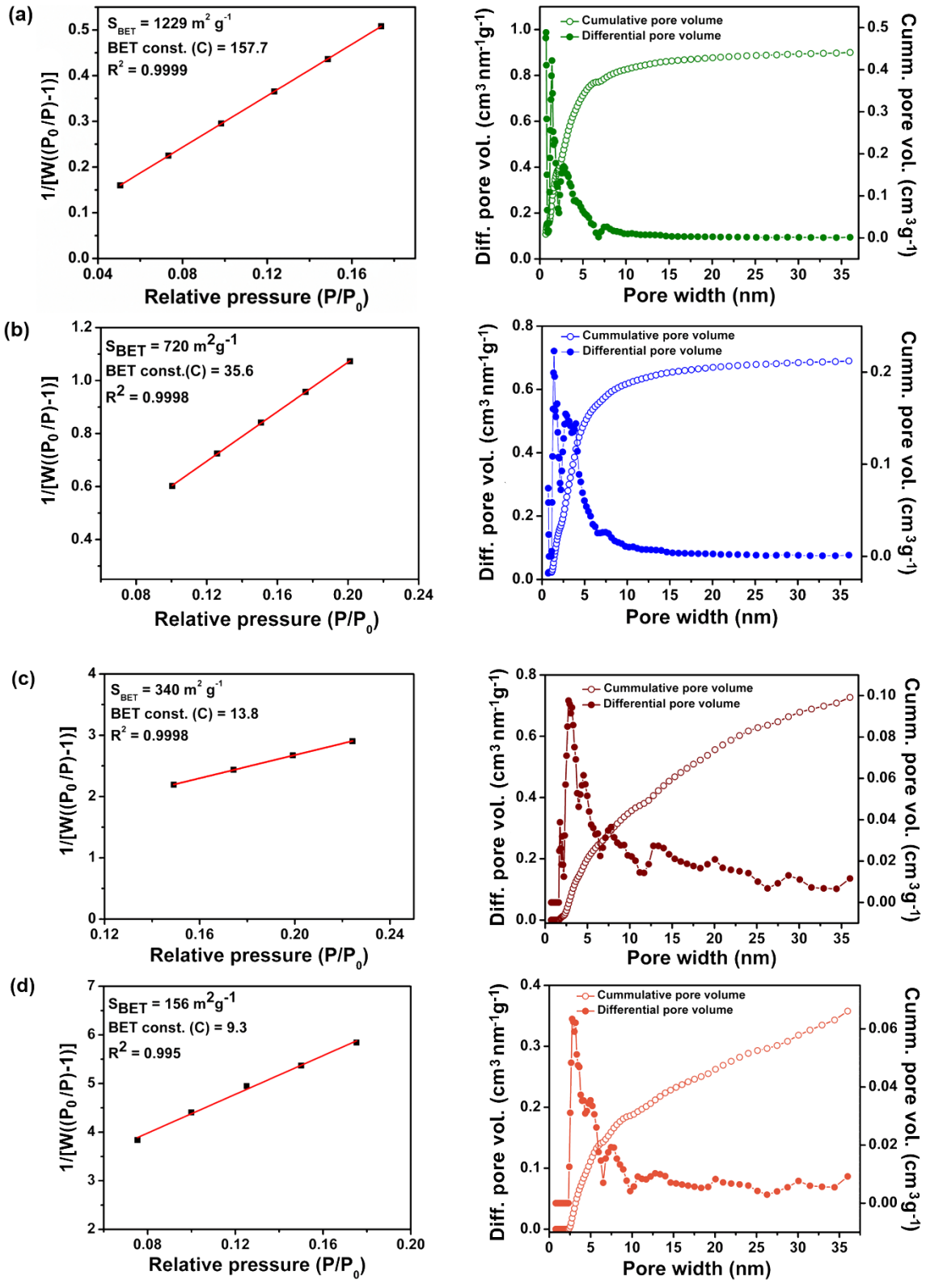

Figure S11. The BET specific surface area plot (left) and NLDFT pore size distribution (right) of (a) RN4-Az-OH, (b) RN4-OH, (c) RN4-F, and (d) HRN4 calculated using N_2 sorption profile.

3.9. Cavity of resorcin[4]arene and pore size distribution of POPs

The pore size distribution (PSD) profiles were estimated through non-local density functional theory (NLDFT, using carbon, slit pore model) method (Figure 3f, S11). We found that the pristine cavitand showed the pores of 2.4 to 6 nm (Figure S11d). These are the extrinsic voids originated from the packing of the resorcin[4]arene monomers in the solid state. However, from the crystal structure analysis of *p*-hydroxyphenylresorcin[4]arene, we found the size of the cavity is of ~ 1.25 nm width and ~ 1.17 nm deep (inner ring diameter ~ 0.72 nm).[14] The nearly similar size of the cavity of metal-coordinated calix[4]resorcinarene cavitands was also reported in literature (cavity diameters:1.62-1.83 nm).[15] In the solid state, the cavities of the pristine macrocycles remain inaccessible, and only the extrinsic voids are contributing to the PSD.[16] On the other hand, connecting the macrocyclic cavitands with aromatic linkers leads to the interconnected porous 3D networks. The interconnectivity between the pores in the network makes the intrinsic cavity of the macrocyclic building blocks accessible to the guests. The peaks emerging in the range of 1.4 – 1.6 nm in the PSD profiles of RN4-Az-OH, RN4-OH, and RN4-F are clearly noticeable, which are contributed by the intrinsic pores of resorcinarene. As a consequence, a large increase in the specific surface area was observed.

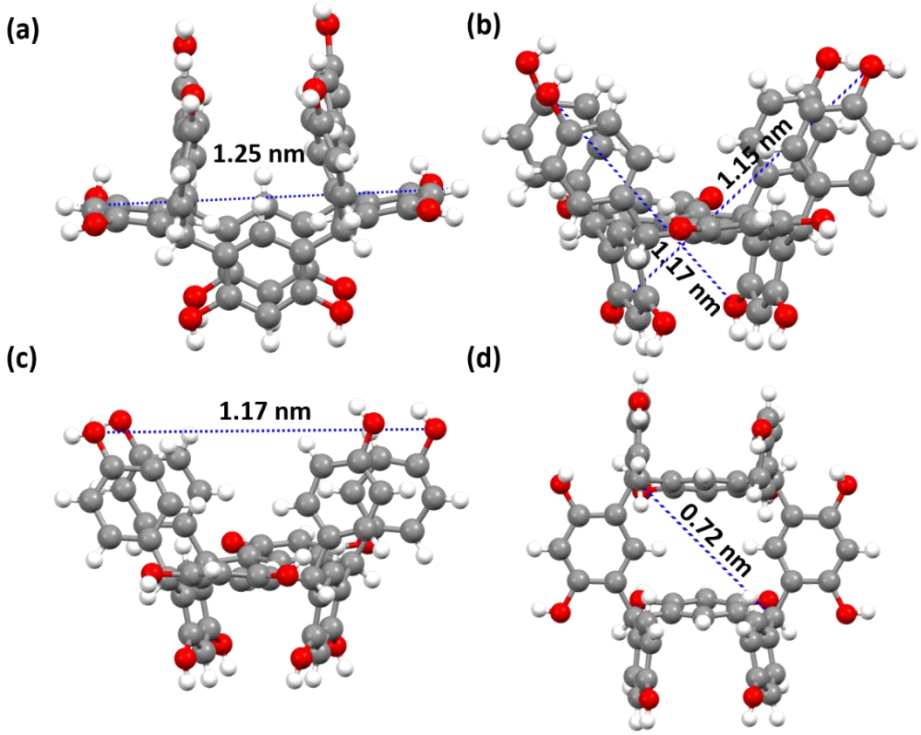

Figure S12. (a-d) Crystal structure of HRN4 analyzed using the software package in Mercury 4.1.2 revealing the dimension of *p*-hydroxyphenylresorcin[4]arene (CCDC No. 1477373).[14]

4. CO_2 and H_2 uptake

The carbon dioxide sorption isotherms of the POPs were measured at 273 K as well as 298 K to calculate the isosteric heat of adsorption (Q_{st}). The isotherms at 298 K are shown in Figure S13a. The hydrogen sorption isotherms for all the POPs were measured at 77 K (Figure S13c). The microporous nature (type Ib H_2 sorption isotherm), as well as high surface area, facilitate the high H_2 uptake in RN4-F and RN4-OH over that of RN4-Az-OH. H_2 having small kinetic diameters (2.89 Å) are effectively adsorbed by smaller pores.[12]

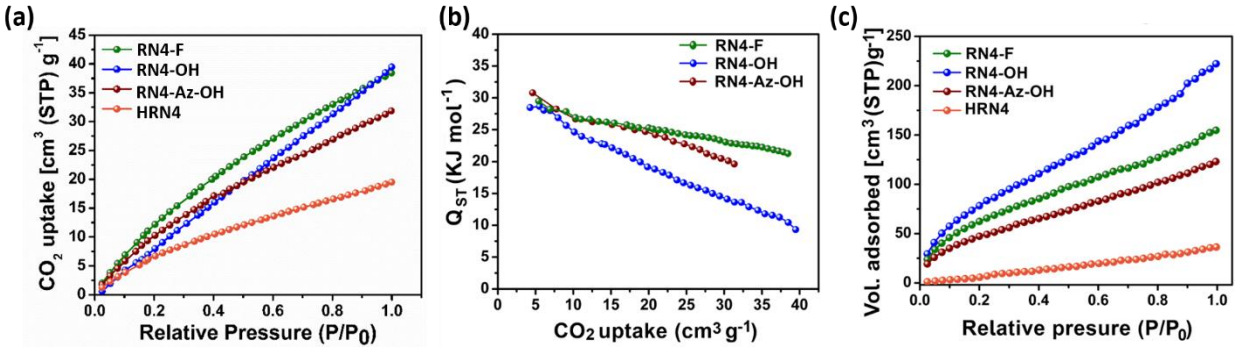

Figure S13. (a) CO_2 sorption isotherms at 298 K. (b) The isosteric heat of adsorption (Q_{st}) profiles of RN4-F, RN4-OH, and RN4-Az-OH. (c) H_2 sorption isotherms of RN4-F, RN4-OH, RN4-Az-OH, and HRN4 at 77 K.

The hysteresis behavior of the RN4-based POPs (Figure 3g, main text) in the CO_2 sorption isotherms is due to the inherent flexibility in the network structure (elastic deformations due to the swelling nature of the polymers during the gas sorption).[17,18] At the same time, the high heat of adsorption (Q_{st}: 28.5-30.8 kJ mol^{-1}) of all the RN4-based POPs for the CO_2 also indicates strong host-guest electrostatic interactions between CO_2 and various functional groups (-OH, -N=N-, -F) present in the POPs. Hence, apart from the change in the pore channel topology during gas sorption (network flexibility), the strong interactions between the CO_2 and pore functionalities also contribute in the open-ended hysteresis loop.[19]

4.1. Isosteric heat of adsorption

The interactions of CO_2 with pores of POPs having diverse functionality can be elucidated by calculating isosteric heat of adsorption. Isosteric heat of adsorption (Q_{st}) is the standard enthalpy of adsorption at fixed surface coverage. The Q_{st} for CO_2 was calculated from the adsorption

isotherms measured at 273 K and 298 K considering the fixed amount of adsorbate using the Clausius-Clapeyron equation.

$$\ln\left(\frac{P_1}{P_2}\right) = \frac{\Delta H_{ads}}{R}\left(\frac{1}{T_2} - \frac{1}{T_1}\right) \qquad (2)$$

where P_1 and P_2 are the pressure for the same volume of the gas adsorbed at two different temperatures, T_1 and T_2, respectively. ΔH_{ads} (or, Q_{st}) gives the isosteric heat of adsorption (Figure S13b). The rate of decrease in Q_{st} of RN4-OH is higher than that of RN4-F due to the larger pores in the former (Figure S13b).

4.2. Selectivity in CO_2 uptake

Ideal adsorbed solution theory (IAST) developed by Myers and Prausnitz enables accurate prediction of adsorption of the binary gas mixture on porous materials, using single component isotherms.[20] Adsorption selectivity (S_{ads}) for binary mixtures is defined as follows.

$$S_{ads} = \frac{q_1/q_2}{p_1/p_2} \qquad (3)$$

where q_i is the amount adsorbed at partial pressure p_i of the i^{th} gas in the binary mixture. To calculate the selectivity for CO_2 over N_2, partial pressures are taken as 0.15 and 0.85 for CO_2 and N_2, respectively as the flue gas contains approximately 15% of CO_2. The corresponding selectivity values for RN4-F, RN4-OH, and RN4-Az-OH at 273 K were found to be 35, 20, 19, respectively (Figure S14).

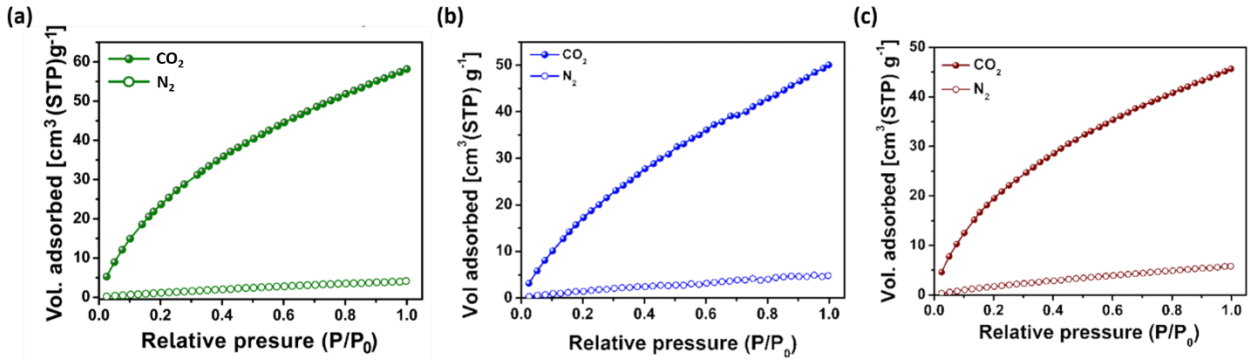

Figure S14. The comparison of CO_2 and N_2 uptake by (a) RN4-F, RN4-OH and (b) RN4-Az-OH at 273 K.

5. Residual palladium in RN4-OH

5.1. Estimation of residual palladium

The presence of trace-amount of residual palladium in RN4-OH plays a key role in the gas uptake as well as catalytic performance.[21] During the course of the polymerization, the phenolic OH groups in RN4-OH can effectively chelate with palladium.[22] After the Soxhlet purification in common organic solvents (MeOH, THF, $CHCl_3$, EtOH), the amount of residual Pd left, was estimated by EDS analysis (Figure S15a). The results showed the presence of Pd in the POP (first batch: 1.2 wt%, second batch: 1.0 wt%, third batch: 1.4 wt%). The PXRD pattern of RN4-OH exhibited the characteristic peak at $2\theta = 40°$ corresponding to the Pd (111) plane (Figure S7b). Due to the low loading of Pd, no other obvious diffraction peaks for Pd nanoparticles (NPs) were observed.[23] Pd NPs were distributed throughout the matrix of RN4-OH as evident by the EDS mapping and HRTEM analysis (Figure S15-S16). The size distribution of the Pd nanoparticles was found to be in the range of 2.5 to 7 nm.

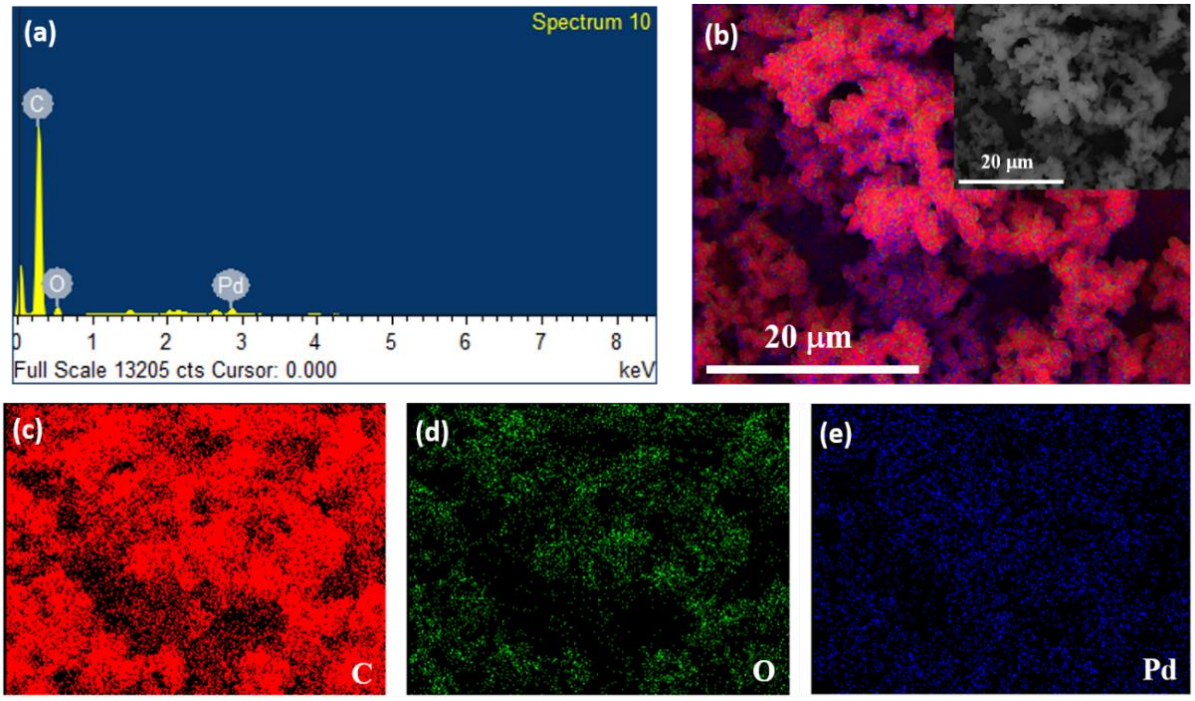

Figure S15. (a) EDS profile of RN4-OH**.** (b) EDS mapping of carbon, oxygen, and palladium through FESEM imaging. EDS mapping of individual elements: (c) carbon, (d) oxygen, and (e) palladium.

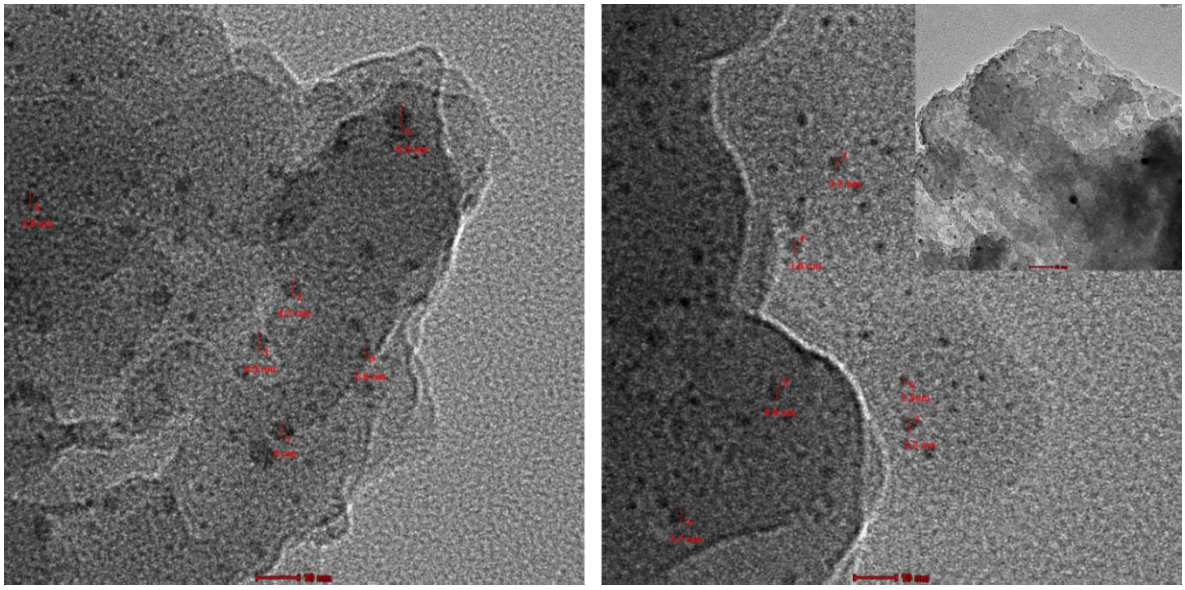

Figure S16. TEM images (scale bar = 10 nm) of RN4-OH showing the presence of Pd particle (size: 2.5 - 7 nm, inset: larger area image, scale bar = 50 nm).

5.2. Reduction of *p*-nitrophenol

The presence of palladium in RN4-OH was further substantiated by probing the catalytic reduction of *p*-nitrophenol. The aqueous solution of *p*-nitrophenol (0.1 mM, 0.3 mL), aq. sodium borohydride (0.5 M, 1 mL) and 1 mL water were added to a cuvette. A suspension of RN4-OH in water (1 mg mL^{-1}, 50 μL) was added, and the progress of the reaction at room temperature was monitored through UV/vis spectroscopy (decrease of absorbance at 400 nm). 95% conversion was observed in 20 mins (Figure S17). The reduction does not proceed only with aq. $NaBH_4$.

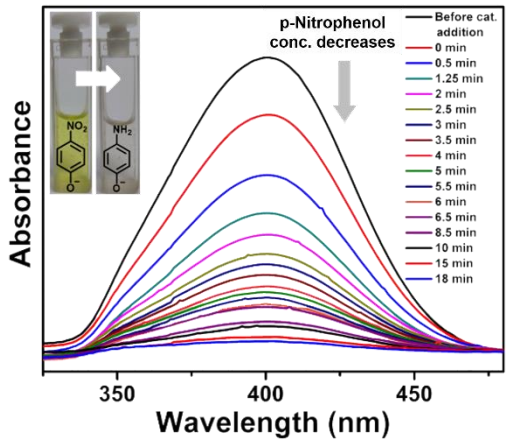

Figure S17. Time-dependent UV/Vis spectra of the reduction of *p*-nitrophenol (0.1 mM) catalyzed by 50 μL aqueous dispersion of RN4-OH (1 mg mL^{-1}).

6. Dispersity of POPs

6.1. Dispersity of RN4-Az-OH in common organic solvents and water

RN4-Az-OH was dispersed in various solvents (different polarity) by sonicating it for 30 min. The dispersions were stable in polar solvents (e.g., water, DMSO, ACN, MeOH, etc., Figure S18).

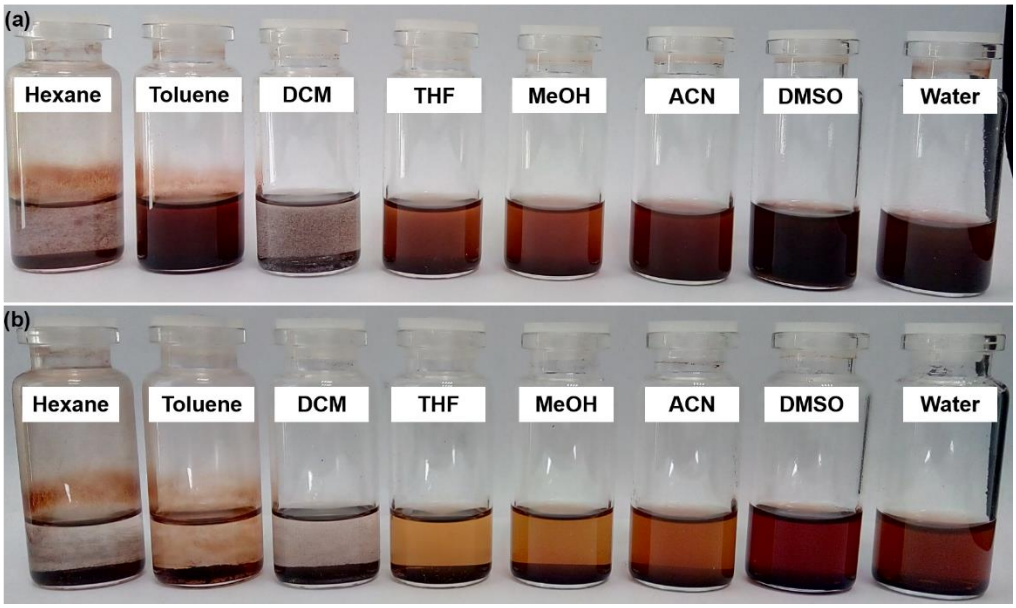

Figure S18. Dispersity of RN4-Az-OH in common solvents after (a) 1 h, and (b) 14 days.

6.2. Zeta potential of POPs

POPs were dispersed in water (1 mg mL^{-1}) through sonication for 30 min. The high negative zeta potential of the aq. dispersion of RN4-Az-OH in neutral pH compared to the other POPs indicates the stability of the dispersion in water (Table S2). The Tyndall effect shown by the aqueous dispersion of RN4-Az-OH (0.025 mg mL^{-1}) also indicates the stable colloidal nature of the dispersion (Figure S19).

Table S2 Zeta potential of RN4-F, RN4-OH and RN4-Az-OH dispersion in water.

Entry / POP	1 (mV)	2 (mV)	3 (mV)	Avg. (mV)	Remarks
RN4-F	-1.68	-2.2	-1.81	-1.89	Unstable dispersion
RN4-OH	- 3.97	-6.2	-4.6	-4.9	Unstable dispersion
RN4-Az-OH	-28.8	-30.4	-38.3	-32.5	Stable dispersion

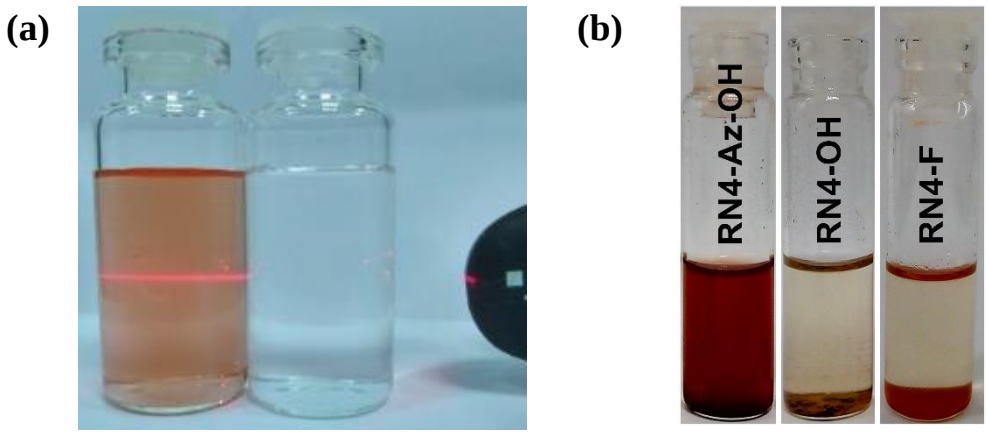

Figure S19. (a) The aqueous dispersion of RN4-Az-OH (left) comparing with water (right) exhibiting the Tyndall effect. (b) Dispersion of POPs (1 mg mL^{-1}) in epichlorohydrin after 12 h.

.

6.3. Interaction of *tert*-n-butylammonium bromide with RN4-Az-OH

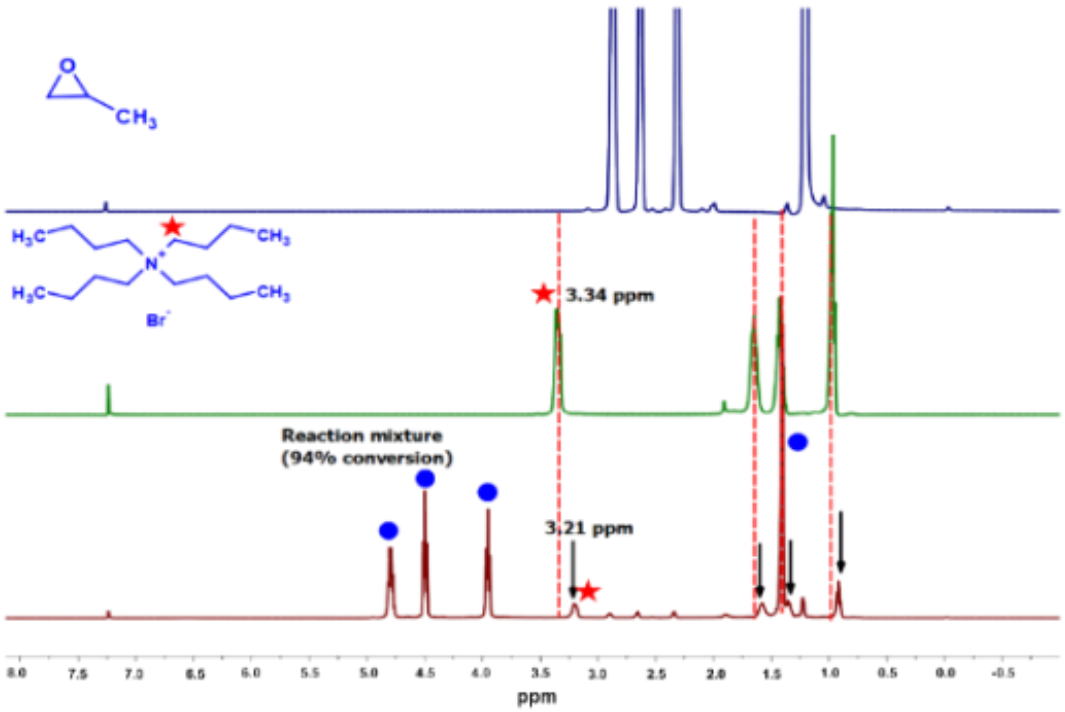

Figure S20. The upfield ^{1}H-NMR shift of methylene protons of TBAB (red star, 3.34 ppm to 3.21 ppm) in the reaction mixture indicates the encapsulation of cationic *tert*-n-butyl ammonium group in porous RN4-Az-OH which improves the nucleophilicity of bromide (Br^{-}) ion. The blue circles indicate the peaks of propylene carbonate formed due to the cycloaddition of propylene oxide with CO_2.

7. Synthesis and characterization of RN4-Az-OR & Zn/RN4-Az-OH

(i) Fabrication of RN4-Az-OR

RN4-Az-OR was synthesized following a reported protocol.[24] Triethylamine (1 mL) was added to a suspension of RN4-Az-OH (100 mg) in epichlorohydrin (10 mL). The reaction mixture was heated at 100 °C for 48 h. After cooling to room temperature, the solid was filtered out and washed several times with methanol and ethanol. The reddish-brown color solid was dried under vacuum at 80 °C for 12 h.

(ii) Fabrication of Zn/ RN4-Az-OH

A mixture of RN4-Az-OH (100 mg) and $Zn(OAc)_2.2H_20$ (50 mg) in absolute ethanol (5 mL) was refluxed under nitrogen atmosphere for 12 h. After cooling down to room temperature, the filtered solid was washed with Soxhlet extraction in methanol and ethanol for 24 h and dried under vacuum at 85 °C for 24 h.

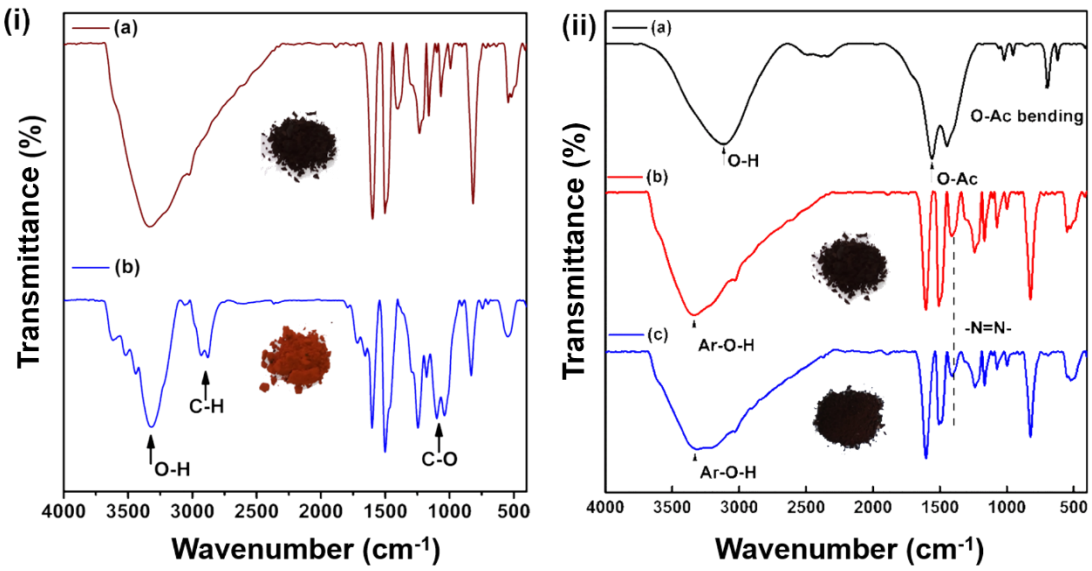

Figure S21. (i) FTIR spectra of (a) RN4-Az-OH and (b) RN4-Az-OR. (ii) FTIR spectra of (a) $Zn(OAc)_2.2H_2O$, (b) RN4-Az-OH and (c) Zn/RN4-Az-OH.

The FTIR spectrum indicates the band at 1102 cm^{-1}, corresponding to the C-O stretching of ether linkage in RN4-Az-OR. The appearance of an alkyl C-H vibration (2870–2940 cm^{-1}) is clear evidence of successful incorporation of the -OR group. On the other hand, the absence of O-Ac bending at 694 cm^{-1} and stretching at 1560 cm^{-1} in Zn/RN4-Az-OH indicated that $Zn(OAc)_2$ was

completely converted to ZnO (Figure S21). Further, the PXRD pattern indicates the formation of ZnO particles embedded on the porous polymer (Figure S22a). Peaks at 31.6, 34.3, 36.2, 47.5, 56.5, 62.8, 67.9, 69 correspond to (100), (002), (101), (102), (110), (103), (112), and (201) planes of ZnO, respectively.[25] The EDS analysis indicates the presence of Zn (7.7 wt%, Figure S22c), and the result is also corroborated with the TGA data (7 wt%, Figure S22b). FESEM and TEM analysis of Zn/RN4-Az-OH revealed the formation of spherical submicron-sized zinc oxide particles (Figure S23).[25]

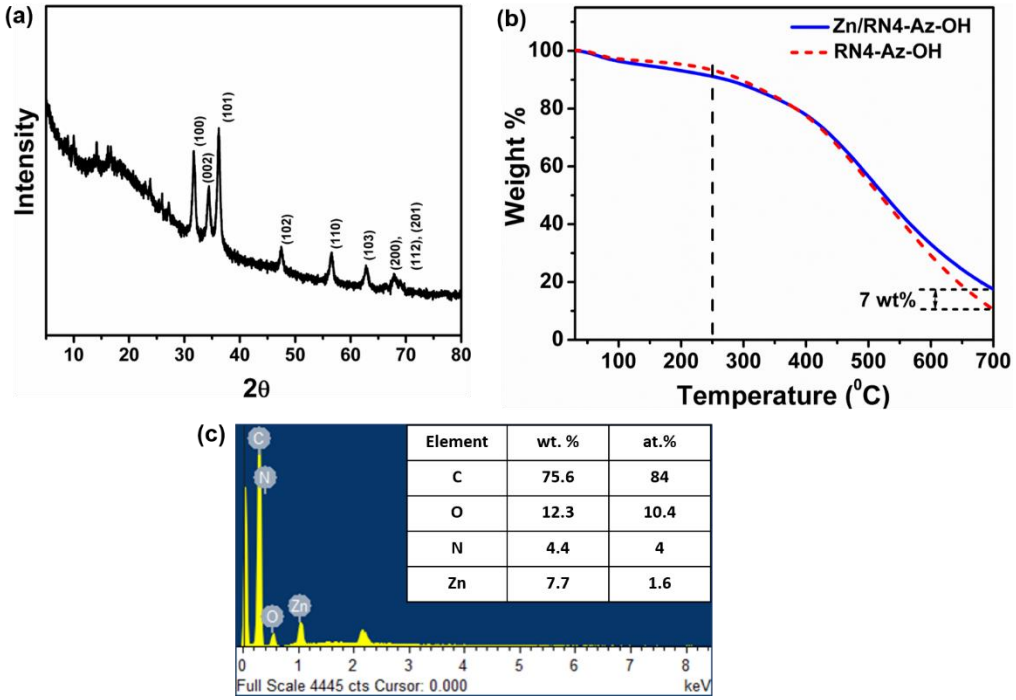

Figure S22 (a) PXRD profile of Zn/RN4-Az-OH indicating the formation of ZnO. (b) TGA of Zn/RN4-Az-OH and RN4-Az-OH indicating the thermal stability of the catalyst up to 250°C. (c) EDS profile of Zn/RN4-Az-OH.

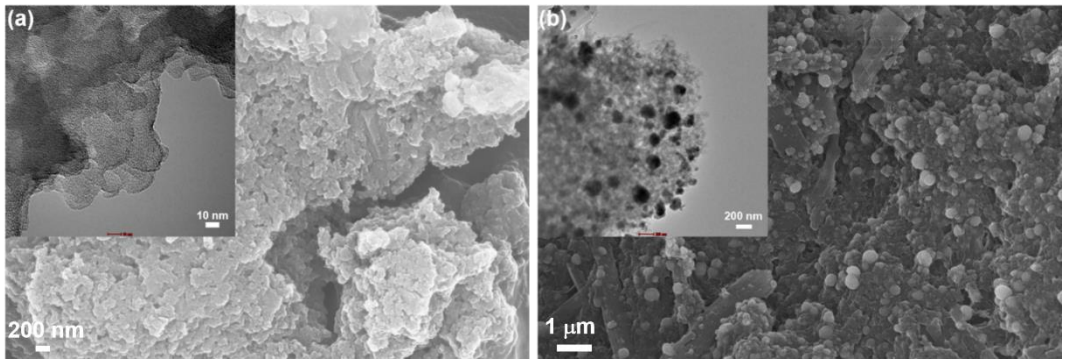

Figure S23. FESEM images (inset: TEM images) of (a) RN4-Az-OR and (b) Zn/RN4-Az-OH.

The specific surface areas of RN4-Az-OR and Zn/RN4-Az-OH were found to be 56 m^2 g^{-1} and 198 m^2 g^{-1} which are lower than that of the pristine POP, RN4-Az-OH (340 m^2 g^{-1}). The decrease in the specific surface area of RN4-Az-OR was due to the substitution by bulky alkoxy groups rendering to pore blocking.[26] Metalation of RN4-Az-OH also caused partial filling of the pores (Figure S24).[27]

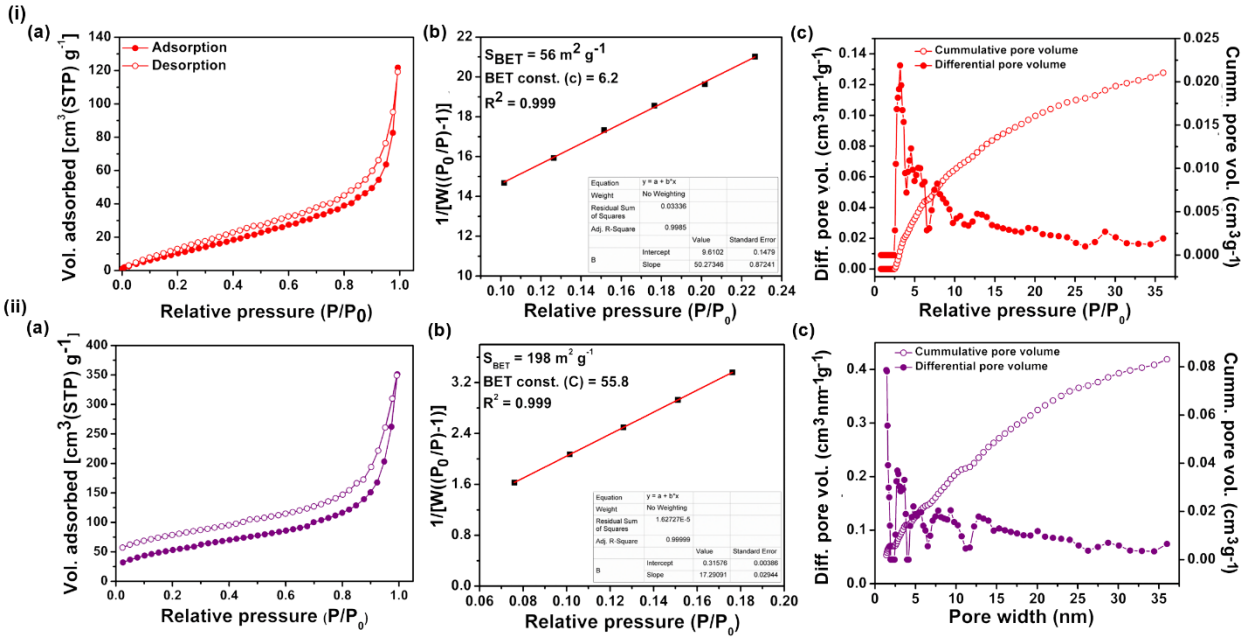

Figure S24. (a) N_2 adsorption-desorption isotherms, (b) the BET specific surface area plot and (c) NLDFT pore size distribution of (i) RN4-Az-OR and (ii) Zn/RN4-Az-OH.

8. CO_2 conversion

8.1. CO_2 fixation to cyclic carbonates

Cyclic organic carbonates have numerous applications as polycarbonate precursors, fuel additives, electrolytes for Li-ion battery, drug precursors, and polar aprotic solvents.[28] The % of conversion of various epoxides to carbonates catalyzed by POPs was calculated from the ^{1}H NMR spectra by integrating the peaks of epoxide vs. cyclic carbonate (Figure S54-S68). We selected styrene oxide (boiling point: 194 °C) as the model substrate to optimize the reaction conditions for the catalytic conversion of CO_2 and epoxide into cyclic carbonates. The RN4-based POPs in the absence of cocatalyst (TBAB) did not show any catalytic activity justifying the role of cocatalyst (nucleophile, Br^-) as depicted in the mechanism (Figure 4d). However, employing only TBAB (0.15, 0.25, 0.5 mmol), the catalytic conversion of styrene oxide (10 mmol) in 12 h (2.5 bar CO_2 and 90 °C) was found to be very low (15, 25 and 40, respectively) indicating the importance of POPs as catalysts. Again, the metalation of RN4-Az-OH with $Zn(OAc)_2$ enhanced the catalytic performance (% of conversion of styrene oxide (10 mmol) was increased from 76% to 98% in 6 h, Figure S68). The isolated yields of cyclic carbonates were determined after silica gel column purification (Figure S44-S53).

Table S3 CO_2 fixation with various epoxide derivatives to cyclic carbonates on a larger scale.

Entry	Epoxide	Product	% Conversion[#]		
			RN4-Az-OH	Zn/RN4-Az-OH	
1			[a]98 (90)	[b]99 (90)	[d]99*
2			[a]97 (92)	[b]99 (88)	[d]99*
3			[a]77 (69)	[c]86 (76)	[c]98*
4		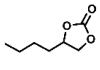	[a]65 (60)	[c]99 (92)	[c]99*
5	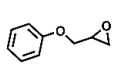	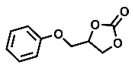	[a]71 (67)	[c]86 (80)	[c]99*

Reaction conditions: Epoxide (20 mmol), TBAB (0.12 mmol), CO_2 (2.5 bar), 90 °C, catalyst (RN4-Az-OH or, Zn/RN4-Az-OH: 30 mg). Reaction time: [a]12 h, [b]4 h, [c]6 h, [d]3h.

[*]Epoxide (10 mmol). TBAB (0.25 mmol), CO_2 (2.5 bar), 90 °C, comparing the catalytic conversion by RN4-Az-OH (Figure 4a).

Isolated yields were estimated after silica gel column purification and reported inside the parentheses. [#]% of conversion calculated through ^{1}H NMR analysis.

8.2. Recyclability of Zn/RN4-Az-OH

The % of conversion of epoxide (epichlorohydrin, 20 mmol, 4 h, measured by ^{1}H NMR) employing Zn/RN4-Az-OH was decreased up to 73% at the 7th cycle due to the leaching of metal. ZnO was further loaded with the recycled catalyst following the same protocol, and the performance of the catalyst was checked. After the metal loading, the catalyst showed similar performance compared to that of the pristine Zn/RN4-Az-OH (Figure S25).

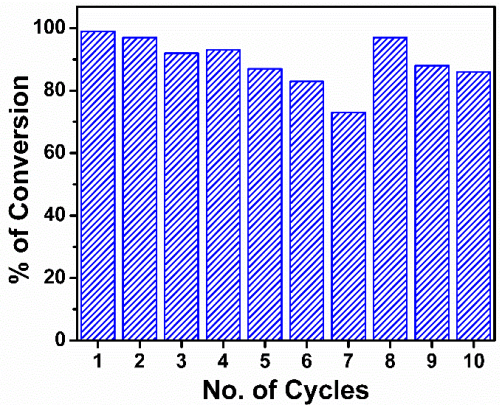

Figure S25. Recyclability of Zn/RN4-Az-OH for CO_2 conversion; the % of conversion is decreased up to 73% in the 7th cycle. The efficiency of the recovered catalyst was further regained upon metal-loading.

8.3. Stability of the RN4-Az-OH and Zn/RN4-Az-OH after recycling

The FTIR spectrum of the recycled catalyst was almost similar to that of the pristine one indicating the stability of the catalyst. However, the presence of a small peak at 1798 cm^{-1} was attributed to the carbonyl stretching of cyclic carbonate (product) which may be trapped in the POPs (Figure S26).

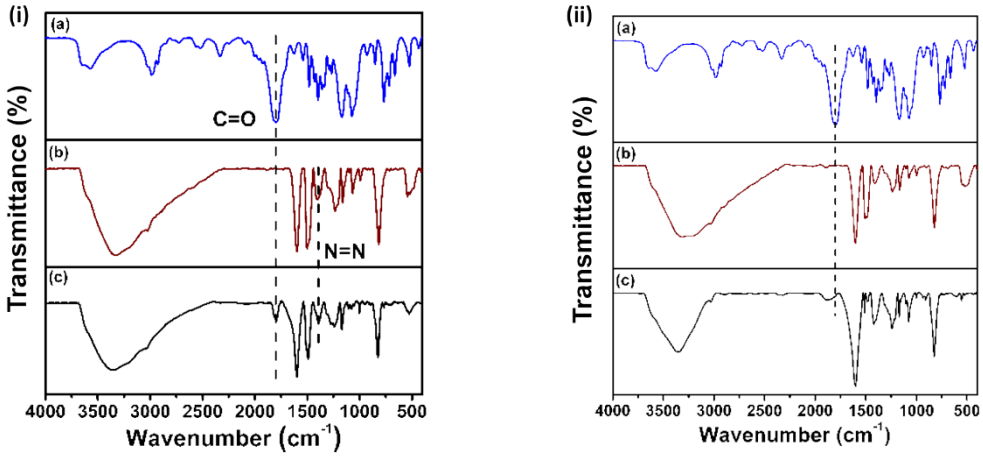

Figure S26. (i) FTIR spectra of (a) 4-(chloromethyl)-1,3-dioxolan-2-one, (b) pristine RN4-Az-OH and (c) RN4-Az-OH after 10th-time recycling. (ii) FTIR spectra of (a) 4-(chloromethyl)-1,3-dioxolan-2-one, (b) pristine Zn/RN4-Az-OH (c) Zn/RN4-Az-OH after 7th-time recycling.

9. Removal of organic micropollutants from water

Organic micropollutants are a diverse set of analytes including pesticides, pharmaceuticals, ingredients of personal care products and toxic dyes which pose a serious threat to human health and aquatic lives.[29] Many of these dyes have carcinogenic, teratogenic and mutagenic properties. Especially, dyes discharged from the textile industries, have high chemical and photolytic stability and therefore, difficult for biodegradation. Methylene blue is one such important dyes used for printing calico, dying leather and cotton, and has an adverse effect on the central nervous system.[30,31] Apart from that, it can cause eye burn and irritation to the gastrointestinal tract. The conventional adsorbents, such as activated carbons, possess several bottlenecks: (i) poor removal efficiency towards highly soluble dyes, (ii) slower uptake (of the order of hours), (iii) nonselective towards the micropollutants and (iv) tedious regeneration process (heating up to 500 – 900 °C) with a steady decrease in the efficiency. In this respect, hydrothermally robust cavitand-based POPs having high pore volume can be the potential candidates for the removal of soluble micropollutants from water. We selected methylene blue as a model micropollutant. RN4-F having a high specific surface area (1230 m^2 g^{-1}) with fluorine-rich hydrophobic network, can adsorb methylene blue without any mechanical agitation (Figure S27).

Figure S27. The visual color change of methylene blue solution (0.1 mM) by soaking with RN4-F (1 mg mL^{-1} dispersion).

9.1. Interaction of methylene blue with RN4-F

The specific interaction between MB and fluorine in RN4-F was confirmed by the FTIR spectroscopy (Figure S28). The peak due to the F-phenyl ring bending at 652 cm^{-1} completely disappeared after MB adsorption. This may be due to the hindrance to the bending of C-F bond angle because of favorable binding of MB with fluorine in RN4-F.

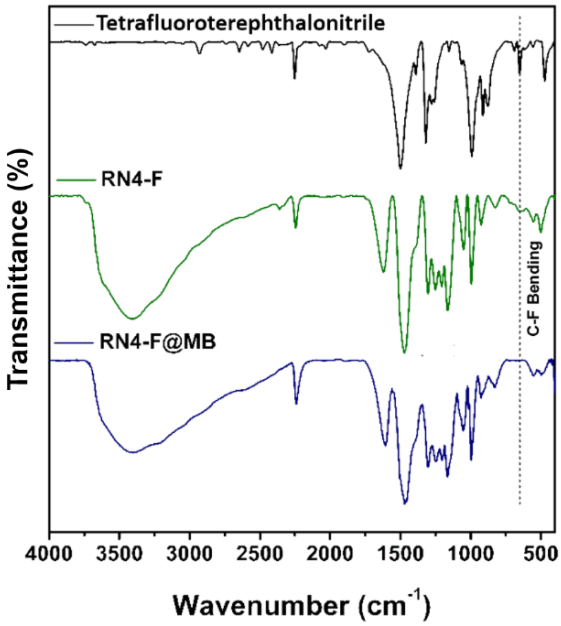

Figure S28. Change in the FTIR spectra of RN4-F after the adsorption of MB molecule.

9.2. Percentage removal efficiency of RN4-F

In the batch adsorption experiment, the initial concentration of dyes was 0.1 mM. 10 mg of POP was added into 10 mL of the dye solution. The mixture was sonicated for 10 s, and then it was stirred at 800 rpm. After 30 min, the mixture was filtered through Whatman 0.45 μm membrane filters attached to a syringe. The concentration of the dye in the filtrate was measured using the UV/vis. spectroscopy. The percentage removal efficiency of the micropollutants was calculated following the equation:

$$\text{Removal efficiency (\%)} = \frac{(C_0 - C_t)}{C_0} \times 100 \qquad (4)$$

where C_0 and C_t are the initial and final concentration (after 30 min) of dye, respectively.

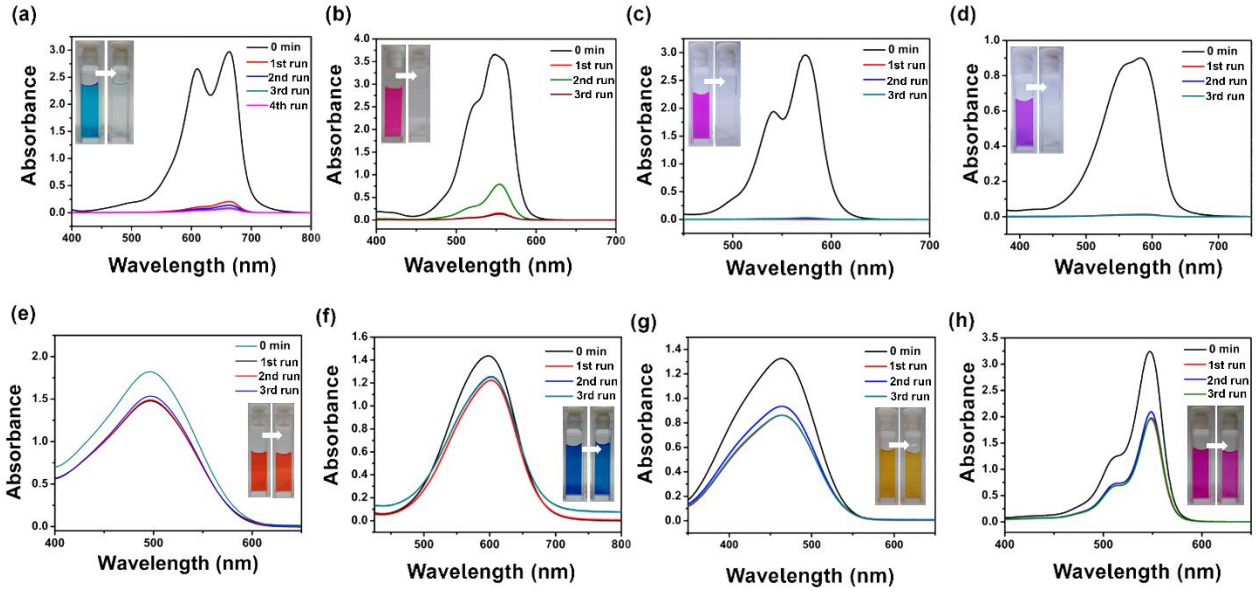

Figure S29. UV-Vis absorption spectra of cationic dyes (0.1 mM) (a) methylene blue, (b) rhodamine B, (c) rhodamine 101, (d) cresyl violet and anionic dyes (0.1 mM) (e) Congo red, (f) methyl blue, (g) methyl orange, (h) rose bengal at 30 min time interval (three/four independent measurements, each run for 30 min) in presence of RN4-F (1 mg mL^{-1}).

We found that ~ 95% of all the cationic dyes (0.1 mM) were removed by RN4-F (Figure S29). Whereas, at lower initial dye concentration (0.05 mM), the same removal efficiency was obtained within 15 min. Apart from water-soluble cationic/anionic dyes, neutral small molecules like *p*-nitrophenol (0.1 mM), 2-naphthol (0.1 mM) were removed up to 80% and 76 %, respectively by RN4-F (1 mg mL^{-1}) within 30 min (Figure S30).

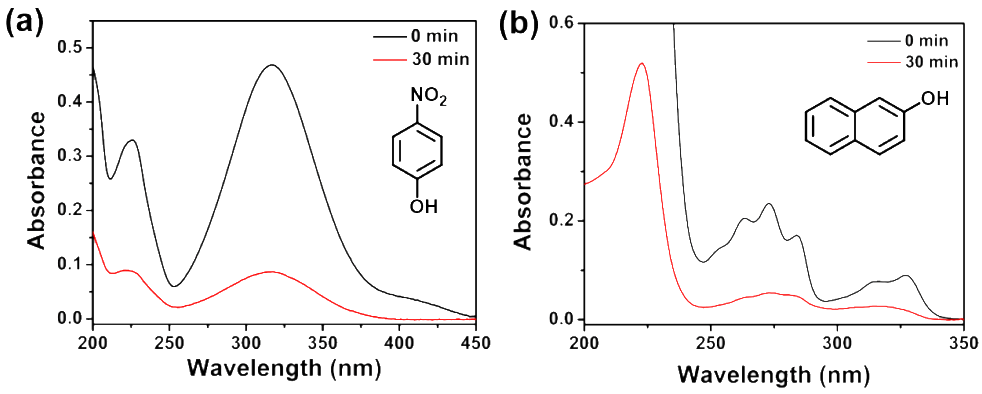

Figure S30. UV-Vis absorption spectra of (a) *p*-nitrophenol (0.1 mM), (b) 2-naphthol (0.1 mM) in water at 30 min time interval in the presence of RN4-F (1 mg mL^{-1}).

9.3. Calculation of the dimensions of model micropollutants

The size of the micropollutants was estimated by density functional theory (DFT) calculations and modelled using Materials Studio version 6.1. All the molecular structures are displayed in space-filling style (Figure S31).

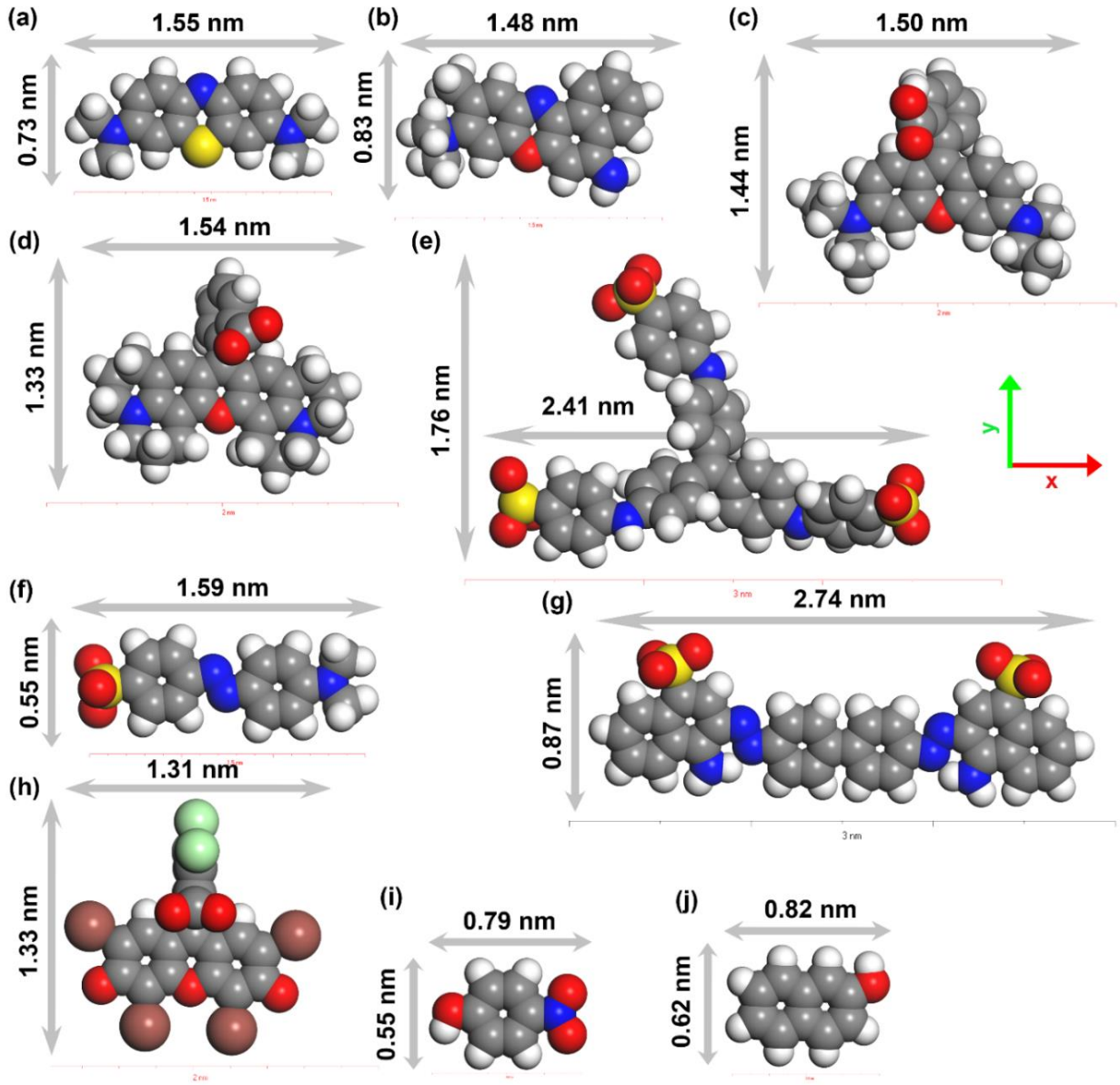

Figure S31. Dimensions of model cationic, anionic and neutral micropollutants: (a) methylene blue, (b) cresyl violet, (c) rhodamine B, (d) rhodamine 101, (e) methyl blue, (f) methyl orange, (g) Congo red, (h) rose bengal, (i) *p*-nitrophenol and (j) 2-naphthol along x- and y-direction, obtained through ground-state geometry optimized structures using density functional theory (DFT) at B3LYP/6-31G (d,p) level employing the polarizable continuum model (PCM) (gray: carbon; red: oxygen; white: hydrogen; blue: nitrogen; green: chlorine; yellow: sulfur, brown: bromine).

9.4. Kinetic analysis of micropollutant uptake

The study of sorption kinetics in water treatment is important as it gives valuable insight into the reaction pathways and the mechanism of sorption. Various models were proposed to analyze the kinetics of the sorption process. Lagergren proposed a pseudo-first order model for the sorption of solutes from a solution as follows.[32]

$$\ln(q_e - q_t) = \ln q_e - k_1 t \qquad (5)$$

Where q and q_e are the grams of solute adsorbed per gram of sorbent at any time and equilibrium, respectively, and k_1 is the of pseudo-first order rate constant.

Another model for the analysis of sorption kinetics is the pseudo-second-order model which was applied by Ho and McKay.[33]

$$\frac{t}{q_t} = \frac{1}{k_2 q_e^2} + \frac{t}{q_e} \qquad (6)$$

Where k_2 is the pseudo-second order rate constant of sorption.

The kinetic studies of dye adsorption were carried out taking methylene blue (MB) and rhodamine B (RhB) as model pollutants. The kinetic data were fitted with both the pseudo first and pseudo second-order kinetic models (Figure S32, S33). However, the adsorption of methylene blue and rhodamine B by RN4-F was best fitted with the pseudo second-order kinetic model with a high correlation coefficient (R^2, Figure S32).

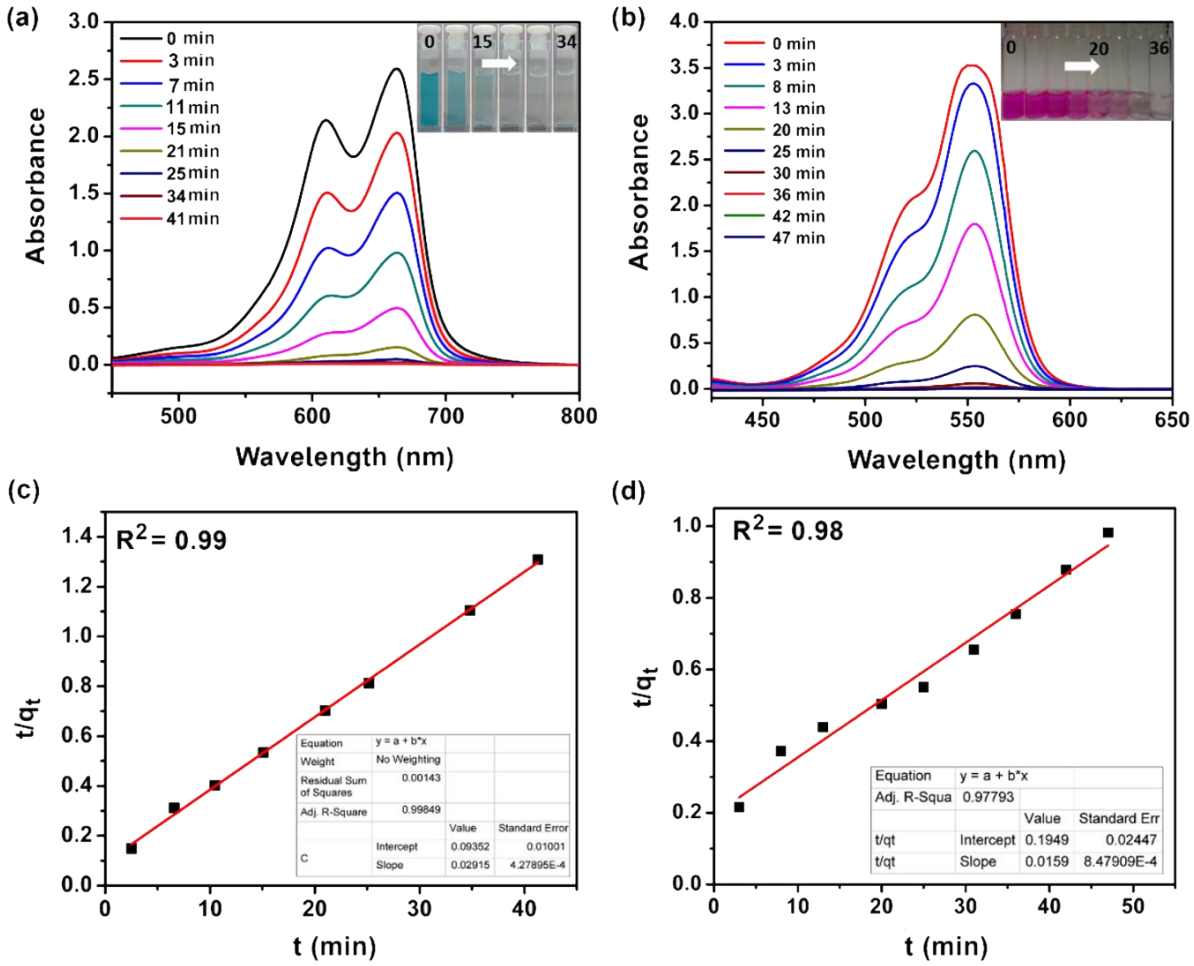

Figure S32 UV/Vis absorption spectra of cationic dyes (a) methylene blue (0.1 mM), (b) rhodamine B (0.1 mM) at different time (min) interval in the presence of RN4-F (1 mg mL^{-1}) in water. The pseudo second-order fitting for the kinetics of adsorption of (c) methylene blue and (d) rhodamine B by RN4-F.

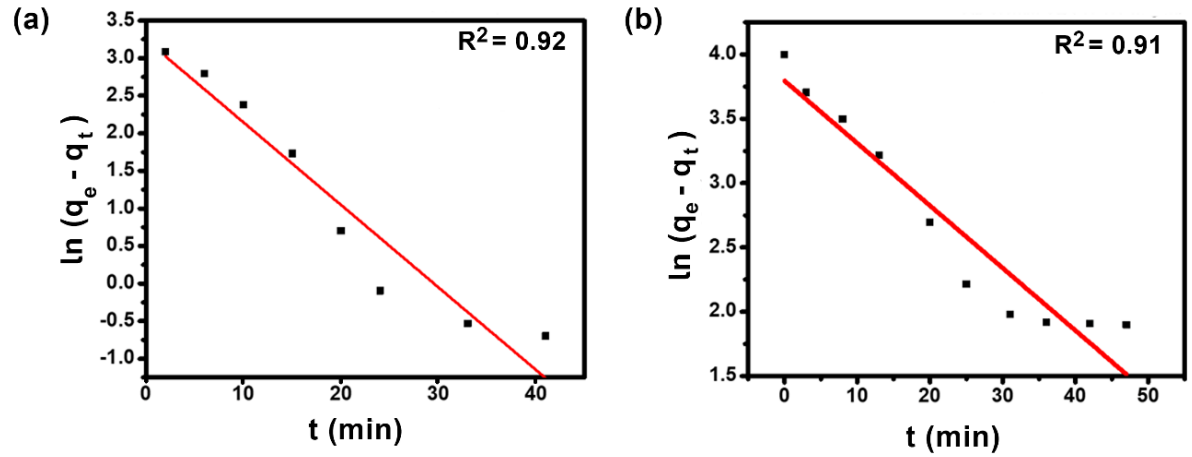

Figure S33. Pseudo first order fitting of (a) methylene blue (0.1 mM, R^2 = 0.92), (b) rhodamine B (0.1 mM, R^2 = 0.91) at different time interval in the presence of RN4-F (1 mg mL^{-1}).

The kinetic model was substantiated through the variation of the pseudo-second order rate constant (k_2) with the change in the initial dye concentration (0.1, 0.08 and 0.05 mM) as well as the adsorbent amount (1 and 0.5 mg mL^{-1}). The rate constant was found to decrease with the increase in the initial dye concentration (Figure S34, Table S4). The plausible explanation could be due to the higher degree of competition among the dye molecules for the surface-active sites.[34] The similar trend was observed by changing the adsorbent amount. The results indicate that the adsorption process is dependent on both the adsorbent and adsorbate.

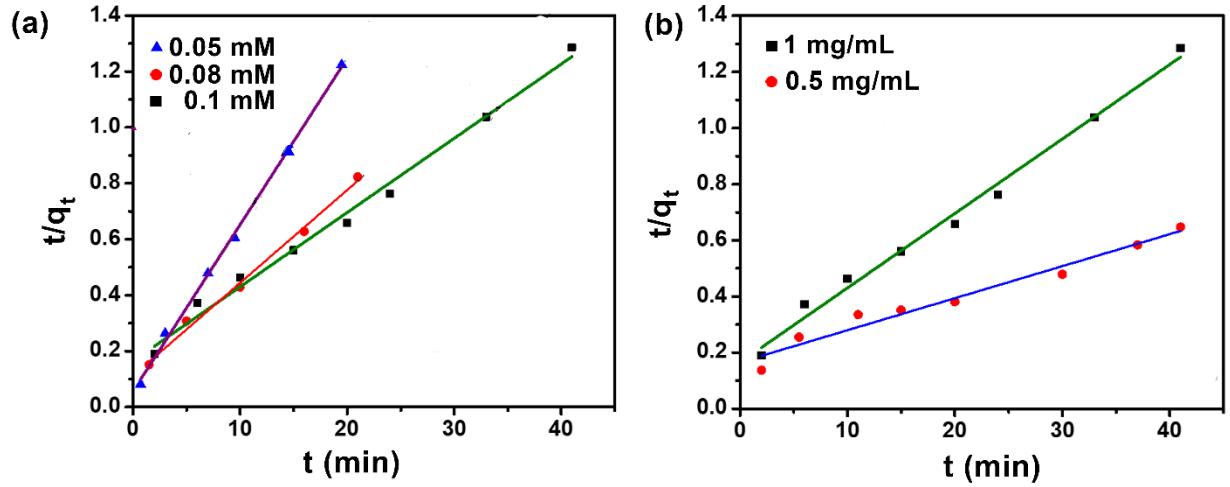

Figure S34 Pseudo second-order fitting of adsorption of (a) methylene blue (0.1 mM, 0.08 mM, 0.05 mM) by 1 mg mL^{-1} of RN4-F and (b) methylene blue (0.1 mM) by 1 and 0.5 mg mL^{-1} of RN4-F in water.

Table S4. Equilibrium uptake and pseudo second-order rate constant of RN4-F for methylene blue uptake.

Adsorbent amount (mg mL^{-1})	Initial dye concentration (mM)	R^2	q_e (mg g^{-1})	k_2 (g mg^{-1} min^{-1})
1	0.05	0.99	16.8	6.1×10^{-2}
1	0.08	0.99	30.1	9.8×10^{-3}
1	0.1	0.99	37.7	4.2×10^{-3}
0.5	0.1	0.96	87.6	7.9×10^{-4}

9.5. Thermodynamic study of dye adsorption by RN4-F

The thermodynamic study of dye adsorption was carried out by taking 5 mg of RN4-F in a 15 mL vial containing 5 mL of rhodamine B dye stock solutions (0.2 to 1 mM dye concentration), and the mixture was stirred for 1 h to reach equilibrium. The suspension was then filtered, and the concentration of the filtrate was determined by UV/Vis spectrometry. The results of thermodynamic studies of dye adsorption by RN4-F were fitted well with the Langmuir model.[35] The adsorption capacity (q_{max}) of RN4-F for rhodamine B was found to be 272 mg g^{-1} (Figure S35). The Langmuir adsorption isotherm was obtained using the following equation:

$$\frac{1}{q_e} = \frac{1}{q_{max,e}} + \frac{1}{q_{max,e} K c_e} \qquad (7)$$

where q_e (mg g^{-1}) is the quantity of the dye adsorbed by RN4-F at equilibrium, $q_{max,e}$ (mg g^{-1}) is the maximum capacity of dye adsorption by RN4-F at equilibrium, c_e (mol L^{-1}) is the concentration of the dye at equilibrium, and K is the equilibrium constant for the dye uptake.

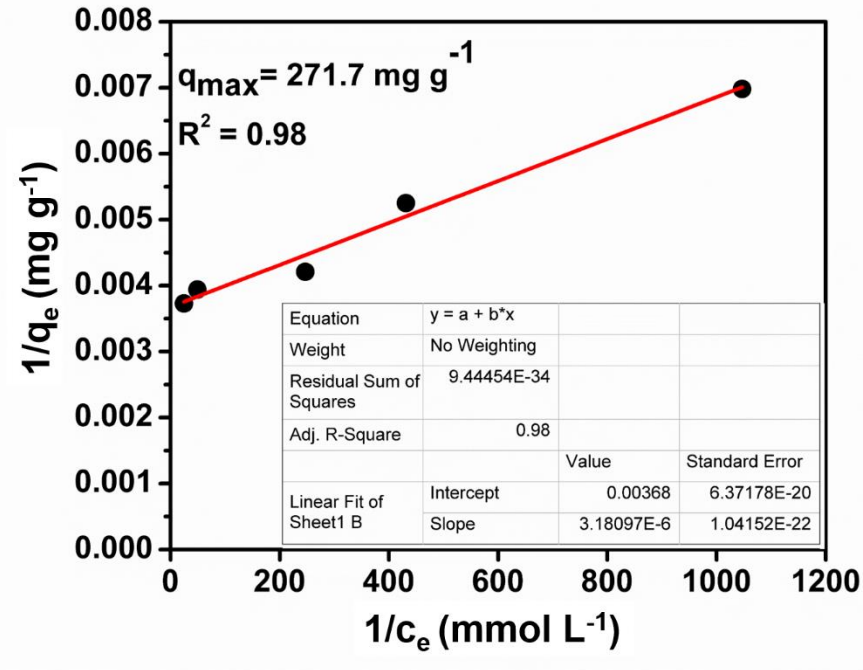

Figure S35. The Langmuir adsorption isotherm of rhodamine B by RN4-F. At high pollutant concentration (up to 1 mM), $q_{max,e}$ was 272 mg g^{-1} as estimated using the Langmuir model.

9.6. Recyclability of dye uptake of RN4-F

10 mg of RN4-F was dispersed in methylene blue stock solution (10 mL, 0.1 mM). The mixture was sonicated for 10 sec for homogenization and stirred at room temperature for 30 min under dark, and then filtered on a Whatman filter paper (Whatman 1). The residual MB concentration in the filtrate was measured by UV/vis spectroscopy. RN4-F was regenerated by washing the POP in ethanol (15 mL) at 50 °C for 6 h and recovered by filtration. The reusability of RN4-F was checked for five cycles with a small decrease in efficiency (98% to 94%, Figure S36), which may be due to the loss of materials during washing. The stability of RN4-F was checked after five-time recycling through FTIR spectroscopy. No significant change in the spectral pattern confirms the stability of the POP (Figure S37).

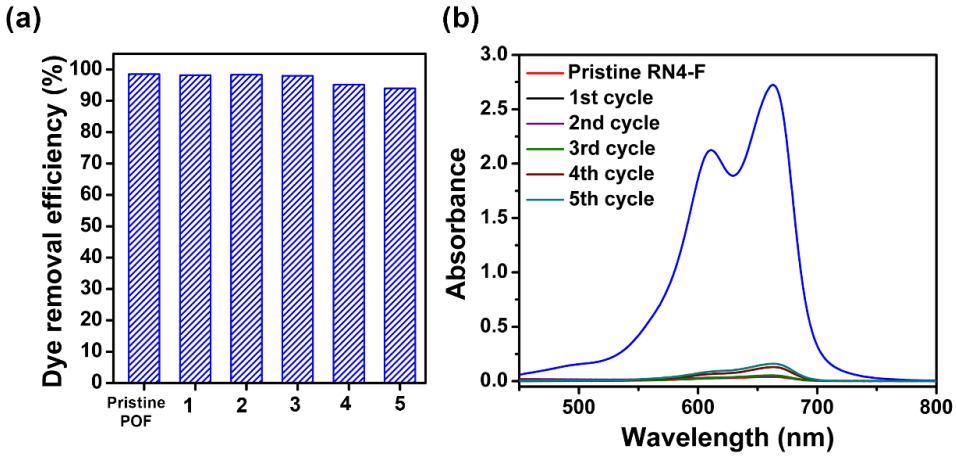

Figure S36. (a) Recyclability of RN4-F up to five cycles; (b) the change in absorbance of methylene blue (MB) solution (0.1 mM) in the presence of RN4-F (1 mg mL^{-1}) for 30 min in different cycles.

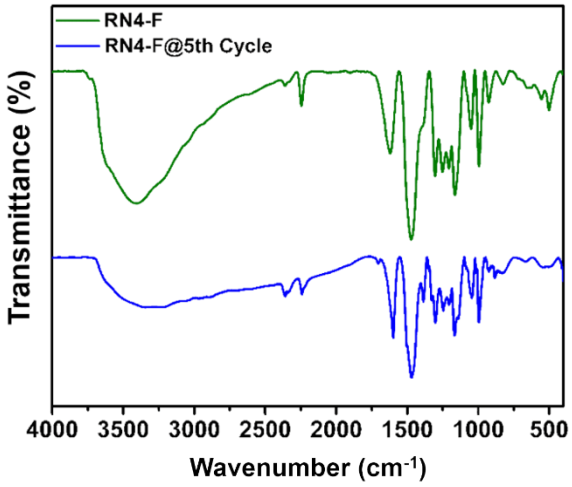

Figure S37. FTIR spectra of pristine and recovered RN4-F after MB adsorption.

Table S5 Comparative accounts of porous organic polymers (POPs) developed in the present study with other porous organic materials, like hypercrosslinked polymers (HCPs), conjugated microporous polymers (CMPs) and covalent organic frameworks (COFs) derived from macrocyclic building blocks for diverse applications.

Adsorbent	Macrocyclic cavitand	S_{BET} ($m^2\ g^{-1}$)	Applications			Reference
			Micropollutant removal	Heterogeneous catalysis	Selective CO_2 uptake, H_2 storage & other	
RN4-F, RN4-OH, RN4-Az-OH	*C*-phenylresorcin [4]arene	1230 724 340	Yes (RN4-F)	Cycloaddition of CO_2 with epoxide (RN4-Az-OH)	Selective CO_2 uptake, H_2 storage (RN4-OH)	*Present work*
P-CDP	*β*-Cyclodextrin	263	Yes	-	-	*Nature* **2016**, *529*, 190[35]
BnCD-HCPP		1225	-	Gold nanoparticle mediated reduction of *p*-nitrophenol	-	*Chem. Sci*. **2016**, *7*, 905[36]
CD-TFP@ cotton		-	Yes	-	-	*Chem. Mater*. **2016**, *28*, 8340[37]
DFB-CDP		140	Yes	-	-	*J. Am. Chem. Soc.* **2017**, *139*, 7689[38]
CD-COF		760	-	-	Li-ion conductivity	*Angew. Chem. Int. Ed.* **2017**, *56*, 16313[39]
β-CD COF		118-263	Yes	-	-	*Chem. Eur. J*. **2018**, *24*, 10979[40]
TFN-CDP-2 to TFN-CDP-5		-	Yes	-	-	*Chem. Sci*. **2018**, *9*, 8883[41]
P5-CMP-1	Pillar[5]arene	400	-	-	Propane/methane separation	*Chem. Mater*. **2016**, *28*, 4460[42]
P-PAP[n]		529, 533	Yes	-	-	*J. Mater. Chem. A* **2017**, *5*, 2514[43]
P[5]-TPE-CMP, P[5]-TET-CMP		7, 22	-	-	Two-photon fluorescence sensors for metal ions and organic molecules	*Adv. Mater*. **2018**, *30*, 1800177[44]
CalP	Calix[4]arene	596	Yes	-	Oil-water separation	*J. Mater. Chem. A* **2017**, *5*, 62[45]
CalP2-Li, CalP3-Li, CalP4-Li		274, 308, 445	-	-	Iodine adsorption from solution/vapor	*Chem. Mater*. **2017**, *29*, 8968[46]
CalP3, CalP4		630, 759	Yes	-	-	*ACS Appl. Mater. Interfaces* **2018**, *10*, 2976[47]
CX4-NS		468	-	-	Iodine vapor adsorption	*ACS Appl. Mater. Interfaces* **2018**, *10*, 17359[48]
$COP1^{++}$, $COP2^{++}$		17.9, 51.8	Yes	-	Iodine capture	*Chem. Eur. J*. **2018**, *24*, 8648[49]

CalPOF-1, CalPOF-2, CalPOF-3	*C*-Alkylcalix[4] resorcinarene	303, 154, 91	-	-	Iodine vapor adsorption	*ACS Sustain. Chem. Eng.* **2018**, *6*, 17402[50]
TPECD, TPESC4A	*β*-Cyclodextrin, sulfonated calix[4]arene	71.9, 91.5	-	-	Tunable photo luminescent in solid state	*Chem. Commun.* **2018**, *54*, 6068[51]
*p*TC-SC4A, *p*TC-P5A	Sulfonated calix[4]arene, pillar[5]arene	123, 85	Yes	-	-	*Chem. Commun.* **2018**, *54*, 7362[52]
P1	*β*-Cyclodextrin, calix[4]arene	8-9	Yes	-	-	*Polym. Chem.* **2014**, *5*, 4499[53]

Table S6 Comparative accounts of *C*-phenylresorcin[4]arene-based porous organic polymers (POPs) with some of the well-known porous materials, like hypercrosslinked polymers (HCPs), conjugated microporous polymers (CMPs), covalent organic frameworks (COFs), metal organic frameworks (MOFs) and porous carbons for H_2 storage (at 77K and 1 bar, > 1 wt%) and selective CO_2 uptake (at 273 K, selectivity > 10).

Absorbent	**S_{BET} (m^2g^{-1})**	**Selective CO_2 uptake over N_2 at 273 K[#]**	**H_2 uptake (wt%, 77 K, 1 bar)**	**Reference**
RN4-OH,	720	20	2	
RN4-Az-OH,	340	19	1.1	*Present work*
RN4-F	1230	35	1.4	
Porous Organic Materials for Selective CO_2 Uptake and H_2 Storage				
PPF-1	1740	14.5	2.7	*Chem. Mater.* **2013**, *25*, 1630[54]
ALP-1	1235	28	2.2	*Chem. Mater.* **2014**, *26*, 1385[55]
PINK	2090	15	2.5	*J. Mater. Chem. A* **2016**, *4*, 2517[56]
CTF-TPC	1668	30	1.7	*J. Mater. Chem. A* **2016**, *4*, 6259[57]
TPMTP	890	61	2.3	*Chem. Commun.* **2017**, *53*, 10576[58]
BDT3	1010	11	2.2	*ACS Appl. Mater. Interfaces* **2016**, *8*, 27669[26]
FCDTPA-K-700	2065	19.6	2.6	*J. Mater. Chem. A* **2014**, *2*, 15139[59]
CPOP-1	2220	25	2.8	*J. Am. Chem. Soc.* **2012**, *134*, 6084[60]
pCTF-1	2034	21.9 wt% (CO_2) (selectivity not shown)	1.7	*Angew. Chem. Int. Ed.* **2018**, *57*, 8438[61]
BILP-7	1122	113	1.3	*Chem. Mater.* **2012**, *24*, 1511[62]
Cz-POF-4	914	37	1.0	*Chem. Mater.* **2014**, *26*, 4023[63]
SPOP-3	965	11.6 wt% (CO_2) (selectivity not shown)	2.2	*Macromolecules* **2011**, *44*, 7987[64]
Metal Organic Frameworks (MOFs) for H_2 Storage				
MOF-177	5640	-	5.5	*J. Am. Chem. Soc.* **2006**, *128*, 3494[65]
$Cu_6(C_s\text{-mdip})_2(C_{2v}\text{-mdip})$	1943	-	3.0	*Angew. Chem. Int. Ed.* **2008**, *47*, 7263[66]
$Be_{12}(OH)_{12}(BTB)_4$	4030	-	1.6	*J. Am. Chem. Soc.* **2009**, *131*, 15120[67]
Zn(tbip)	256	-	0.7	*J. Am. Chem. Soc.* **2006**, *128*, 4180[68]
$Sc(BDC)_3$	721	-	1.5	*Chem. Mater.* **2005**, *17*, 5837[69]
$Co_3(bpdc)_3(4,40\text{-bpy})$	922	-	2.0	*Adv. Mater.* **2005**, *17*, 2703[70]
$Zn_2(BDC)_2(dabco)$	1264	-	1.9	*Adv. Eng. Mater.* **2006**, *8*, 293[71]

Porous Carbon and Composite materials for H_2 and CO_2 storage				
PFA/MOF-5	2827	-	2.6	*J. Am. Chem. Soc.* **2008**, *130*, 5390[72]
SU-MAC-500	941	27	-	*J. Am. Chem. Soc.* **2016**, *138*, 1001[73]

[#]Selectivity was estimated through the ideal adsorption solution theory (IAST).

Table S7 Comparative accounts of *C*-phenylresorcin[4]arene-based porous organic polymers (POPs) with some of the well-known porous materials, like hypercrosslinked polymers (HCPs), conjugated microporous polymers (CMPs), covalent organic frameworks (COFs), ionic liquids (ILs) and metal organic frameworks (MOFs) for cycloaddition of epoxide with carbon dioxide.

Catalyst	Metal used	S_{BET} (m^2g^{-1})	Reaction Condition						% Con.	Reference
			Substrate	Pressure	Temp. (°C)	Catalyst (mg)	TBAB (mmol)	Time (h)		
Porous Organic Materials										
RN4-Az-OH	No	340	Styrene oxide (10 mmol)	2.5 bar	90 °C	30 mg (RN4-Az-OH: 0.2 mol%)[#]	(0.25 mmol)	12	95	*This work*
Zn/RN4-Az-OH	Zn	198						6	98	
RN4-Az-OH	No	340	Styrene oxide (20 mmol)			30 mg (RN4-Az-OH: 0.1 mol%)[#]	(0.12 mmol)	12	77	
Zn/RN4-Az-OH	Zn	198						6	86	
RN4-Az-OH	No	340	Epichlorohydrin (2.5 mmol)	1 atm	35 °C	30 mg (RN4-Az-OH: 0.7 mol%)[#]	(0.5 mmol)	24	84	
Zn/RN4-Az-OH	Zn	198							92	
PPS⊂COF-TpBpy-Cu	Cu	496	Epichlorohydrin (10.9 mmol)	1 bar	40 °C	25 mg	-	24	95	*J. Am. Chem. Soc.* **2016**, *138*, 15790[74]
Zn-HAzo-POP-1	*Zn*	256.5	Propylene oxide (20 mmol)	30 bar	100 °C	18 mg	7.2 mol%	0.8	90	*Angew. Chem. Int. Ed.* **2016**, *55*, 9685[13]
Co/Zn R@HMTA	Co/Zn	442	Propylene oxide (20 mmol)	10 bar	100 °C	30 mg	7.2 mol%	1.5	99	*Adv. Mater.* **2017**, *29*, 1700445[75]
Co-CMP	Co	965	Propylene oxide (25 mmol)	30 bar	100 °C	100 mg	1.8 mol%	1	98	*Nat. Commun.* **2013**, *4*, 1960[76]
PPh3-ILBr-ZnBr2@POPs	Zn	482	Styrene oxide (56 mmol)	30 bar	40 °C	16.3 mg	-	48	20	*ACS Catal.* **2016**, *6*, 6091[77]
Bp-Zn@MA	Zn	445	Styrene oxide (6.72 mmol)	10 bar	100 °C	20 mg	0.55 mol%	1.5	88	*Green Chem.* **2016**, *18*, 6493[78]
cCTF-500	NO	1247	Styrene oxide	10 bar	90 °C	4 wt%	-	12	36	*ACS Appl. Mater. Interfaces* **2017**, *9*, 7209[79]
PAD-3	NO	156	Styrene oxide (5 mmol)	10 bar	110 °C	100 mg	-	0.5	93	*ACS Appl. Mater.*

										Interfaces **2016**, *8*, 12812[80]
ZnTPy/CNTs-3	Zn	122	Styrene oxide (6.6 mmol)	15 bar	120 °C	-	-	2.5	96	*ACS Appl. Mater. Interfaces* **2018**, *10*, 2546[81]
1-Cr, 1-Co (POPs)	Cr/Co	732	Propylene oxide (50 mmol)	20 bar	100 °C	100 mg	0.4 mmol	16	98	*J. Mater. Chem. A* **2016**, *4*, 7453[82]
HCP (PPh_3)	NO	770	Styrene oxide 1.43 mmol	10 bar	130 °C	0.5 mol%	-	4	96	*Chem. Commun.* **2015**, *51*, 15708[83]
PRP-1	NO	835	Styrene oxide (1 mmol)	1 bar	60 °C	50 mg	0.17 mmol	24	92	*Chem. Commun.* **2016**, *52*, 12294[84]
Polymeric catalyst 1	NO	18	Styrene oxide (5 mmol)	1 bar	100 °C	30 mg	-	24	99	*ACS Appl. Mater. Interfaces* **2018**, *10*, 9478[85]
TBICOF	NO	1424	Styrene oxide (1.5 mmol)	1 atm	28 °C	0.1 mol%	0.5 mmol	24	54	*Chem. Mater.* **2019**, *31*, 1584[86]
Ionic Liquids										
PDMBr (ionic liquid)	NO	205	Styrene oxide (10 mmol)	10 bar	110 °C	50 mg	-	4	99	*Chem. Sci.* **2015**, *6*, 6916[87]
CABFILs (ionic liquid)	NO	-	Styrene oxide (14.3 mmol)	20 bar	130 °C	1 mol%	-	0.3	85	*ACS Sustain. Chem. Eng.* **2017**, *5*, 3081[88]
Metal Organic Frameworks and Cages										
gea-MOF-1	Y	1490	Styrene oxide (100 mmol)	20 bar	120 °C	60 mg	0.15 mmol	6	85	*Nat. Chem.* **2014**, *6*, 673[89]
Ni-MON	Ni	-	Styrene oxide (20 mmol)	10 bar	100 °C	10 μmol	0.3 mmol	12	99	*J. Am. Chem. Soc.* **2015**, *137*, 15066[90]
VPI-100 (Ni)	Ni	344	Epichlorohydrin (31.3 mmol)	9.86 bar	90 °C	0.008 mmol	0.31 mmol	6	98	*J. Am. Chem. Soc.* **2018**, *140*, 993[91]
Hf-MOF	Hf	1780	Styrene oxide (0.2 mmol)	1 bar	25 °C	4.0 mol	10 mmol	56	100	*J. Am. Chem. Soc.* **2014**, *136*, 15861[92]
Ti-PCP	Ti	1029	Styrene oxide (10 mmol)	1atm	100 °C	0.9 wt%	0.1 mmol	24	99	*J. Mater. Chem. A* **2017**, *5*, 9163[93]
Cu_2-MOF-1	Cu	2436	Propylene oxide (20 mmol)	1 atm	25 °C	0.2 mol%	10 mol%	48	96	*J. Am. Chem. Soc.* **2016**, *138*, 2142[94]
NU-1008	Zr	1400	Styrene oxide (0.2 mmol) in acetonitrile 400 μL	1 bar	25 °C	4.0 mol%	0.02 mmol	24	100	*Chem. Sci.* **2019**, *10*, 1186.[95]

Co(III)@cage, Al(III)@cage	Co, Al	771	Styrene oxide (5 mmol)	1 atm	25 °C	0.5 mol%	10 mol%	24 h (Co), 48h (Al)	>99	*Chem. Sci.* **2019**, *10*, 1549[96]

[#]The mol% of the catalyst (RN4-Az-OH) was calculated by considering the molecular weight of the repeating unit (A_4-B_2 type polymerization).

Table S8 Comparative accounts of *C*-phenylresorcin[4]arene-based porous organic polymers (POPs) with some of the well-known porous materials, like hypercrosslinked polymers (HCPs), conjugated microporous polymers (CMPs), covalent organic frameworks (COFs) for selective separation of organic micropollutants.

Adsorbent	Size selectivity	Charge specificity	Micropollutants used	q_{max} (mg g^{-1})	References
RN4-F	Yes	Yes (cationic dye)	Methylene blue, cresyl violet, rhodamine B, rhodamine 101, Congo red, methyl blue, methyl orange, rose bengal, *p*-nitrophenol, 2-naphthol	272 (Rhodamine B)	Present study
P-CDP	-	-	Bisphenol A, bisphenol S, 2-naphthol, 2,4-dichlorophenol, 1-naphthyl amine, ethinyl oestradiol, metolachlor, propranolol	81 (Bisphenol A)	*Nature* **2016**, *529*, 190[35]
COP-99	Yes	Yes	Methylene blue, rhodamine B, brilliant blue G, 4-nitrophenol	-	*Nat. Commun.* **2016**, *7*, 13377[10]
SA-COF	Yes	Yes	Anthraflavic acid, methylene blue, rhodamine B, Chrome azurol S	-	*J. Am. Chem. Soc.* **2017**, *139*, 8897[97]
M-TpBD	Yes	-	Rose bengal, tetracycline, methylene blue, Congo red, curcumin, *p*-nitroaniline, methylcobalamine	-	*Adv. Mater.* **2017**, *29*, 1603945[98]
COF-LZU1	Yes	-	Chrome black T. methyl blue, Congo red, acid fuchsin, rose bengal, rhodamine B, methyl orange, methylene blue	-	*Angew. Chem. Int. Ed*. **2018**, *57*, 4083[29]
CalP4	-	-	Bisphenol A, propranolol HCl, 1-naphthylamine, 2-naphthol	403 (Bisphenol A)	*ACS Appl. Mater., Interfaces* **2018**, *10*, 2976[47]
THPS	-	-	Congo red, methylene blue, methyl blue	330 (Methylene blue)	*Macromolecules* **2015**, *48*, 8509[99]
CalP	-	-	Congo red, methylene blue, rhodamine B	625 (Methylene blue)	*J. Mater. Chem. A* **2017**, *5*, 62[45]
AHCP-1	-	-	Methylene blue, rhodamine B, neutral red, methyl orange, bisphenol A, bisphenol S, 4-nitrophenol, hexafluorobisphenol A	258 (Rhodamine B)	*Polym. Chem.* **2018**, *9*, 4724[100]
P-PAP[5]	-	Yes	Paraquat, carbamazepine, tetracycline, bisphenol A, 2,4-dichlorophenol, 1-naphthyl amine, 2-naphthol	209 (Paraquat)	*J. Mater. Chem. A* **2017**, *5*, 2514[43]
TpPa-2–foam	-	-	methylene blue, rhodamine B, acid fuchsin, rose bengal, bisphenol A, decabromodiphenyl ether, $KMnO_4$, I_2	108 (Bisphenol A)	*J. Am. Chem. Soc.* **2019**, *141*, 7572[101]

10. ^{1}H, ^{13}C NMR and MALDI-TOF spectra of compounds

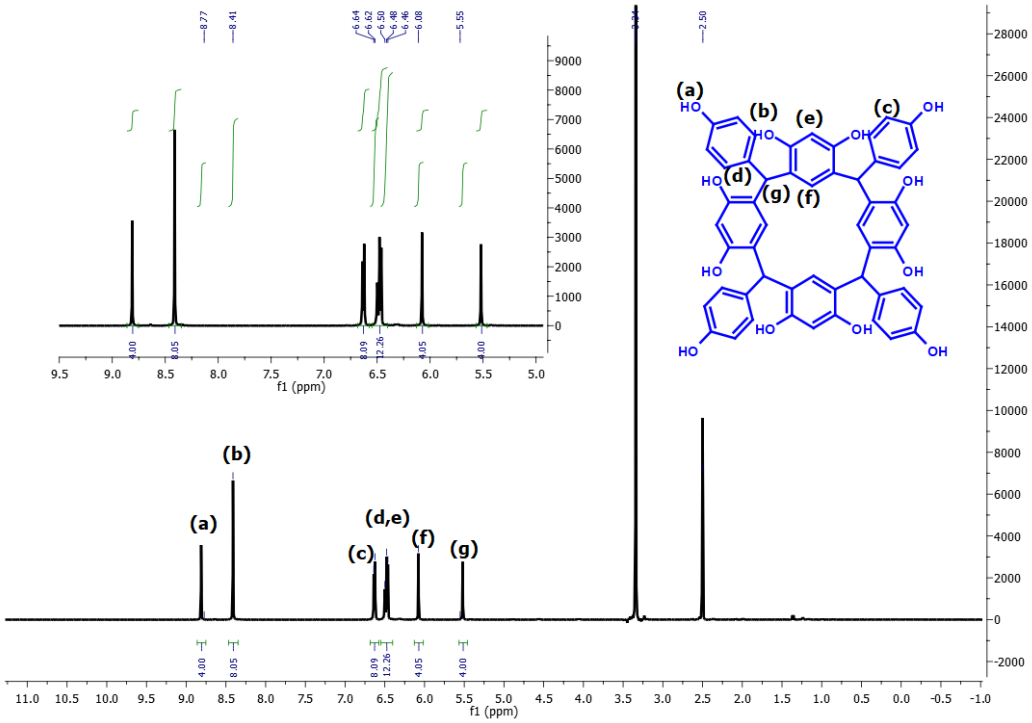

Figure S38. ^{1}H NMR spectrum of *p*-hydroxyphenylresorcin[4]arene.

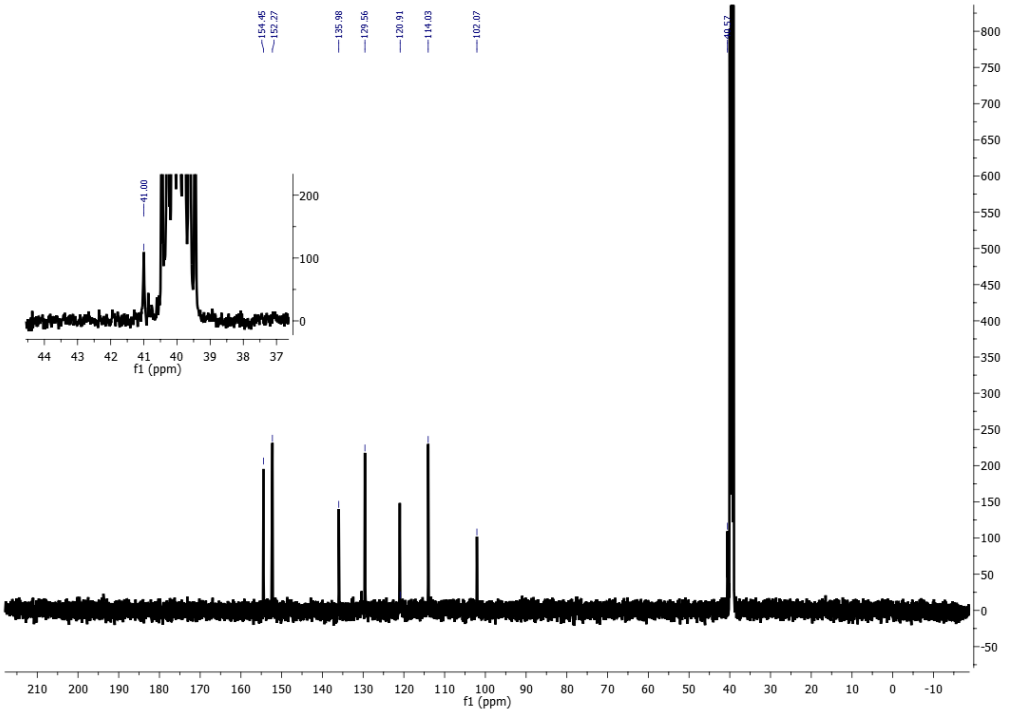

Figure S39. ^{13}C NMR spectrum of *p*-hydroxyphenylresorcin[4]arene.

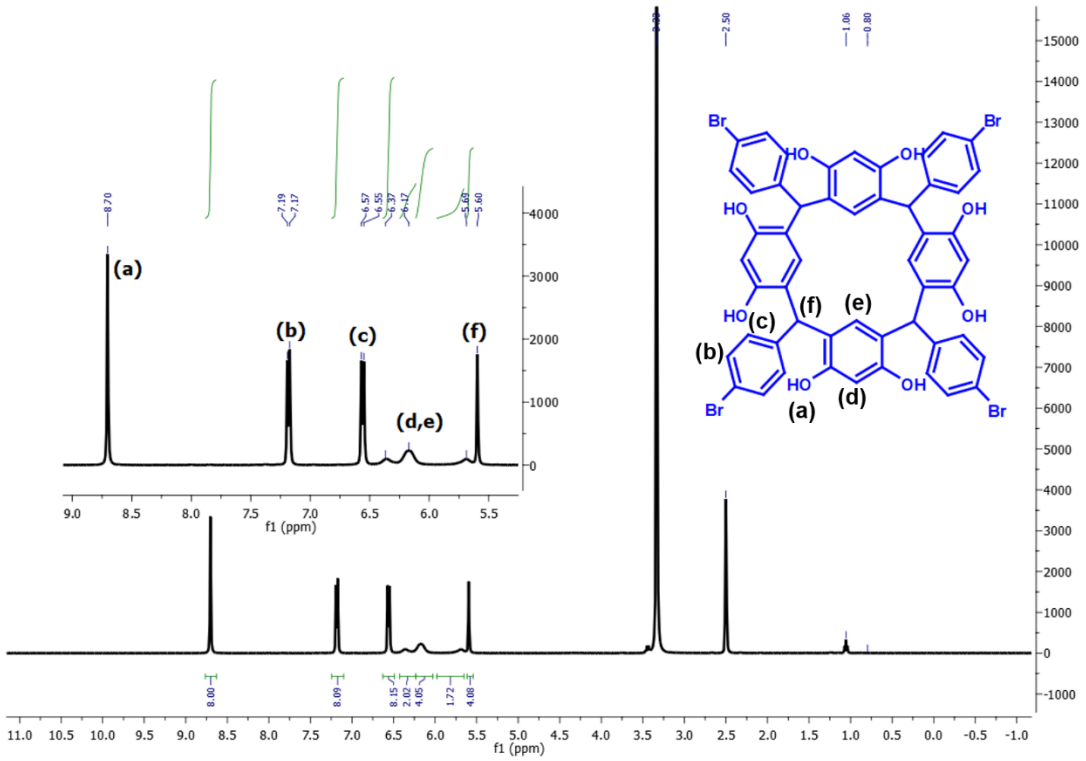

Figure S40. ^{1}H NMR spectrum of *p*-bromophenylresorcin[4]arene.

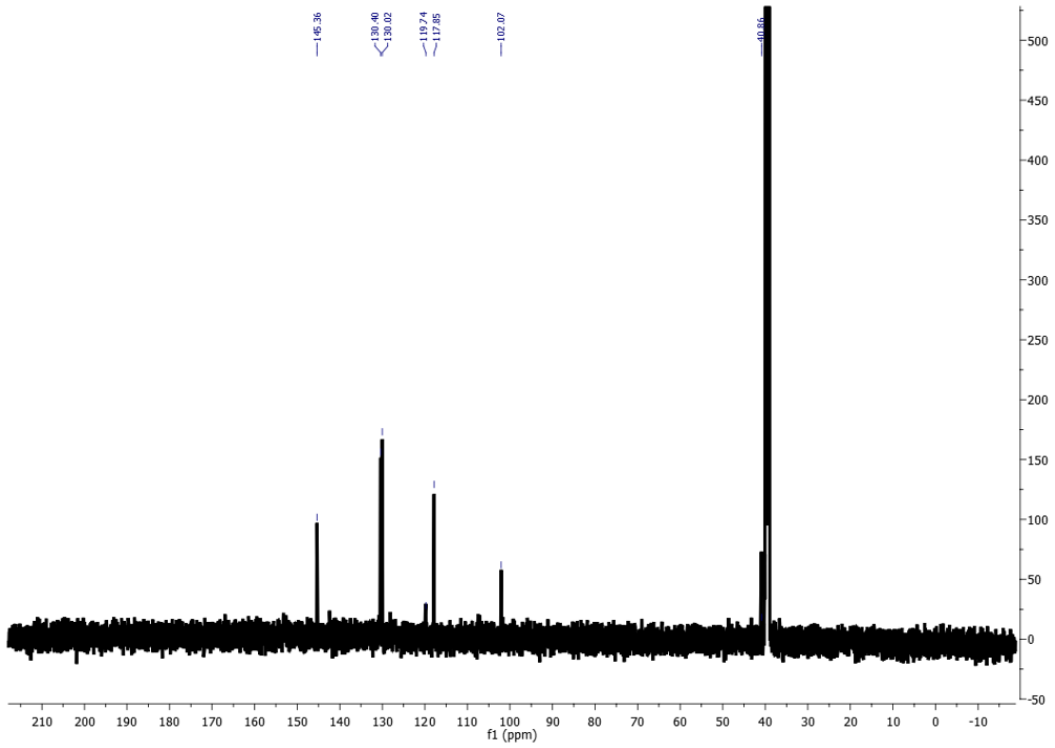

Figure S41. ^{13}C NMR spectrum of *p*-bromophenylresorcin[4]arene.

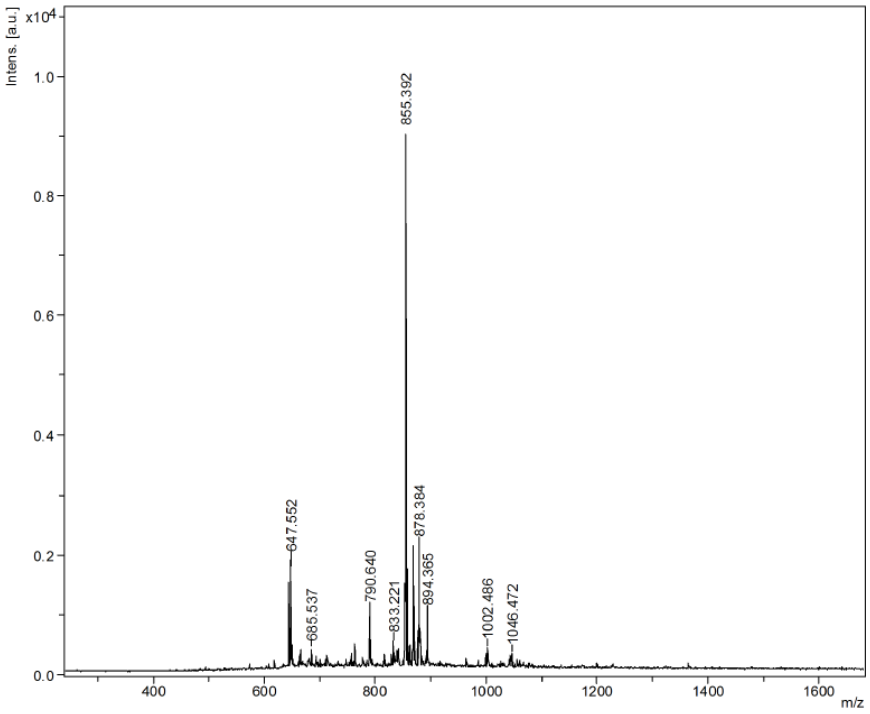

Figure S42. MALDI-TOF analysis of *p*-hydroxyphenylresorcin[4]arene.

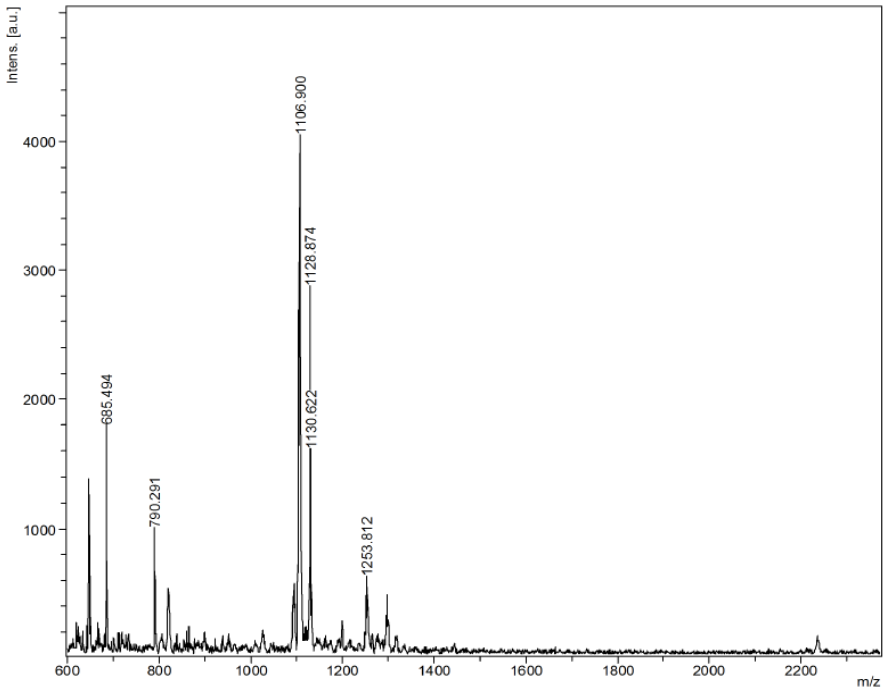

Figure S43. MALDI-TOF analysis of *p*-bromophenylresorcin[4]arene.

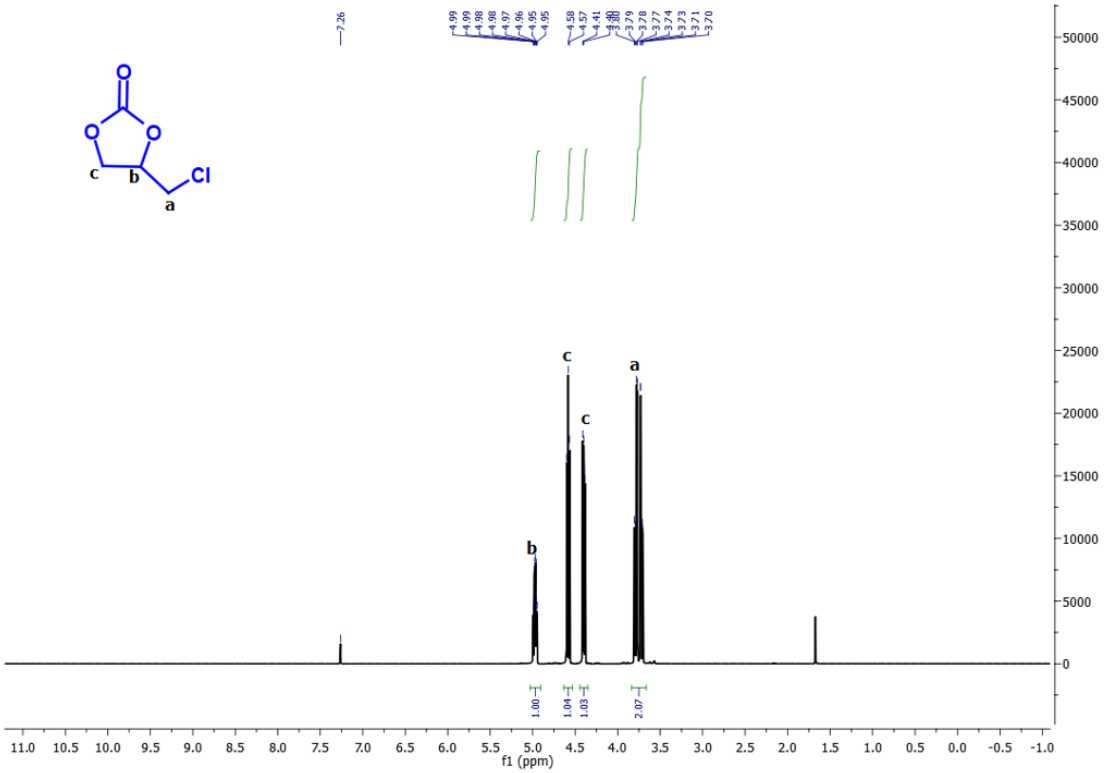

Figure S44. ^{1}H NMR spectrum of 4-(chloromethyl)-1,3-dioxolan-2-one.

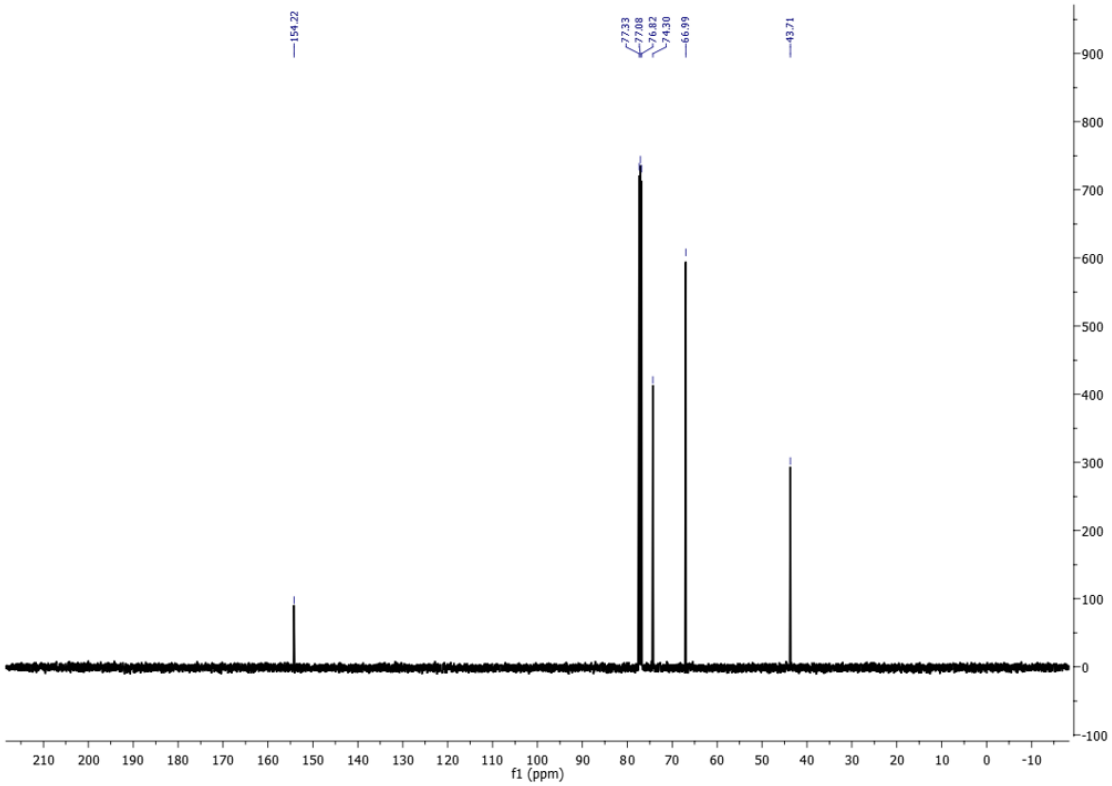

Figure S45. ^{13}C NMR spectrum of 4-(chloromethyl)-1,3-dioxolan-2-one.

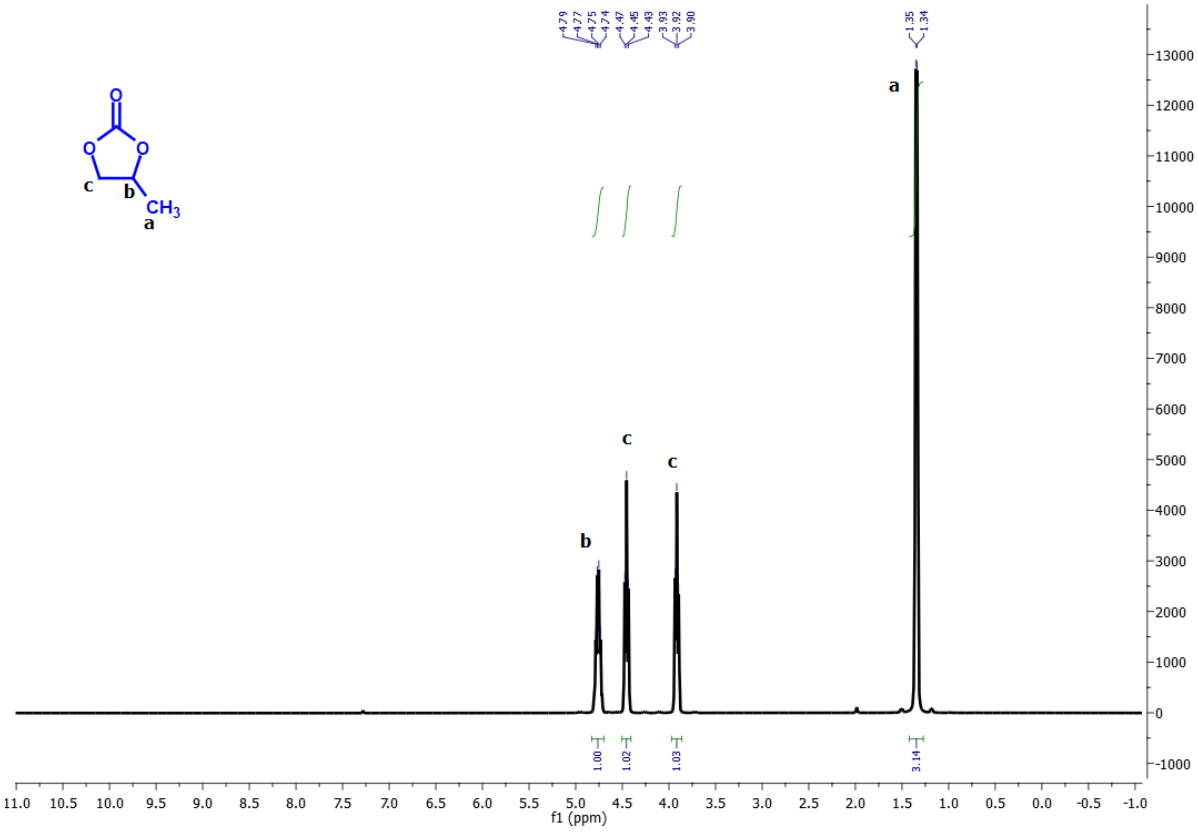

Figure S46. ^{1}H NMR spectrum of 4-methyl-1,3-dioxolan-2-one.

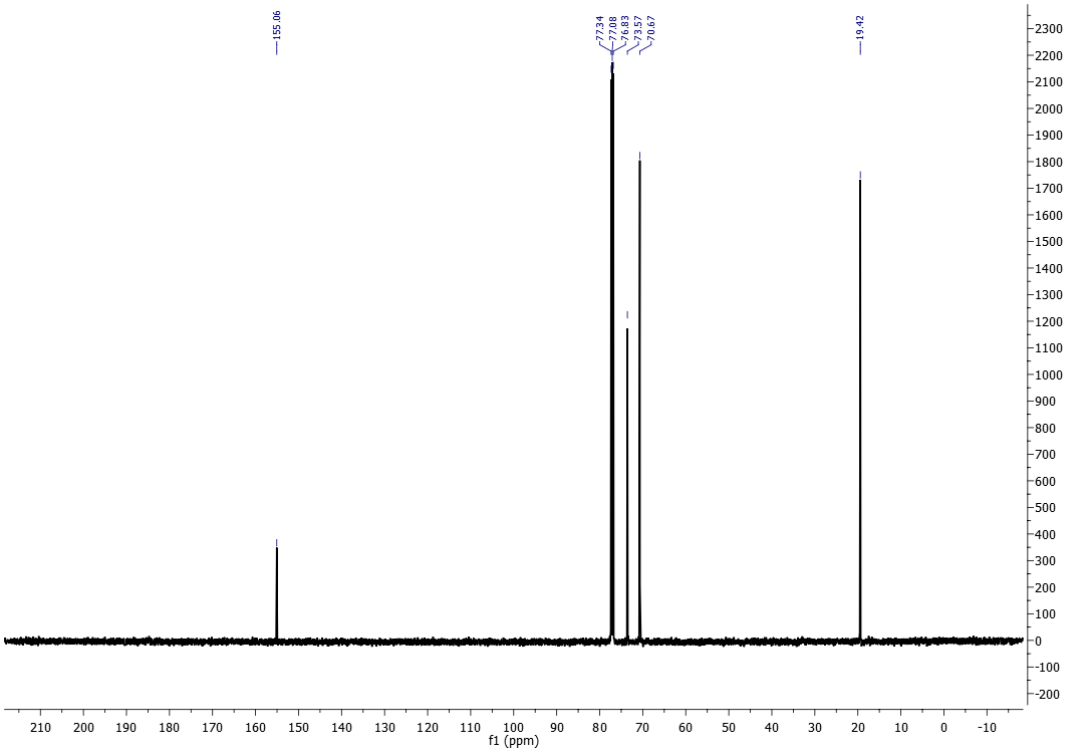

Figure S47. ^{13}C NMR spectrum of 4-methyl-1,3-dioxolan-2-one.

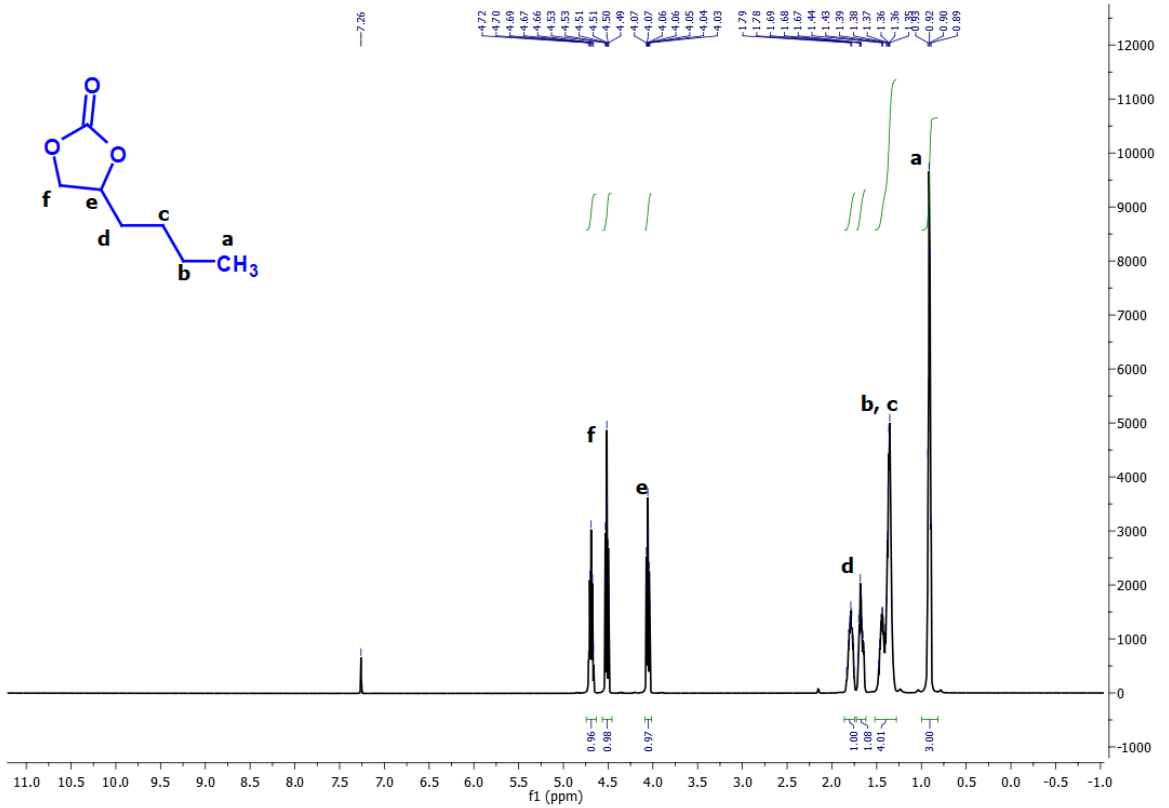

Figure S48. ^{1}H NMR spectrum of 4-butyl-1,3-dioxolan-2-one.

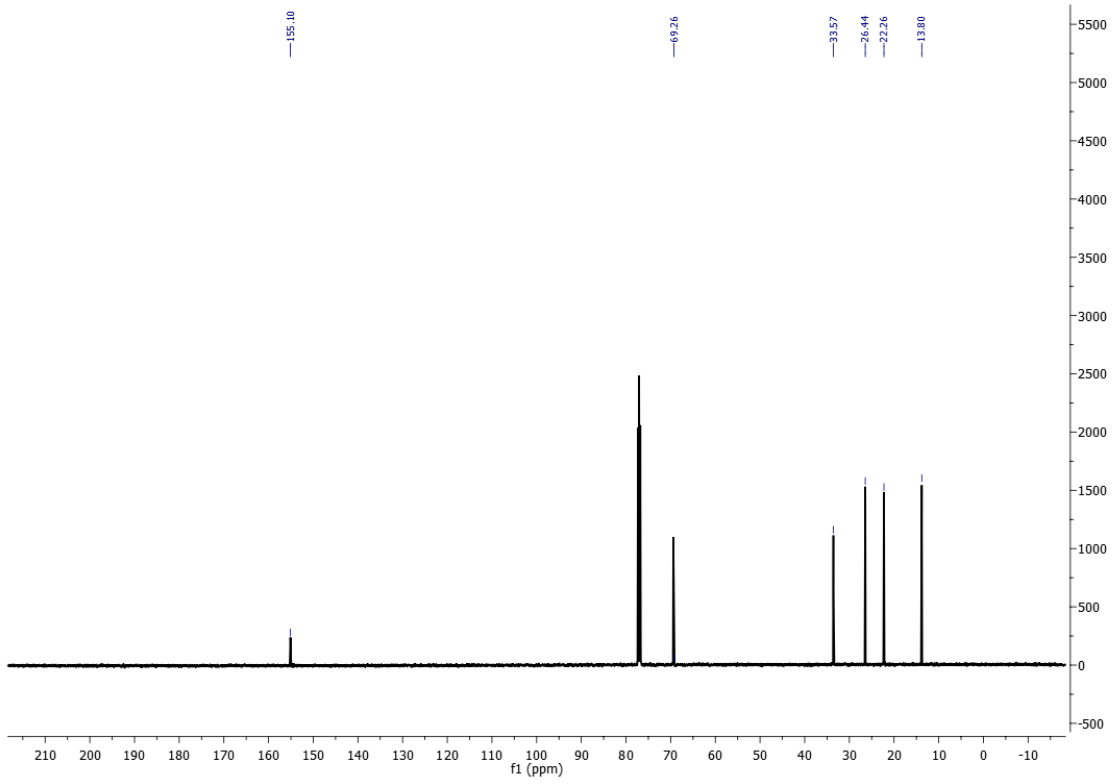

Figure S49. ^{13}C NMR spectrum of 4-butyl-1,3-dioxolan-2-one.

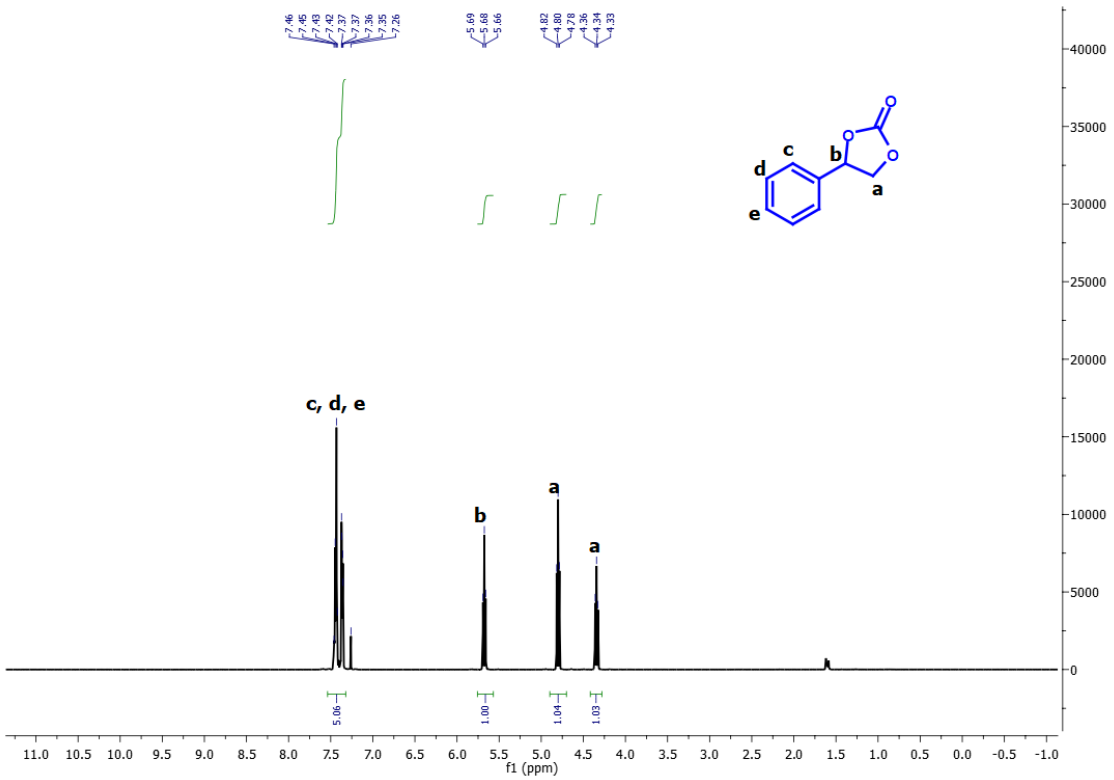

Figure S50. ^{1}H NMR spectrum of 4-phenyl-1,3-dioxolan-2-one.

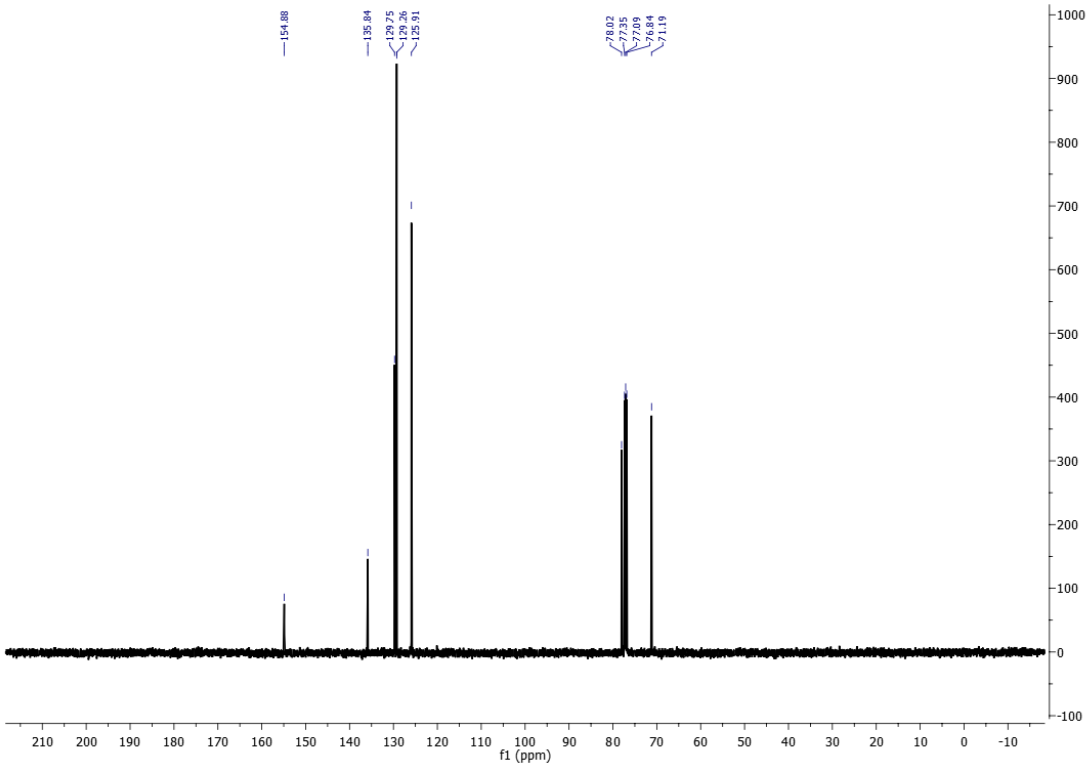

Figure S51. ^{13}C NMR spectrum of 4-phenyl-1,3-dioxolan-2-one.

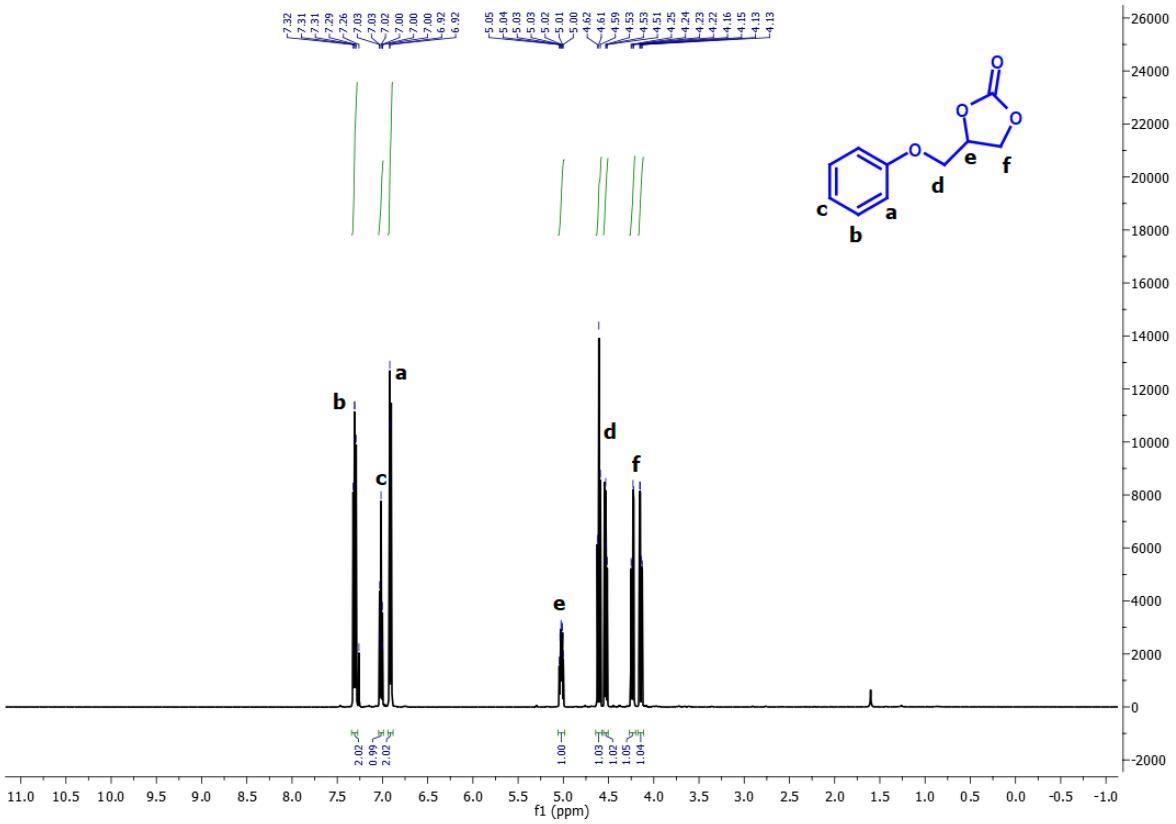

Figure S52. ^{1}H NMR spectrum of 4-(phenoxymethyl)-1,3-dioxolan-2-one.

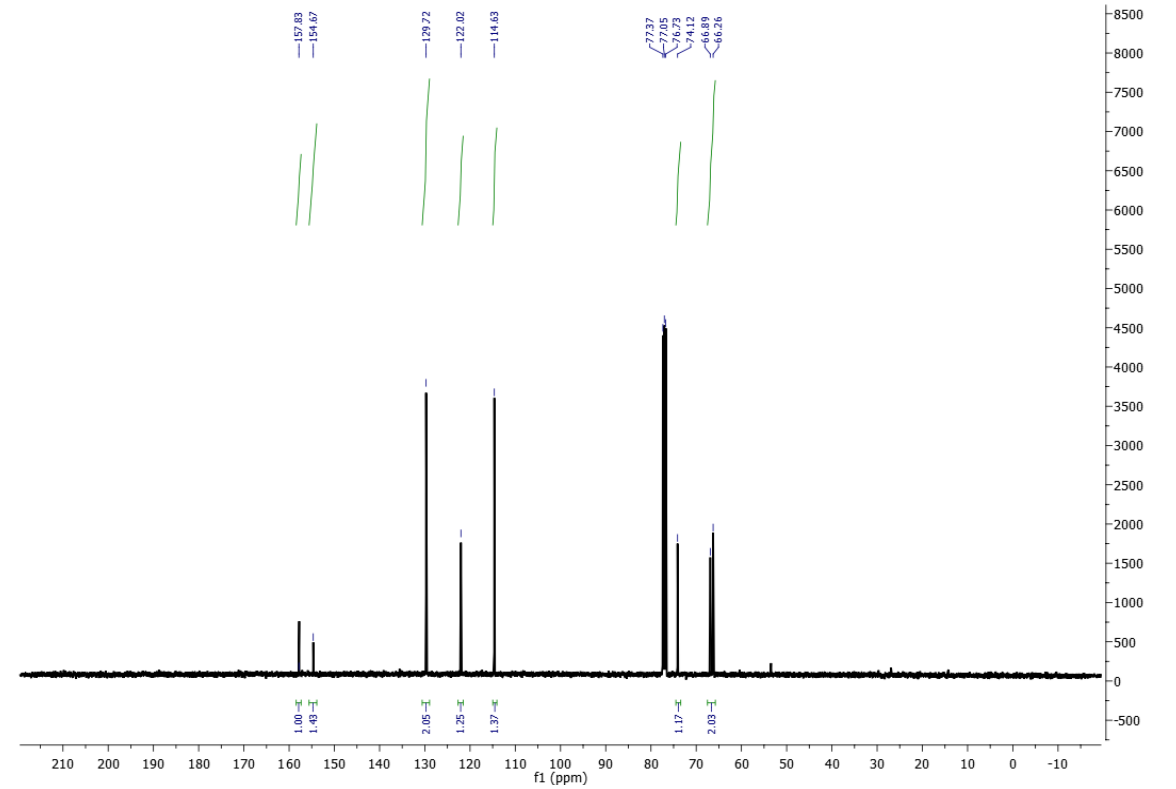

Figure S53. ^{13}C NMR spectrum of 4-(phenoxymethyl)-1,3-dioxolan-2-one.

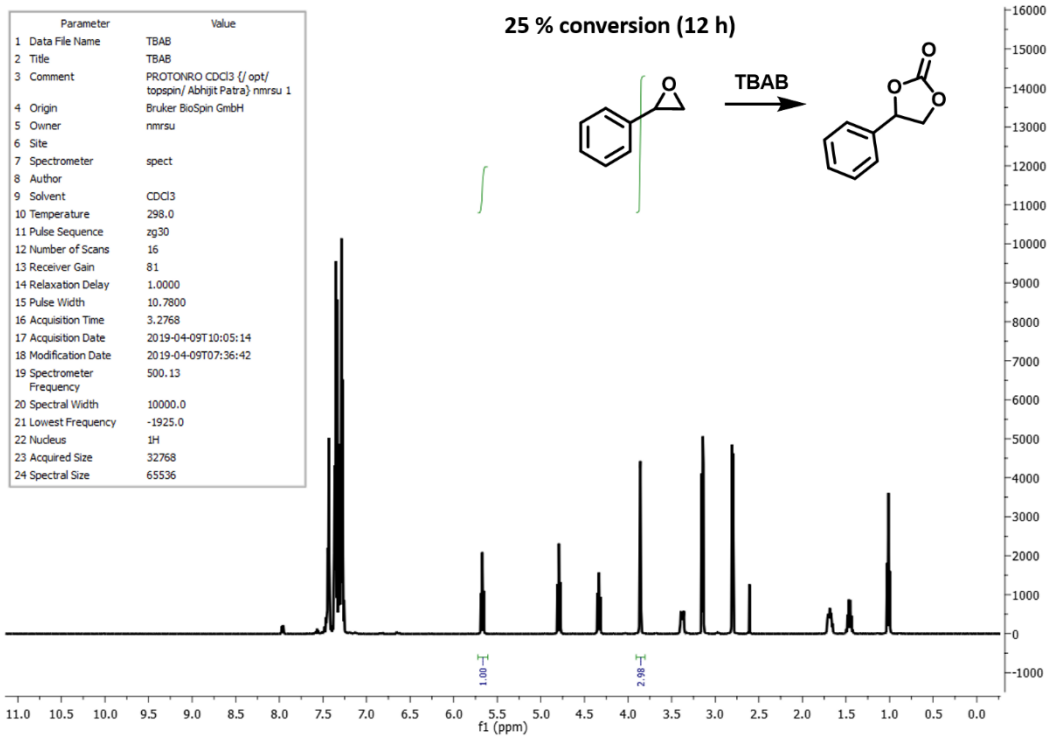

Figure S54. ^{1}H NMR conversion of styrene oxide in presence of TBAB (Conversion: 25%, Table 2, entry 1).

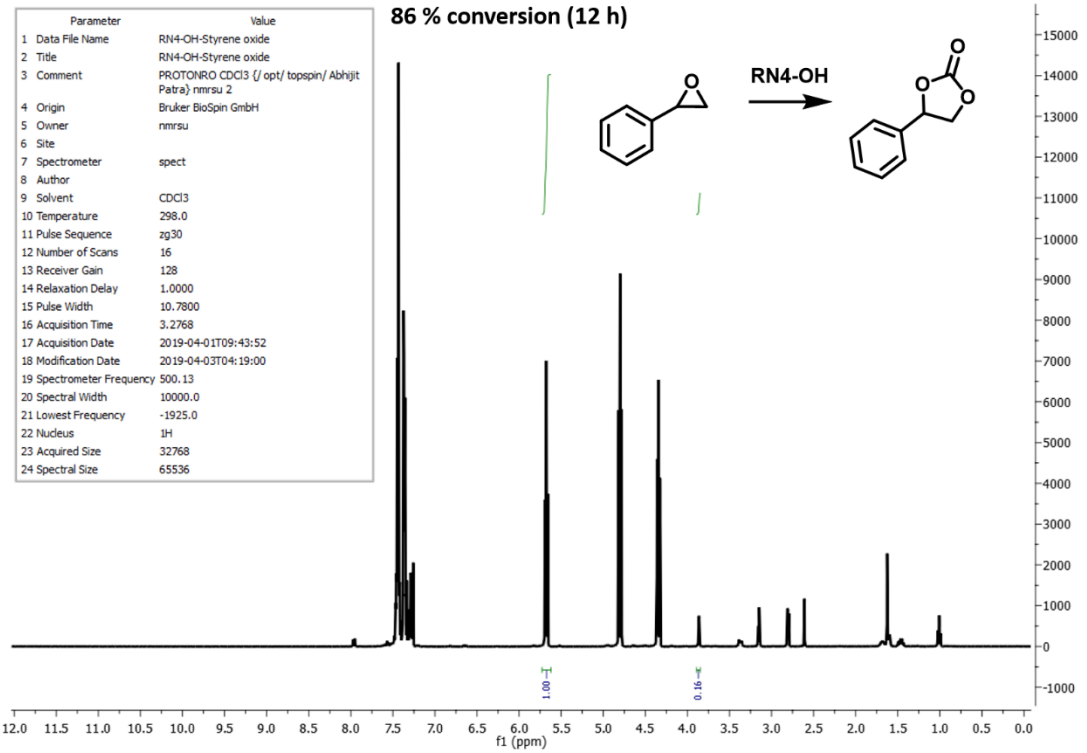

Figure S55. ^{1}H NMR conversion of styrene oxide in presence of RN4-OH (Conversion: 86 %, Table 2, entry 3).

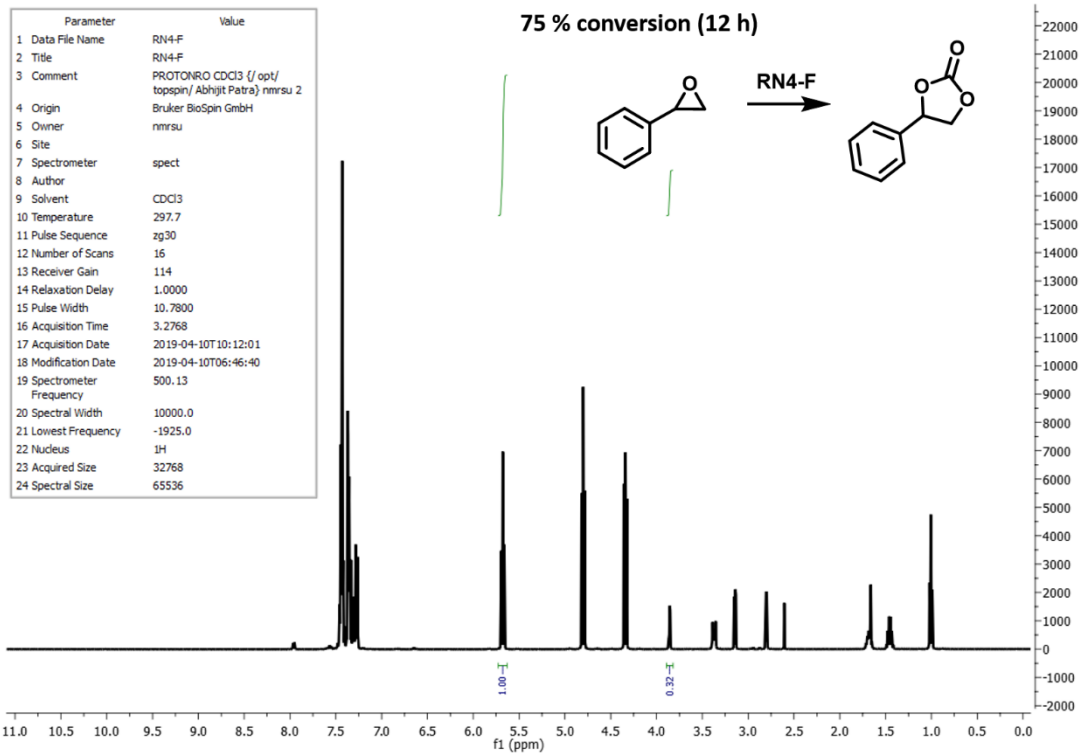

Figure S56. ^{1}H NMR conversion of styrene oxide in presence of RN4-F (Conversion: 75%, Table 2, entry 4).

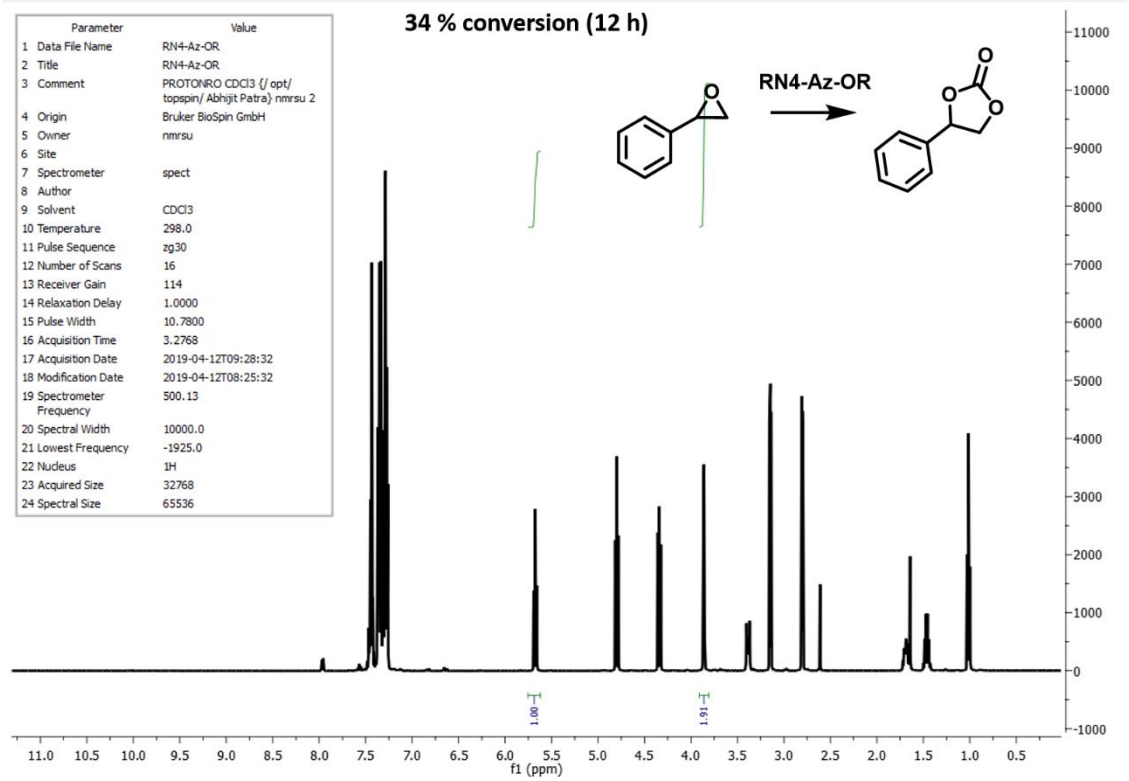

Figure S57. ^{1}H NMR conversion of styrene oxide in presence of RN4-Az-OR (Conversion: 34%, Table 2, entry 5).

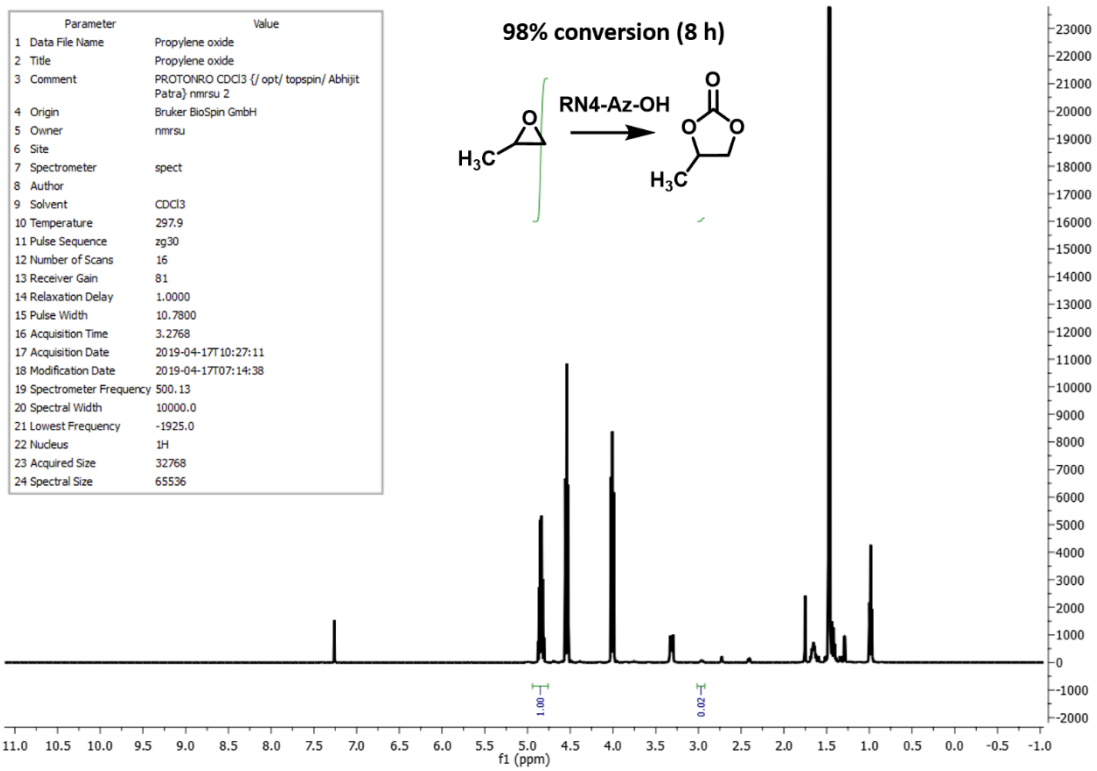

Figure S58. ^{1}H NMR conversion of propylene oxide in presence of RN4-Az-OH (Conversion: 98%, Figure 4a).

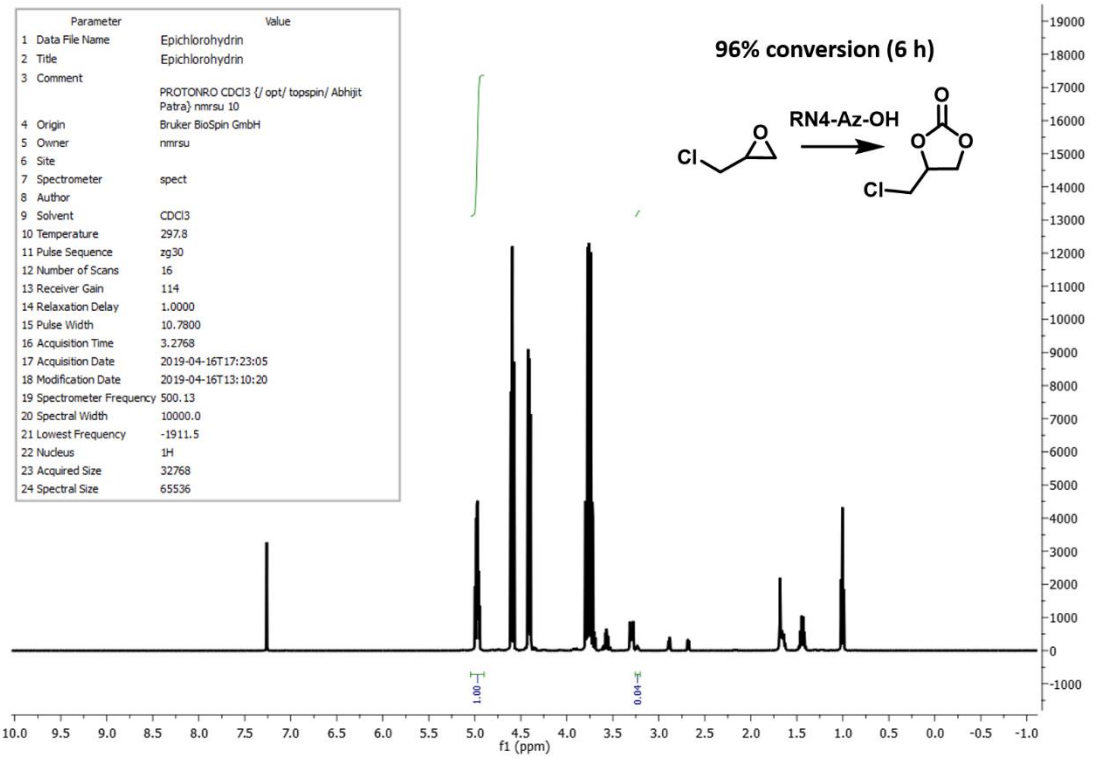

Figure S59. ^{1}H NMR conversion of epichlorohydrin in presence of RN4-Az-OH (Conversion: 96%, Figure 4a).

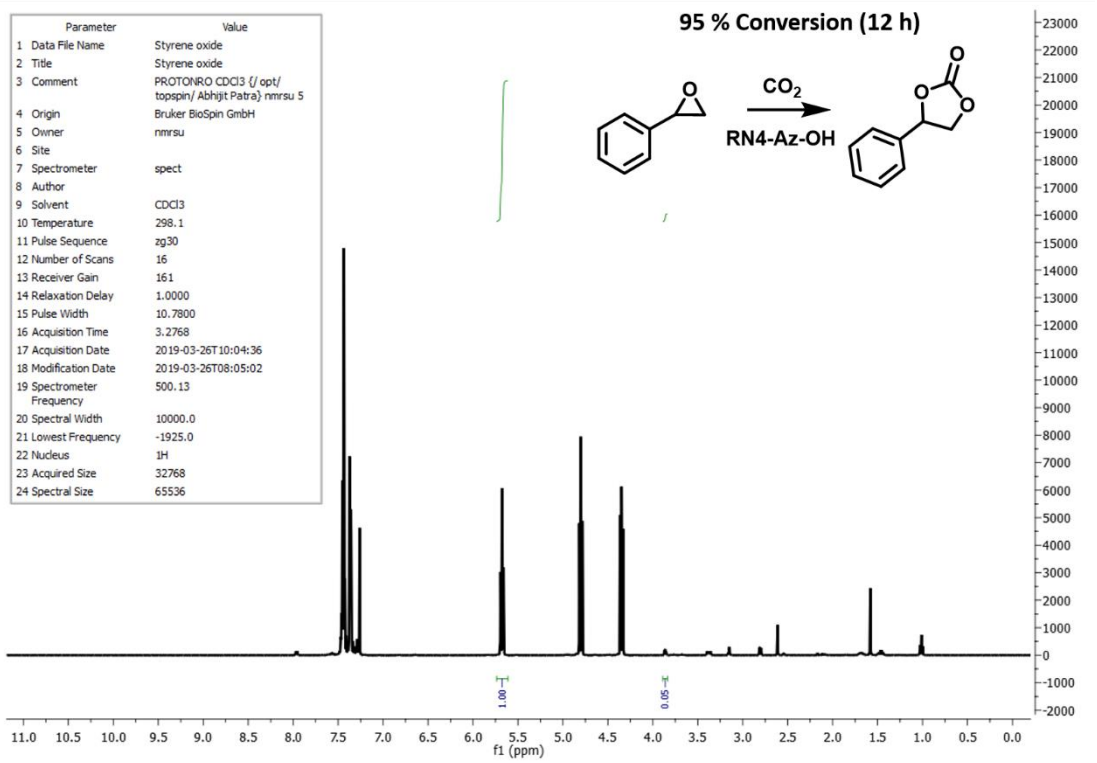

Figure S60. [1]H NMR conversion of styrene oxide in presence of RN4-Az-OH (Conversion: 95%, Table 2, entry 2, Figure 4a).

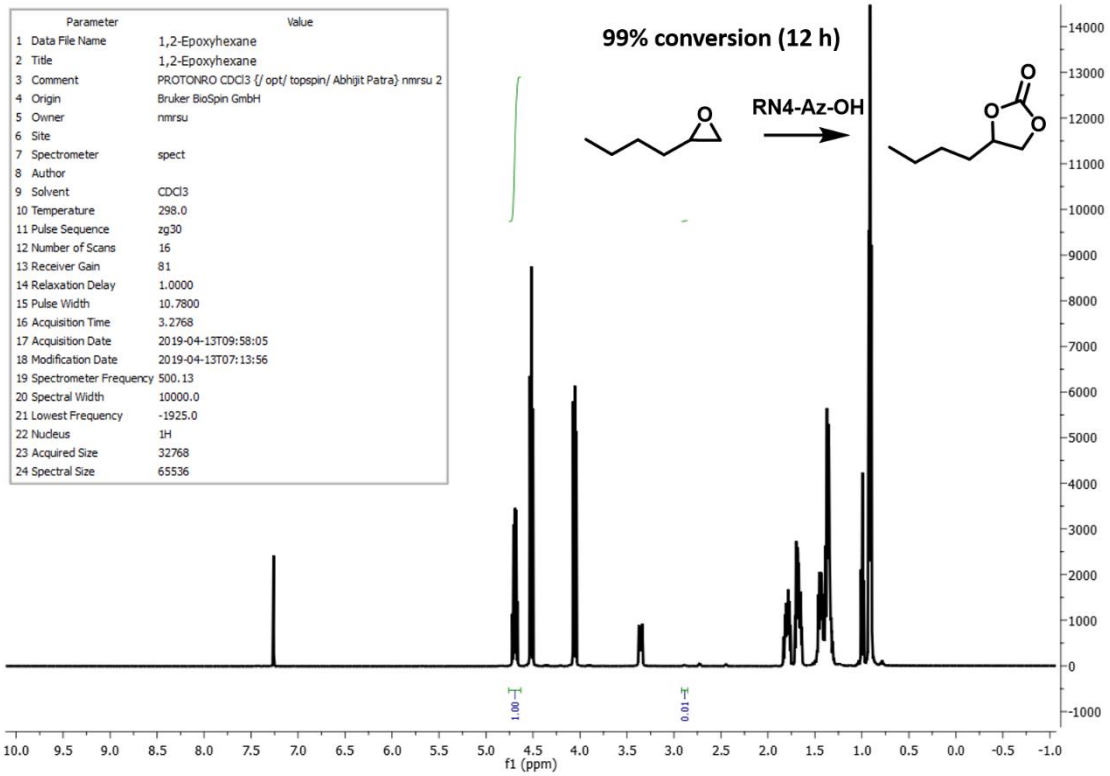

Figure S61. [1]H NMR conversion of epoxyhexane in presence of RN4-Az-OH (Conversion: 99%, Figure 4a).

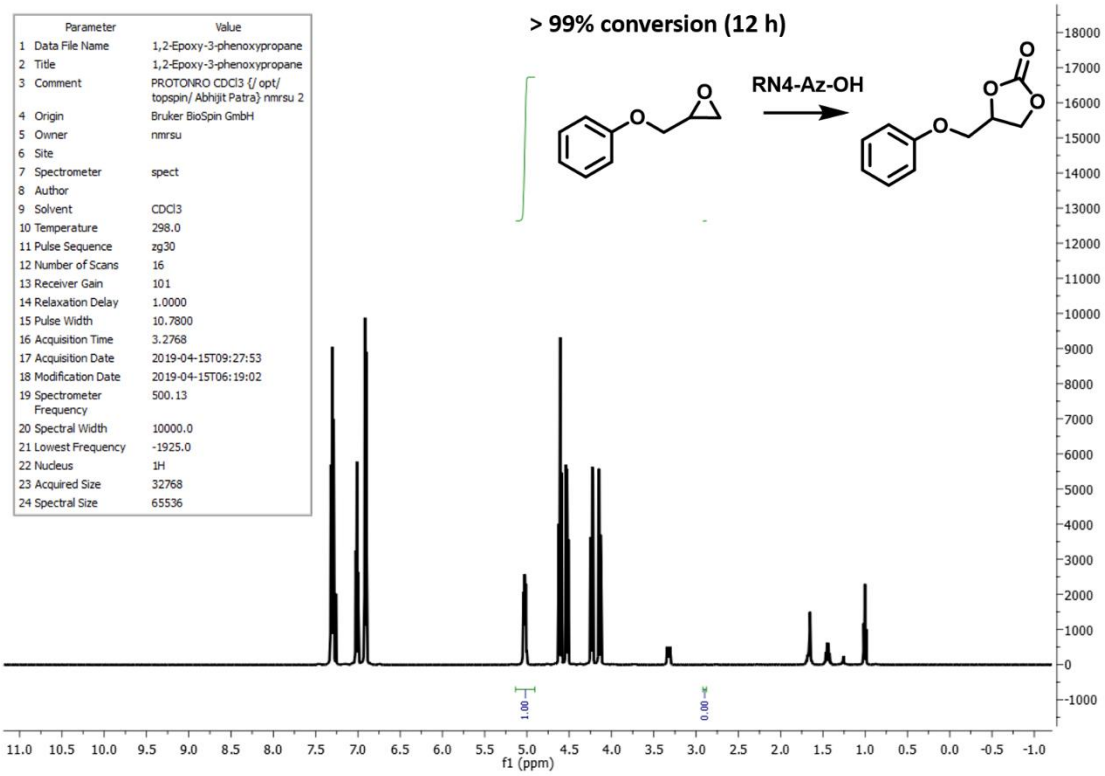

Parameter	Value
1 Data File Name	1,2-Epoxy-3-phenoxypropane
2 Title	1,2-Epoxy-3-phenoxypropane
3 Comment	PROTONRO CDCl3 {/ opt/ topspin/ Abhijit Patra} nmrsu 2
4 Origin	Bruker BioSpin GmbH
5 Owner	nmrsu
6 Site	
7 Spectrometer	spect
8 Author	
9 Solvent	CDCl3
10 Temperature	298.0
11 Pulse Sequence	zg30
12 Number of Scans	16
13 Receiver Gain	101
14 Relaxation Delay	1.0000
15 Pulse Width	10.7800
16 Acquisition Time	3.2768
17 Acquisition Date	2019-04-15T09:27:53
18 Modification Date	2019-04-15T06:19:02
19 Spectrometer Frequency	500.13
20 Spectral Width	10000.0
21 Lowest Frequency	-1925.0
22 Nucleus	1H
23 Acquired Size	32768
24 Spectral Size	65536

Figure S62. [1]H NMR conversion of 1,2-epoxy-3-phenoxypropane in presence of RN4-Az-OH (Conversion: 99%, Figure 4a).

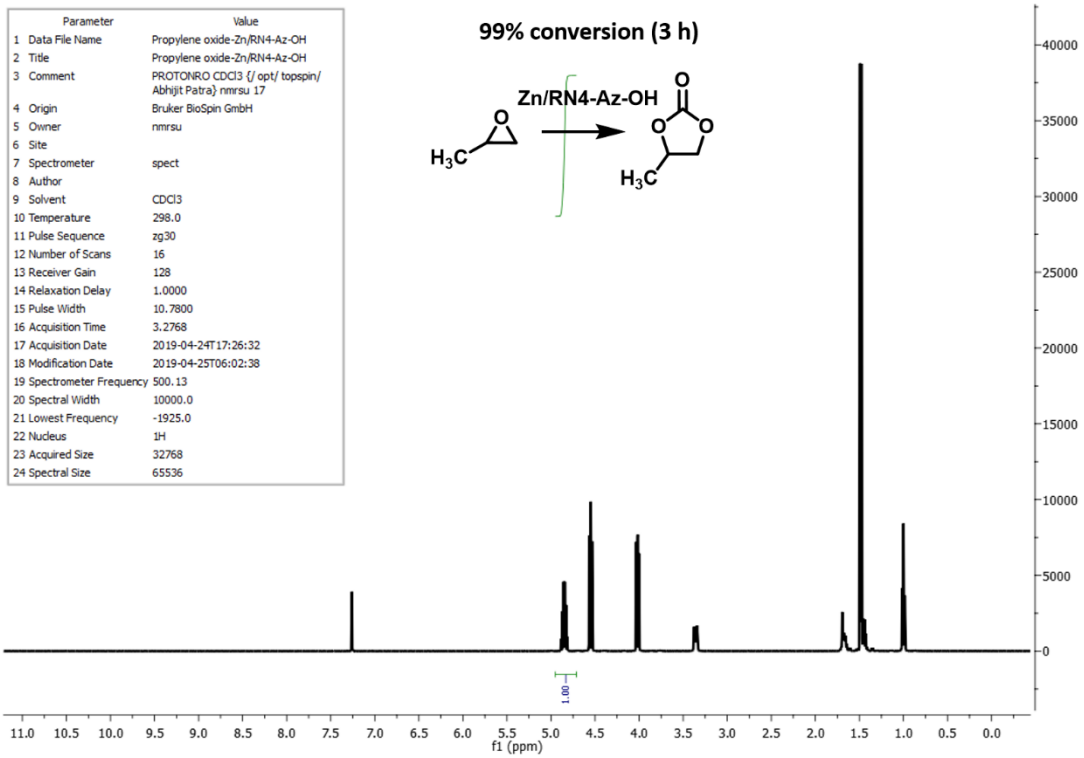

Parameter	Value
1 Data File Name	Propylene oxide-Zn/RN4-Az-OH
2 Title	Propylene oxide-Zn/RN4-Az-OH
3 Comment	PROTONRO CDCl3 {/ opt/ topspin/ Abhijit Patra} nmrsu 17
4 Origin	Bruker BioSpin GmbH
5 Owner	nmrsu
6 Site	
7 Spectrometer	spect
8 Author	
9 Solvent	CDCl3
10 Temperature	298.0
11 Pulse Sequence	zg30
12 Number of Scans	16
13 Receiver Gain	128
14 Relaxation Delay	1.0000
15 Pulse Width	10.7800
16 Acquisition Time	3.2768
17 Acquisition Date	2019-04-24T17:26:32
18 Modification Date	2019-04-25T06:02:38
19 Spectrometer Frequency	500.13
20 Spectral Width	10000.0
21 Lowest Frequency	-1925.0
22 Nucleus	1H
23 Acquired Size	32768
24 Spectral Size	65536

Figure S63. [1]H NMR conversion of propylene oxide in presence of Zn/RN4-Az-OH (Conversion: 99 %, Table S3).

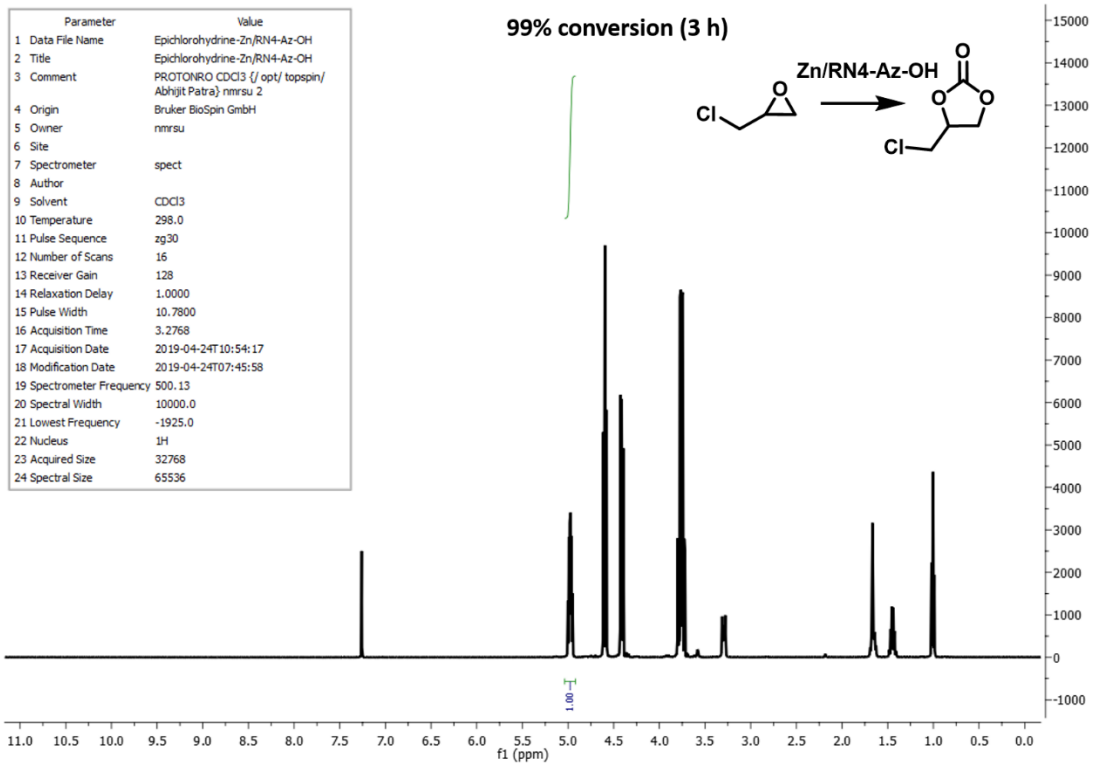

Figure S64. [1]H NMR conversion of epichlorohydrin in presence of Zn/RN4-Az-OH (Conversion: 99 %, Table S3).

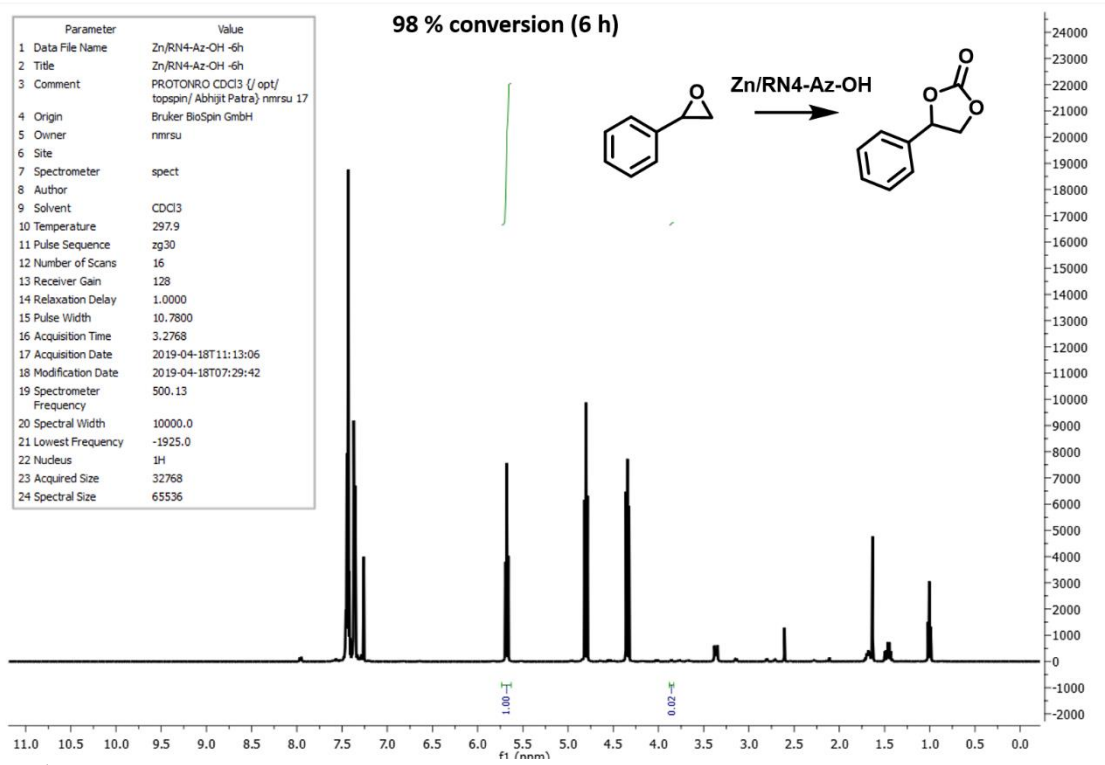

Figure S65. [1]H NMR conversion of styrene oxide in presence of Zn/RN4-Az-OH (Conversion: 98 %, Table S3).

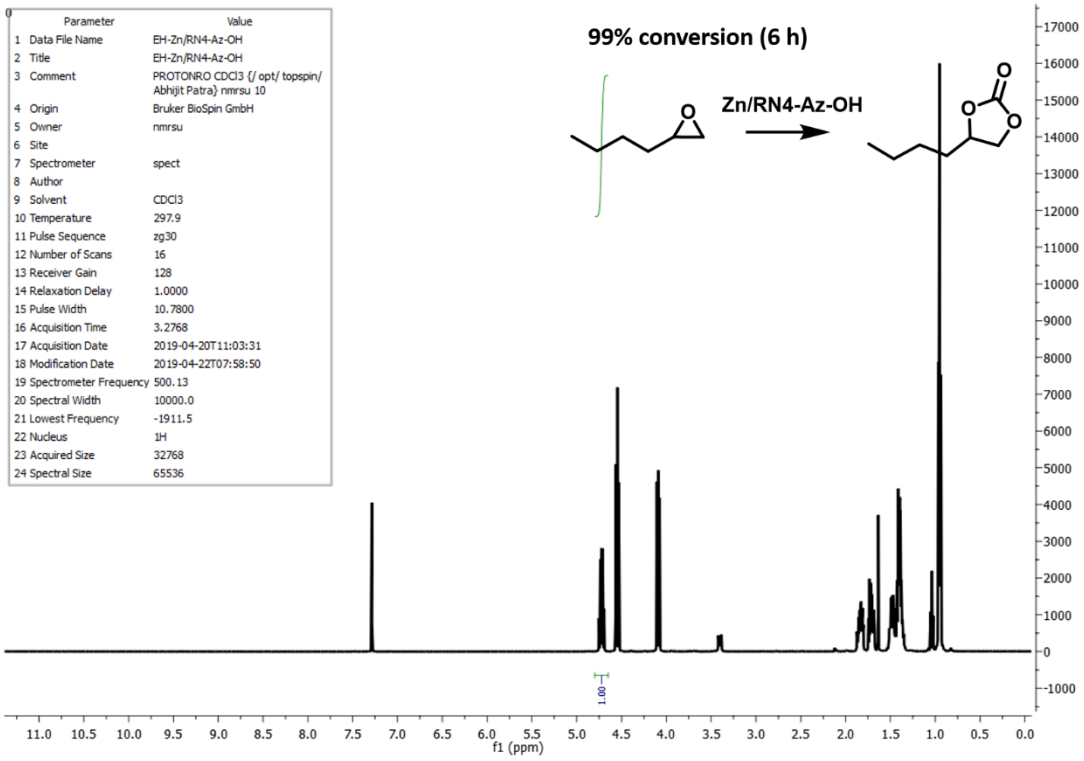

Figure S66. [1]H NMR conversion of epoxyhexane in presence of Zn/RN4-Az-OH (Conversion: 99 %, Table S3).

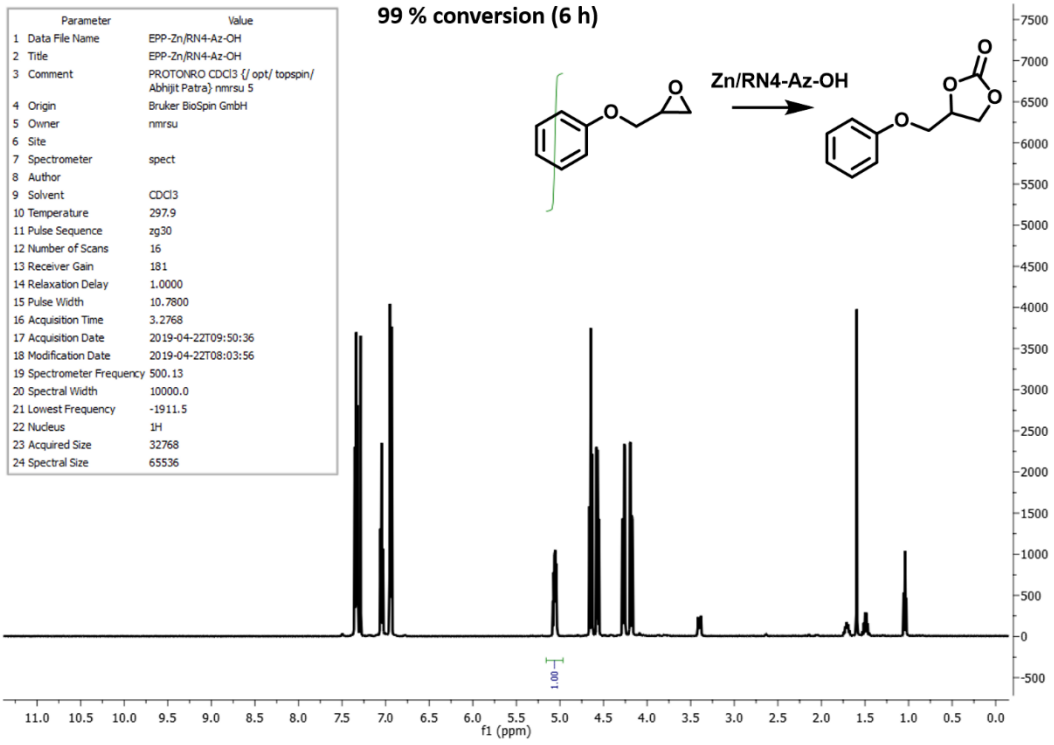

Figure S67. [1]H NMR conversion of 1,2-epoxy-3-phenoxypropane in presence of Zn/RN4-Az-OH (Conversion: 99 %, Table S3).

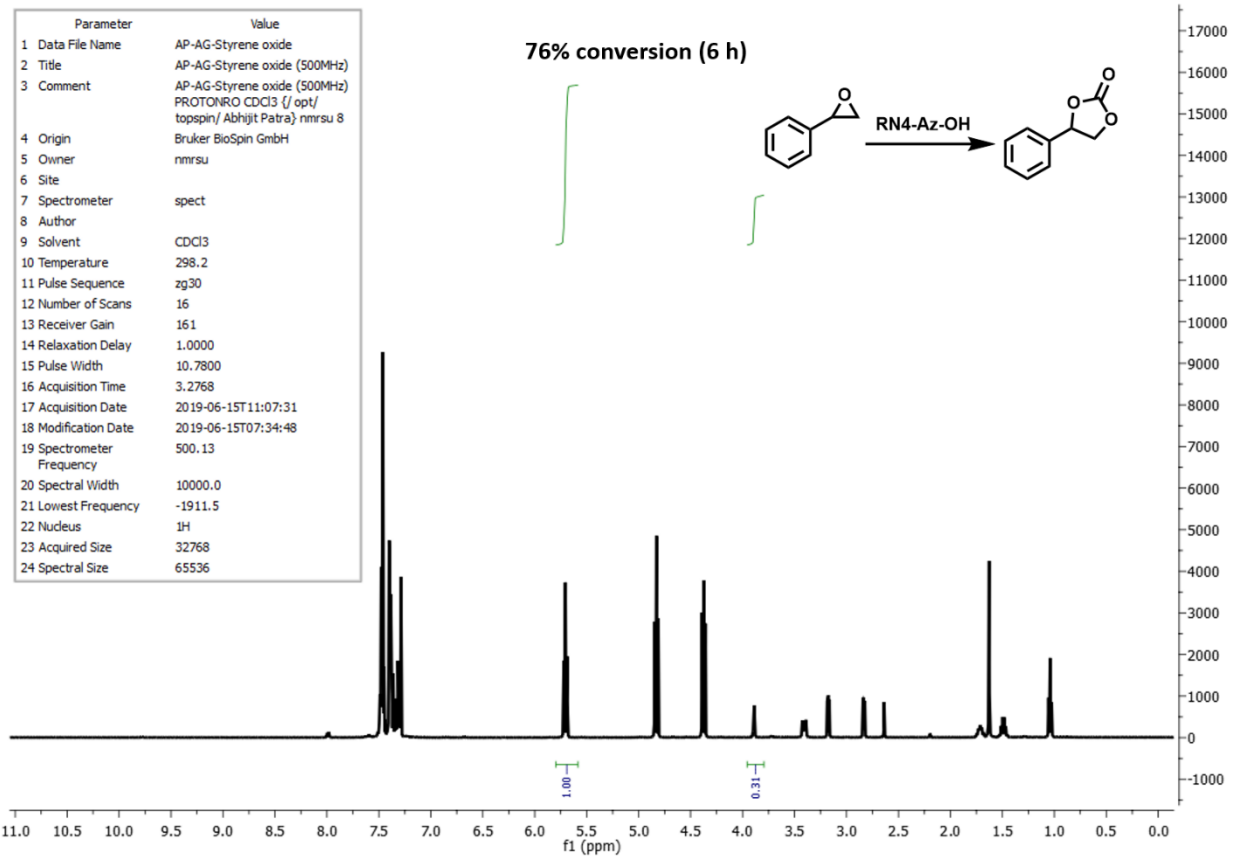

Figure S68. ^{1}H NMR conversion of styrene oxide in presence of RN4-Az-OH (Conversion: 76%) at 6 h.

12. References

(1) Niederl, J. B.; Vogel, H. J. Aldehyde-Resorcinol Condensations. *J. Am. Chem. Soc.* **1940**, *62*, 2512-2514.

(2) Gutsche, C. D. *Calixarenes*; The Royal Society of Chemistry: Cambridge, England, 1989.

(3) Roberts, B. A.; Cave, G. W. V.; Raston, C. L.; Scott, J. L. Solvent-Free Synthesis of Calix[4]resorcinarenes. *Green Chem.* **2001**, *3*, 280-284.

(4) Zhang, Q.; Catti, L.; Tiefenbacher, K. Catalysis inside the Hexameric Resorcinarene Capsule. *Acc. Chem. Res.* **2018**, *51*, 2107-2114.

(5) Li, H.; Yang, Y.; Xu, F. F.; Liang, T. X.; Wen, H. R.; Tian, W. Pillararene-based Supramolecular Polymers. *Chem. Commun.* **2019**, *55*, 271-285.

(6) Thallapally, P. K.; Dobrzanska, L.; Gingrich, T. R.; Wirsig, T. B.; Barbour, L. J.; Atwood, J. L. Acetylene Absorption and Binding in a Nonporous Crystal Lattice. *Angew. Chem. Int. Ed.* **2006**, *45*, 6506-6509.

(7) Lo Meo, P.; Lazzara, G.; Liotta, L.; Riela, S.; Noto, R. Cyclodextrin–Calixarene Co-polymers as a New Class of Nanosponges. *Polym. Chem.* **2014**, *5*, 4499–4510.

(8) Patel, H. A.; Je, S. H.; Park, J.; Chen, D. P.; Jung, Y.; Yavuz, C. T.; Coskun, A. Unprecedented High-temperature CO_2 Selectivity in N_2-phobic Nanoporous Covalent Organic Polymers. *Nat. Commun.* **2013**, *4*, 1357.

(9) Lu, W. G.; Yuan, D. Q.; Zhao, D.; Schilling, C. I.; Plietzsch, O.; Muller, T.; Brase, S.; Guenther, J.; Blumel, J.; Krishna, R.; Li, Z.; Zhou, H. C. Porous Polymer Networks: Synthesis, Porosity, and Applications in Gas Storage/Separation. *Chem. Mater.* **2010**, *22*, 5964-5972.

(10) Byun, J.; Patel, H. A.; Thirion, D.; Yavuz, C. T. Charge-Specific Size-Dependent Separation of Water-soluble Organic Molecules by Fluorinated Nanoporous Networks. *Nat. Commun.* **2016**, *7*, 13377.

(11) Tunstad, L. M.; Tucker, J. A.; Dalcanale, E.; Weiser, J.; Bryant, J. A.; Sherman, J. C.; Helgeson, R. C.; Knobler, C. B.; Cram, D. J. Host Guest Complexation .48. Octol Building-Blocks for Cavitands and Carcerands. *J. Org. Chem.* **1989**, *54*, 1305-1312.

(12) Thommes, M.; Kaneko, K.; Neimark, A. V.; Olivier, J. P.; Rodri-guez-Reinoso, F.; Rouquerol, J.; Sing, K. S. W. Physisorption of Gases, with Special Reference to the Evaluation of Surface Area and Pore Size Distribution (IUPAC Technical Report). *Pure Appl. Chem.* **2015**, *87*, 1051-1069.

(13) Ji, G. P.; Yang, Z. Z.; Zhang, H. Y.; Zhao, Y. F.; Yu, B.; Ma, Z. S.; Liu, Z. M. Hierarchically Mesoporous o-Hydroxyazobenzene Polymers: Synthesis and Their Applications in CO_2 Capture and Conversion. *Angew. Chem. Int. Ed.* **2016**, *55*, 9685-9689.

(14) Patil, R. S.; Zhang, C.; Atwood, J. L. Process Development for Separation of Conformers from Derivatives of Resorcin[4]arenes and Pyrogallol[4]arenes. *Chem. Eur. J.* **2016**, *22*,15202–15207.

(15) Pei, W. Y.; Xu, G.; Yang, J.; Wu, H.; Chen, B.; Zhou, W.; Ma, J. F. Versatile Assembly of Metal-Coordinated Calix[4]resorcinarene Cavitands and Cages through Ancillary Linker Tuning. *J. Am. Chem. Soc.* **2017**, *139*, 7648-7656.

(16) Atwood, J. L.; Barbour, L. J.; Jerga. A. Storage of Methane and Freon by Interstitial van der Waals Confinement. *Science* **2002**, *296*, 2367-2369.

(17) Jeromenok, J.; Weber, J. Restricted Access: On the Nature of Adsorption/Desorption Hysteresis in Amorphous, Microporous Polymeric Materials. *Langmuir* **2013**, *29*, 12982-12989.

(18) Weber, J.; Antonietti, M.; Thomas, A. Microporous Networks of High-Performance Polymers: Elastic Deformations and Gas Sorption Properties. *Macromolecules* **2008**, *41*, 2880-2885.

(19) Bezuidenhout, C. X.; Smith, V. J.; Bhatt, P. M.; Esterhuysen, C.; Barbour, L. J. Extreme Carbon Dioxide Sorption Hysteresis in Open-Channel Rigid Metal–Organic Frameworks. *Angew. Chem., Int. Ed.* **2015**, *54*, 2079-2083.

(20) Lu, W.; Sculley, J. P.; Yuan, D.; Krishna, R.; Wei, Z.; Zhou, H. C. Polyamine-tethered Porous Polymer Networks for Carbon Dioxide Capture from Flue Gas. *Angew. Chem. Int. Ed.* **2012**, *51*, 7480-7484.

(21) Li, L.; Cai, Z.; Wu, Q.; Lo, W.; Zhang, N.; Chen, L. X.; Yu, L. Rational Design of Porous Conjugated Polymers and Roles of Residual Palladium for Photocatalytic Hydrogen Production. *J. Am. Chem. Soc.* **2016**, *138*, 7681-7686.

(22) Xu, T. Y.; Zhang, Q. F.; Yang, H. F.; Li, X. N.; Wang, J. G. Role of Phenolic Groups in the Stabilization of Palladium Nanoparticles. *Ind. Eng. Chem. Res.* **2013**, *52*, 9783-9789.

(23) Yang, J.; Yuan, M.; Xu, D.; Zhao, H.; Zhu, Y. Y.; Fan, M. Y.; Zhang, F. W.; Dong, Z. P. Highly Dispersed Ultrafine Palladium Nanoparticles Encapsulated in a Triazinyl Functionalized Porous Organic Polymer as a Highly Efficient Catalyst for Transfer Hydrogenation of Aldehydes. *J. Mater. Chem. A* **2018**, *6*, 18242-18251.

(24) Lu, W. G.; Bosch, M.; Yuan, D. Q.; Zhou, H. C. Cost-Effective Synthesis of Amine-tethered Porous Materials for Carbon Capture. *ChemSusChem* **2015**, *8*, 433-438.

(25) Shen, L.; Bao, N.; Yanagisawa, K.; Gupta, A.; Domen, K.; Grimes, C. A. Controlled Synthesis and Assembly of Nanostructured ZnO Architectures by a Solvothermal Soft Chemistry Process. *Cryst. Growth Des.* **2007**, *7*, 2742-2748.

(26) Bandyopadhyay, S.; Anil, A. G.; James, A.; Patra, A. Multifunctional Porous Organic Polymers: Tuning of Porosity, CO_2, and H_2 Storage and Visible-Light-Driven Photocatalysis. *ACS Appl. Mater. Interfaces* **2016**, *8*, 27669-27678.

(27) Chen, J.; Li, H.; Zhong, M.; Yang, Q. Hierarchical Mesoporous Organic Polymer with an Intercalated Metal Complex for the Efficient Synthesis of Cyclic Carbonates from Flue Gas. *Green Chem.* **2016**, *18*, 6493-6500.

(28) Martin, C.; Fiorani, G.; Kleij, A. W. Recent Advances in the Catalytic Preparation of Cyclic Organic Carbonates. *ACS Catal.* **2015**, *5*, 1353-1370.

(29) Fan, H.; Gu, J.; Meng, H.; Knebel, A.; Caro, J. High-Flux Membranes Based on the Covalent Organic Framework COF-LZU1 for Selective Dye Separation by Nanofiltration. *Angew. Chem. Int. Ed*. **2018**, *57*, 4083-4087.

(30) He, X. Y.; Male, K. B.; Nesterenko, P. N.; Brabazon, D.; Paull, B.; Luong, J. H. T. Adsorption and Desorption of Methylene Blue on Porous Carbon Monoliths and Nanocrystalline Cellulose. *ACS Appl. Mater. Interfaces* **2013**, *5*, 8796-8804.

(31) Oz, M.; Lorke, D. E.; Hasan, M.; Petroianu, G. A. Cellular and Molecular Actions of Methylene Blue in the Nervous System. *Med. Res. Rev.* **2010**, *31*, 93-117.

(32) Azizian, S. Kinetic Models of Sorption: a Theoretical Analysis. *J. Colloid Interface Sci*. **2004**, *276*, 47-52.

(33) Ho, Y. S.; McKay, G. Pseudo-Second Order Model for Sorption Processes. *Process. Biochem.* **1999**, *34*, 451-465.

(34) Roy, A.; Adhikari, B.; Majumder, S. B. Equilibrium, Kinetic, and Thermodynamic Studies of Azo Dye Adsorption from Aqueous Solution by Chemically Modified Lignocellulosic Jute Fiber. *Ind. Eng. Chem. Res.* **2013**, *52*, 6502-6512.

(35) Alsbaiee, A.; Smith, B. J.; Xiao, L. L.; Ling, Y. H.; Helbling, D. E.; Dichtel, W. R. Rapid Removal of Organic Micropollutants from Water by a Porous β-Cyclodextrin Polymer. *Nature* **2016**, *529*, 190-194.

(36) Li, H. Y.; Meng, B.; Chai, S. H.; Liu, H. L.; Dai, S. Hyper-Crosslinked β-Cyclodextrin Porous Polymer: An Adsorption-Facilitated Molecular Catalyst Support for Transformation of Water-Soluble Aromatic Molecules. *Chem. Sci.* **2016**, *7*, 905-909.

(37) Alzate-Sanchez, D. M.; Smith, B. J.; Alsbaiee, A.; Hinestroza, J. P.; Dichtel, W. R. Cotton Fabric Functionalized with a β-Cyclodextrin Polymer Captures Organic Pollutants from Contaminated Air and Water. *Chem. Mater.* **2016**, *28*, 8340-8346.

(38) Xiao, L. L.; Ling, Y. H.; Alsbaiee, A.; Li, C. J.; Helbling, D. E.; Dichtel, W. R. β-Cyclodextrin Polymer Network Sequesters Perfluorooctanoic Acid at Environmentally Relevant Concentrations. *J. Am. Chem. Soc.* **2017**, *139*, 10585-10585.

(39) Y Zhang, Y. Y.; Duan, J. Y.; Ma, D.; Li, P. F.; Li, S. W.; Li, H. W.; Zhou, J. W.; Ma, X. J.; Feng, X.; Wang, B. Three-Dimensional Anionic Cyclodextrin-Based Covalent Organic Frameworks. *Angew. Chem. Int. Ed.* **2017**, *56*, 16313-16317.

(40) Wang, R. Q.; Wei, X. B.; Feng, Y. Q. β-Cyclodextrin Covalent Organic Framework for Selective Molecular Adsorption. *Chem. Eur. J.* **2018**, *24*, 10979-10983.

(41) Klemes, M. J.; Ling, Y. H.; Chiapasco, M.; Alsbaiee, A.; Helbling, D. E.; Dichtel, W. R. Phenolation of cyclodextrin polymers controls their lead and organic micropollutant adsorption. *Chem. Sci.* **2018**, *9*, 8883-8889.

(42) Talapaneni, S. N.; Kim, D.; Barin, G.; Buyukcakir, O.; Je, S. H.; Coskun, A. Pillar[5]arene Based Conjugated Microporous Polymers for Propane/Methane Separation through Host-Guest Complexation. *Chem. Mater.* **2016**, *28*, 4460-4466.

(43) Lan, S.; Zhan, S. J.; Ding, J. M.; Ma, J. Q.; Ma, D. Pillar[n]arene-Based Porous Polymers for Rapid Pollutant Removal from Water. *J. Mater. Chem. A* **2017**, *5*, 2514-2518.

(44) Li, X.; Li, Z.; Yang, Y. W. Tetraphenylethylene-Interweaving Conjugated Macrocycle Polymer Materials as Two-Photon Fluorescence Sensors for Metal Ions and Organic Molecules. *Adv. Mater.* **2018**, *30*, 1800177.

(45) Shetty, D.; Jahovic, I.; Raya, J.; Ravaux, F.; Jouiad, M.; Olsen, J. C.; Trabolsi, A. An Ultra-Absorbent Alkyne-rich Porous Covalent Polycalix[4]arene for Water Purification. *J. Mater. Chem. A* **2017**, *5*, 62-66.

(46) Shetty, D.; Raya, J.; Han, D. S.; Asfari, Z.; Olsen, J. C.; Trabolsi, A. Lithiated Polycalix[4]arenes for Efficient Adsorption of Iodine from Solution and Vapor Phases. *Chem. Mater.* **2017**, *29*, 8968-8972.

(47) Shetty, D.; Jahovic, J.; Raya, J.; Asfari, Z.; Olsen, J. C.; Trabolsi, A. Porous Polycalix[4]arenes for Fast and Efficient Removal of Organic Micropollutants from Water. *ACS Appl. Mater. Interfaces* **2018**, *10*, 2976-2981.

(48) Shetty, D.; Skorjanc, T.; Raya, J.; Sharma, S. K.; Jahovic, I.; Polychronopoulou, K.; Asfari, Z.; Han, D. S.; Dewage, S.; Olsen, J. C.; Jagannathan, R.; Kirmizialtin, S.; Trabolsi, A. Calix[4]arene-Based Porous Organic Nanosheets. *ACS Appl. Mater. Interfaces* **2018**, *10*, 17359-17365.

(49) Skorjanc, T.; Shetty, D.; Sharma, S. K.; Raya, J.; Trabolsi, H.; Han, D. S.; Lalla, J.; Newlon, R.; Jagannathan, R.; Kirmizialtin, S.; Olsen, J. C.; Trabolsi, A. Redox-Responsive Covalent Organic Nanosheets from Viologens and Calix[4]arene for Iodine and Toxic Dye Capture. *Chem. Eur. J.* **2018**, *24*, 8648-8655.

(50) Su, K. Z.; Wang, W. J.; Li, B. B.; Yuan, D. Q. Azo-Bridged Calix[4]resorcinarene-Based Porous Organic Frameworks with Highly Efficient Enrichment of Volatile Iodine. *ACS Sustain. Chem. Eng.* **2018**, *6*, 17402-17409.

(51) Zhao, Q.; Liu, Y. Tunable Photo-Luminescence Behaviors of Macrocycle-Containing Polymer Networks in the Solid-State. *Chem. Commun.* **2018**, *54*, 6068-6071.

(52) Zhao, Q.; Liu, Y. Macrocycle Crosslinked Mesoporous Polymers for Ultrafast Separation of Organic Dyes. *Chem. Commun.* **2018**, *54*, 7362-7365.

(53) Lo Meo, P.; Lazzara, G.; Liotta, L.; Riela, S.; Noto, R. Cyclodextrin-Calixarene Co-Polymers as a New Class of Nanosponges. *Polym. Chem.* **2014**, *5*, 4499-4510.

(54) Zhu, Y. L.; Long, H.; Zhang, W. Imine-Linked Porous Polymer Frameworks with High Small Gas (H_2, CO_2, CH_4, C_2H_2) Uptake and CO_2/N_2 Selectivity. *Chem. Mater.* **2013**, *25*, 1630-1635.

(55) Arab, P.; Rabbani, M. G.; Sekizkardes, A. K.; Islamoglu, T.; El-Kaderi, H. M. Copper(I)-Catalyzed Synthesis of Nanoporous Azo-Linked Polymers: Impact of Textural Properties on Gas Storage and Selective Carbon Dioxide Capture. *Chem. Mater.* **2014**, *26*, 1385-1392.

(56) Chang, G. J.; Shang, Z. F.; Yu, T.; Yang, L. Rational Design of a Novel Indole-Based Microporous Organic Polymer: Enhanced Carbon Dioxide Uptake via Local Dipole-π Interactions. *J. Mater. Chem. A* **2016**, *4*, 2517-2523.

(57) Dey, S.; Bhunia, A.; Esquivel, D.; Janiak, C. Covalent Triazine-Based Frameworks (CTFs) from Triptycene and Fluorene Motifs for CO_2 Adsorption. *J. Mater. Chem. A* **2016**, *4*, 6259-6263.

(58) Hussain, W.; Bandyopadhyay, S.; Patra, A. Microporous Organic Polymers Involving Thiadiazolopyridine for High and Selective Uptake of Greenhouse Gases at Low Pressure. *Chem. Commun.* **2017**, *53*, 10576-10579.

(59) Yang, X.; Yu, M.; Zhao, Y.; Zhang, C.; Wang, X. Y.; Jiang, J. X. Remarkable Gas Adsorption by Carbonized Nitrogen-Rich Hypercrosslinked Porous Organic Polymers. *J. Mater. Chem. A* **2014**, *2*, 15139-15145.

(60) Kandambeth, S.; Mallick, A.; Lukose, B.; Mane, M. V.; Heine, T.; Banerjee, R. Construction of Crystalline 2D Covalent Organic Frameworks with Remarkable Chemical (Acid/Base) Stability via a Combined Reversible and Irreversible Route. *J. Am. Chem. Soc.* **2012**, *134*, 19524-19527.

(61) Yu, S. Y.; Mahmood, J.; Noh, H. J.; Seo, J. M.; Jung, S. M.; Shin, S. H.; Im, Y. K.; Jeon, I. Y.; Baek, J. B. Direct Synthesis of a Covalent Triazine-Based Framework from Aromatic Amides. *Angew. Chem. Int. Ed.* **2018**, *57*, 8438-8442.

(62) Rabbani, M. G.; El-Kaderi, H. M. Synthesis and Characterization of Porous Benzimidazole-Linked Polymers and Their Performance in Small Gas Storage and Selective Uptake. *Chem. Mater.* **2012**, *24*, 1511-1517.

(63) Zhang, X.; Lu, J. Z.; Zhang, J. Porosity Enhancement of Carbazolic Porous Organic Frameworks Using Dendritic Building Blocks for Gas Storage and Separation. *Chem. Mater.* **2014**, *26*, 4023-4029.

(64) Chen, Q.; Wang, J. X.; Wang, Q.; Bian, N.; Li, Z. H.; Yan, C. G.; Han, B. H. Spiro(fluorene-9,9 '-xanthene)-Based Porous Organic Polymers: Preparation, Porosity, and Exceptional Hydrogen Uptake at Low Pressure. *Macromolecules* **2011**, *44*, 7987-7993.

(65) Wong-Foy, A. G.; Matzger, A. J.; Yaghi, O. M. Exceptional H_2 saturation uptake in microporous metal-organic frameworks. *J. Am. Chem. Soc.* **2006**, *128*, 3494-3495.

(66) Wang, X. S.; Ma, S. Q.; Forster, P. M.; Yuan, D. Q.; Eckert, J.; Lopez, J. J.; Murphy, B. J.; Parise, J. B.; Zhou, H. C. Enhancing H_2 Uptake by "Close-Packing" Alignment of Open Copper Sites in Metal-Organic Frameworks. *Angew. Chem. Int. Ed.* **2008**, *47*, 7263-7266.

(67) Sumida, K.; Hill, M. R.; Horike, S.; Dailly, A.; Long, J. R. Synthesis and Hydrogen Storage Properties of $Be_{12}(OH)_{12}$ (1,3,5-benzenetribenzoate)$_4$. *J. Am. Chem. Soc.* **2009**, *131*, 15120-15121.

(68) Pan, L.; Parker, B.; Huang, X. Y.; Olson, D. H.; Lee, J.; Li, J. Zn(tbip) (H_2tbip= 5-*tert*-Butyl Isophthalic Acid)): A Highly Stable Guest-Free Microporous Metal Organic Framework with Unique Gas Separation Capability. *J. Am. Chem. Soc.* **2006**, *128*, 4180-4181.

(69) Perles, J.; Iglesias, M.; Martin-Luengo, M. A.; Monge, M. A.; Ruiz-Valero, C.; Snejko, N. Metal-Organic Scandium Framework: Useful Material for Hydrogen Storage and Catalysis. *Chem. Mater.* **2005**, *17*, 5837-5842.

(70) Lee, J. Y.; Pan, L.; Kelly, S. R.; Jagiello, J.; Emge, T. J.; Li, J. Achieving High Density of Adsorbed Hydrogen in Microporous Metal Organic Frameworks. *Adv. Mater.* **2005**, *17*, 2703.

(71) Krawiec, P.; Kramer, M.; Sabo, M.; Kunschke, R.; Frode, H.; Kaskel, S. Improved Hydrogen Storage in the Metal-Organic Framework $Cu_3(BTC)_2$. *Adv. Eng. Mater.* **2006**, *8*, 293-296.

(72) Liu, B.; Shioyama, H.; Akita, T.; Xu, Q. Metal-Organic Framework as a Template for Porous Carbon Synthesis. *J. Am. Chem. Soc.* **2008**, *130*, 5390-5391.

(73) To, J. W. F.; He, J.; Mei, j.; Haghpanah, R.; Chen, Z.; Kurosawa, T.; Chen, S.; Bae, W. G.; Pan, L.; Tok, J. B. H.; Wilcox, J.; Bao, Z. Hierarchical N-Doped Carbon as CO_2 Adsorbent with High CO_2 Selectivity from Rationally Designed Polypyrrole Precursor. *J. Am. Chem. Soc.* **2016**, *138*, 1001-1009.

(74) Sun, Q.; Aguila, B.; Perman, J.; Nguyen, N.; Ma, S. Q. Flexibility Matters: Cooperative Active Sites in Covalent Organic Framework and Threaded Ionic Polymer. *J. Am. Chem. Soc.* **2016**, *138*, 15790-15796.

(75) Liu, F. J.; Huang, K.; Wu, Q.; Dai, S. Solvent-Free Self-Assembly to the Synthesis of Nitrogen-Doped Ordered Mesoporous Polymers for Highly Selective Capture and Conversion of CO_2. *Adv. Mater.* **2017**, *29*, 1700445.

(76) Xie, Y.; Wang, T. T.; Liu, X. H.; Zou, K.; Deng, W. Q. Capture and Conversion of CO_2 at Ambient Conditions by a Conjugated Microporous Polymer. *Nat. Commun.* **2013**, *4*, 1960.

(77) Wang, W. L.; Li, C. Y.; Yan, L.; Wang, Y. Q.; Jiang, M.; Ding, Y. J. Ionic Liquid/Zn-PPh_3 Integrated Porous Organic Polymers Featuring Multifunctional Sites: Highly Active Heterogeneous Catalyst for Cooperative Conversion of CO_2 to Cyclic Carbonates. *ACS Catal.* **2016**, *6*, 6091-6100.

(78) Chen, J.; Li, H.; Zhong, M. M.; Yang, Q. H. Hierarchical Mesoporous Organic Polymer with An Intercalated Metal Complex for the Efficient Synthesis of Cyclic Carbonates from Flue Gas. *Green Chem.* **2016**, *18*, 6493-6500.

(79) Buyukcakir, O.; Je, S. H.; Talapaneni, S. N.; Kim, D.; Coskun, A. Charged Covalent Triazine Frameworks for CO_2 Capture and Conversion. *ACS Appl. Mater. Interfaces* **2017**, *9*, 7209-7216.

(80) Guo, Z. J.; Cai, X. C.; Xie, J. Y.; Wang, X. C.; Zhou, Y.; Wang, J. Hydroxyl-Exchanged Nanoporous Ionic Copolymer toward Low Temperature Cycloaddition of Atmospheric Carbon Dioxide into Carbonates. *ACS Appl. Mater. Interfaces* **2016**, *8*, 12812-12821.

(81) Jayakumar, S.; Li, H.; Chen, J.; Yang, Q. H. Cationic Zn-Porphyrin Polymer Coated onto CNTs as a Cooperative Catalyst for the Synthesis of Cyclic Carbonates. *ACS Appl. Mater. Interfaces* **2018**, *10*, 2546-2555.

(82) Alkordi, M. H.; Weselinski, L. J.; D'Elia, V.; Barman, S.; Cadiau, A.; Hedhili, M. N.; Cairns, A. J.; AbdulHalim, R. G.; Basset, J. M.; Eddaoudi, M. CO_2 Conversion: the Potential of Porous-Organic Polymers (POPs) for Catalytic CO_2-Epoxide Insertion. *J. Mater. Chem. A* **2016**, *4*, 7453-7460.

(83) Wang, J. Q.; Yang, J. G. W.; Yi, G. S.; Zhang, Y. G. Phosphonium Salt Incorporated Hypercrosslinked Porous Polymers for CO_2 Capture and Conversion. *Chem. Commun.* **2015**, *51*, 15708-15711.

(84) Ding, M. L.; Jiang, H. L. One-Step assembly of a Hierarchically Porous Phenolic Resin-type Polymer with High Stability for CO_2 Capture and Conversion. *Chem. Commun.* **2016**, *52*, 12294-12297.

(85) Subramanian, S.; Park, J.; Byun, J.; Jung, Y.; Yavuz, C. T. Highly Efficient Catalytic Cyclic Carbonate Formation by Pyridyl Salicylimines. *ACS Appl. Mater. Interfaces* **2018**, *10*, 9478-9484.

(86) Das, P; Mandal, S. K. In-Depth Experimental and Computational Investigations for Remarkable Gas/Vapor Sorption, Selectivity, and Affinity by a Porous Nitrogen-Rich Covalent Organic Framework. *Chem. Mater.* **2019**, *31*, 1584-1596.

(87) Wang, X. C.; Zhou, Y.; Guo, Z. J.; Chen, G. J.; Li, J.; Shi, Y. M.; Liu, Y. Q.; Wang, J. Heterogeneous conversion of CO_2 into cyclic carbonates at ambient pressure catalyzed by ionothermal-derived meso-macroporous hierarchical poly(ionic liquid)s. *Chem. Sci.* **2015**, *6*, 6916-6924.

(88) Meng, X. L.; He, H. Y.; Nie, Y.; Zhang, X. P.; Zhang, S. J.; Wang, J. J. Temperature-Controlled Reaction-Separation for Conversion of CO_2 to Carbonates with Functional Ionic Liquids Catalyst. *ACS Sustain. Chem. Eng.* **2017**, *5*, 3081-3086.

(89) Guillerm, V.; Weselinski, L. J.; Belmabkhout, Y.; Cairns, A. J.; D'Elia, V.; Wojtas, L.; Adil, K.; Eddaoudi, M. Discovery and introduction of a (3,18)-connected net as an ideal blueprint for the design of metal-organic frameworks. *Nat. Chem.* **2014**, *6*, 673-680.

(90) Zhou, Z.; He, C.; Xiu, J. H.; Yang, L.; Duan, C. Y. Metal-Organic Polymers Containing Discrete Single-Walled Nanotube as a Heterogeneous Catalyst for the Cycloaddition of Carbon Dioxide to Epoxides. *J. Am. Chem. Soc.* **2015**, *137*, 15066-15069.

(91) Zhu, J.; Usov, P. M.; Xu, W. Q.; Celis-Salazar, P. J.; Lin, S. Y.; Kessinger, M. C.; Landaverde-Alvarado, C.; Cai, M.; May, A. M.; Slebodnick, C.; Zhu, D. R.; Senanayake, S. D.; Morris, A. J. A New Class of Metal-Cyclam-Based Zirconium Metal-Organic Frameworks for CO_2 Adsorption and Chemical Fixation. *J. Am. Chem. Soc.* **2018**, *140*, 993-1003.

(92) Beyzavi, M. H.; Klet, R. C.; Tussupbayev, S.; Borycz, J.; Vermeulen, N. A.; Cramer, C. J.; Stoddart, J. F.; Hupp, J. T.; Farha, O. K. A Hafnium-Based Metal Organic Framework as an Efficient and Multifunctional Catalyst for Facile CO_2 Fixation and Regioselective and Enantioretentive Epoxide Activation. *J. Am. Chem. Soc.* **2014**, *136*, 15861-15864.

(93) Du, Y.; Yang, H.; Wan, S.; Jina, Y.; Zhang, W. A titanium-based porous coordination polymer as a catalyst for chemical fixation of CO_2. *J. Mater. Chem. A* **2017**, *5*, 9163-9168.

(94) Li, P. Z.; Wang, X. J.; Liu, J.; Lim, J. S.; Zou, R.; Zhao, Y. A Triazole-Containing Metal–Organic Framework as a Highly Effective and Substrate Size-Dependent Catalyst for CO_2 Conversion. *J. Am. Chem. Soc.* **2016**, *138*, 2142-2145.

(95) Lyu, J.; Zhang, X.; Otake, K.; Wang, X.; Li, P.; Li, Z.; Chen, Z.; Zhang, Y.; Wasson, M. C.; Yang, Y.; Bai, P.; Guo, X.; Islamoglu, T.; Farha, O. K. Topology and Porosity Control of Metal–organic Frameworks through Linker Functionalization. *Chem. Sci.* **2019**, *10*, 1186-1192.

(96) Ng, C. K.; Toh, R. W.; Lin, T. T.; Luo, H.; Hor, T. S. A.; Wu, J. Metal-salen Molecular Cages as Efficient and Recyclable Heterogeneous Catalysts for Cycloaddition of CO_2 with Epoxides under Ambient Conditions. *Chem. Sci.* **2019**, *10*, 1549-1554.

(97) Ning, G. H.; Chen, Z. X.; Gao, Q.; Tang, W.; Chen, Z. X.; Liu, C. B.; Tian, B. B.; Li, X.; Loh, K. P. Salicylideneanilines-Based Covalent Organic Frameworks as Chemoselective Molecular Sieves. *J. Am. Chem. Soc.* **2017**, *139*, 8897-8904.

(98) Kandambeth, S.; Biswal, B. P.; Chaudhari, H. D.; Rout, K. C.; Kunjattu, H. S.; Mitra, S.; Karak, S.; Das, A.; Mukherjee, R.; Kharul, U. K.; Banerjee, R. Selective Molecular Sieving in Self-Standing Porous Covalent-Organic-Framework Membranes. *Adv. Mater.* **2017**, *29*, 1603945.

(99) Zhang, C.; Zhu, P. C.; Tan, L.; Liu, J. M.; Tan, B.; Yang, X. L.; Xu, H. B. Triptycene-Based Hyper-Cross-Linked Polymer Sponge for Gas Storage and Water Treatment. *Macromolecules* **2015**, *48*, 8509-8514.

(100) Shen, R.; Yan, X. D.; Guan, Y. J.; Zhu, W.; Li, T.; Liu, X. G.; Li, Y. X.; Gu, Z. G. One-Pot Synthesis of a Highly Porous Anionic Hypercrosslinked Polymer for Ultrafast Adsorption of Organic Pollutants. *Polym. Chem.* **2018**, *9*, 4724-4732.

(101) Karak, S.; Dey, K.; Torris, A.; Halder, A.; Bera, S.; KP, F.; Banerjee, R. Inducing Disorder in Order: Hierarchically Porous Covalent Organic Framework Nanostructures for Rapid Removal of Persistent Organic Pollutants. *J. Am. Chem. Soc.* **2019**, *141*, 7572-7581.